Chiba University Doctoral Dissertation

Branching ratio measurement of a structure dependence radiative $K^+ \to e^+\nu_e\gamma$ decay using the J-PARC E36 detector system

Atsushi Kobayashi

Graduate School of Science and Engineering
CHIBA UNIVERSITY

January 2022

Abstract

The structure dependent $K^+ \to e^+ \nu \gamma$ ($K^{\mathrm{SD}}_{e2\gamma}$) decay was investigated with a stopped K^+ beam. The e^+ momentum vectors were determined by reconstructing charged particle tracks in the spectrometer with and without a photon in coincidence. The photon momentum vectors were obtained from the energy and position information by the CsI(Tl) calorimeter. The gap sandwitch counters (GSC) were also used for detecting photons. The detector acceptance and response function were calculated by Monte Carlo simulations. The ratio of the branching ratio of the $K^{\mathrm{SD}}_{e2\gamma}$ decay and the $K^+ \to e^+ \nu$ decay including the internal bremsstrahlung process ($K_{e2(\gamma)}$) were obtained to be $Br(K^{\mathrm{SD}}_{e2\gamma})/Br(K_{e2(\gamma)}) = 1.12 \pm 0.07(\mathrm{stat}) \pm 0.04(\mathrm{syst})$ and $Br(K^{\mathrm{SD}}_{e2\gamma})/Br(K_{e2(\gamma)}) = 1.15 \pm 0.12(\mathrm{stat}) \pm 0.08(\mathrm{syst})$ from the CsI(Tl) and GSC analyses, respectively. They are consistent within the experimental uncertainties, although the kinematical approach of the CsI(Tl) and GSC analysis are so different. This feature implies that invisible and/or non-evaluated systematic uncertainties are expected to be smaller than the current ones.

The $Br(K^{\mathrm{SD}}_{e2\gamma})/Br(K_{e2(\gamma)})$ value obtained in the CsI(Tl) analysis indicates a partial branching ratio, $Br(K^{\mathrm{SD}+}_{e2\gamma},\ p_e > 200\ \mathrm{MeV}/c,\ E_\gamma > 10\ \mathrm{MeV})/Br(K_{\mu2}) = (1.85 \pm 0.11_{\mathrm{stat}} \pm 0.07_{\mathrm{syst}}) \times 10^{-5}$, which is 25%($\sim 2.5\sigma$) higher than the previous experimental result which supported the theoretical model of Chiral Perturbation Theory. On the other hand, the present result is in agreement with the recent lattice calculation.

It has been well known that the $K^{\mathrm{SD}}_{e2\gamma}$ decay is one of the most dominant backgrounds in the experiment to search for lepton universality violation by measuring the ratio of the K_{e2} and $K^+ \to \mu^+ \nu$ ($K_{\mu2}$) branching ratios (R_K). In the R_K analysis, the $K^{\mathrm{SD}}_{e2\gamma}$ decay with a missing photon cannot be discriminated from the observed $K_{e2(\gamma)}$ sample and has to be subtracted using the information of the observed $K^{\mathrm{SD}}_{e2\gamma}$ events with the photon detection. In the present work, separate spectra were obtained for events with one and two photons detected in the CsI(Tl) calorimeter and for events without conditions on the number of photons; these were fit simultaneously to determine the $Br(K^{\mathrm{SD}}_{e2\gamma})/Br(K_{e2(\gamma)})$ value. The successful fitting made the reliable $K^{\mathrm{SD}}_{e2\gamma}$ subtraction from the e^+ sample, and the present work promoted one of the essential analysis in the R_K determination.

In the NA62 experiment, which produced the result with the smallest R_K uncertainty, the $K^{\mathrm{SD}}_{e2\gamma}$ decay was the main background source in the $K_{e2(\gamma)}$ sample. The branching ratio of the $K^{\mathrm{SD}}_{e2\gamma}$ reported by the KLOE group was used in the NA62 analysis, and this SD contribution was subtracted from the observed $K_{e2(\gamma)}$. This indicates the $K^{\mathrm{SD}}_{e2\gamma}$ fraction would increase by 25% and affect the R_K result in the NA62 analysis.

Contents

1 Introduction

Studies of charged and neutral K mesons (kaon) have strongly contributed to the understanding of various weak interaction phenomena and to the establishment of the Standard Model (SM) in particle physics so far. In 1956, the idea that invariance with respect to space inversion (parity) is actually violated in weak interaction was proposed by Lee and Yang to solve a peculiarity known as the θ-τ puzzle ($K^+ \to \pi^+\pi^0$ and $K^+ \to \pi^+\pi^+\pi^-$) [1, 2, 3]. Direct evidence of parity violation, P violation, was then observed in the detection of left-right symmetry in β-ray emission form polarized ^{60}Co nuclei by Wu[4]. After the discovery of parity violation, sufficient data on the decay systematics of β decay, muon decay, and meson decay established the famous V−A law. In 1964, another important aspect of the weak interaction, violation of combined invariance of parity and charge conjugation (CP invariance) was observed by Christenson et al. [5] in long-lived neutral kaon K_L system. K_L had been assigned to be an eigenstate of $CP = -1$, however, a small but finite branching ratio of 0.2% for the decay $K_L \to \pi^+\pi^-$, in which the final state has $CP = +1$, was observed [5]. In 1970, Glashow, Iliopoulos, and Maiani proposed the GIM model [6], where the fourth quark, charm quark, was introduced to explain the very small branching fraction of $K_L \to \mu^+\mu^-$ (9×10^{-9}) namely the absence of flavor-changing neutral current processes. In 1973, the GIM model was further generalized to take six quarks into account in Kobayashi-Maskawa model [7], in which CP violation was naturally involved in the imaginary phase of the quark mixing matrix (CKM matrix).

These days, kaon physics is becoming more and more important as one of the major fields of particle physics, because kaon decays provide further a playground to study the fundamental electroweak interaction and important information for the low energy strong interaction through their decay widths and form factors. It is well recognized that there are many interesting decay modes [8], as is listed in Table 1. Some rare decay experiment such as $K^+ \to \pi^+\nu\bar{\nu}$ [9] and $K_L \to \pi^0\nu\bar{\nu}$ [10] are now testing the standard model through the precise determination of CKM matrix elements, and further to search for new physics beyond the standard model. Also, violation of time reversal invariance was searched for by precisely measuring the transverse muon polarization in $K^+ \to \pi^0\mu^+\nu$ decay [11]. A systematic study of various decay modes offers the means to test effective theories of Quantum Chromo Dynamics (QCD) at low energy such as Chiral Perturbation Theory (ChPT) and Lattice calculation, which has recently been developing [12].

As well as searches for rare kaon decays, high precision electroweak tests represent a powerful tool to prove the SM and to obtain indirect hints of new physics. The $K^+ \to l^+\nu_l$ decay (K_{l2}), which is one of the simplest decays among the K^+ decay channels, is a clean and sensitive channel to perform such tests. Lepton universality, which is expressed as the identical coupling constant of the three lepton generations —the electron, muon, and tau— is a basic assumption in the SM. Violation of lepton universality clearly indicates the existence of other physics beyond the SM. Although each K_{l2} decay width can be described using the K_{l2} hadronic form factor with a few percent accuracy, this form factor can be canceled out by forming the ration of electronic $K^+ \to e^+\nu$ (K_{e2}) and muonic $K^+ \to \mu^+\nu$ ($K_{\mu2}$) decay channels. In this R_K measurement, the structure dependent $K^+ \to e^+\nu\gamma$ decay ($K_{e2\gamma}^{\mathrm{SD}}$) is a serious background and has to be subtracted from the observed e^+ events [13].

In the present dissertation work, I measured both of $K_{e2(\gamma)}$ and $K_{e2\gamma}^{\mathrm{SD}}$ decays using the toroidal spectrometer for charged particles and the CsI(Tl) and GSC detectors for photons using a stopped K^+beam at the J-PARC. The branching ratio of $K_{e2\gamma}^{\mathrm{SD}}$ relative to that of $K_{e2(\gamma)}$ decay was successfully

Table 1: Major K^+ decay modes.

Mode	Symbol	Fraction
$K^+ \to e^+\nu$	K_{e2}	$(1.582 \pm 0.007) \times 10^{-5}$
$K^+ \to \mu^+\nu$	$K_{\mu2}$	0.6351 ± 0.0018
$K^+ \to e^+\nu\gamma(\mathrm{SD})$	$K_{e2\gamma}^{\mathrm{SD}}$	
$K^+ \to \pi^+\pi^0$	$K_{\pi2}$	0.2066 ± 0.0008
$K^+ \to \pi^+\pi^+\pi^-$	$K_{\pi3}$	0.0559 ± 0.0004
$K^+ \to \pi^0 e^+\nu_e$	K_{e3}	0.0507 ± 0.0004
$K^+ \to \pi^0\mu^+\nu_\mu$	$K_{\mu3}$	0.0335 ± 0.0003
$K^+ \to \pi^+\pi^0\pi^0$		0.0176 ± 0.0002
$K^+ \to \mu^+\nu_\mu\gamma$		$(6.2 \pm 0.8) \times 10^{-3}$
$K^+ \to \pi^0 e^+\nu_e\gamma$		$(2.56 \pm 0.16) \times 10^{-4}$
$K^+ \to \pi^+\nu\bar{\nu}$		$(8^{+6}_{-4}) \times 10^{-13}$

determined. In this dissertation, details of the experiment, analysis, and results are described. In section 2, the motivation of the $K_{e2\gamma}^{\mathrm{SD}}$ decay is described. In section 3, details of the experimental configuration are explained by separating each detector component. Principle of the measurement and methodology to drive the $K_{e2\gamma}^{\mathrm{SD}}$ branching ratio, as well as details of the analysis procedure are written in section 4. The detector acceptance and background contamination are estimated by a Monte Carlo simulation, as described in section 5. In section 6, the $Br(K_{e2\gamma}^{\mathrm{SD}})/Br(K_{e2(\gamma)})$ ratio is determined by fitting the $K_{e2\gamma}^{\mathrm{SD}}$ and $K_{e2(\gamma)}$ momentum spectra simultaneously using the CsI(Tl) calorimeter and GSC counter. Systematic uncertainties in the measurement are carefully discussed in section 7. The results and conclusion of this work are finally summarized in section 8.

2 Physics motivation

2.1 The $\Gamma(K^+ \to e^+\nu)/\Gamma(K^+ \to \mu^+\nu)(R_K)$ measurement

The matrix element of K_{l2} decays can be described to be

$$
\begin{aligned}
M &= g_l \frac{G}{\sqrt{2}} q^\lambda f(q^2)[u_l\gamma_\lambda(1-\gamma_5)u_\nu] & (1) \\
&= g_l \frac{G}{\sqrt{2}} f_K m_l u_l(1-\gamma_5)u_\nu, & (2)
\end{aligned}
$$

where g_l is the coupling constant for the lepton current and g_e/g_μ should be unity under the assumption of lepton universality. $f(q^2)$ is the hadronic form factor as a function of momentum transfer squared (q^2) which is the only Lorentz scalar that can be formed from q. However, in the present case, $q^2 = m_K^2$ and $f(m_K^2) = f_K$ is a constant. The K_{l2} decay diagrams are shown in Fig. 1. Then, the K_{l2} decay width can be calculated as

$$
\Gamma(K_{l2}) = g_l^2 \frac{G^2}{8\pi} f_K^2 m_K m_l^2 \left(1 - \frac{m_l^2}{m_K^2}\right)^2. \tag{3}
$$

This K_{l2} hadronic form factor can be canceled out by forming the ratio of the electric (K_{e2}) and muonic $(K_{\mu2})$ decay modes as,

$$
R_K = \frac{\Gamma(K^+ \to e^+\nu)}{\Gamma(K^+ \to \mu^+\nu)} = \left(\frac{g_e}{g_\mu}\right)^2 \frac{m_e^2}{m_\mu^2} \left(\frac{m_K^2 - m_e^2}{m_K^2 - m_\mu^2}\right)^2 (1 + \delta_r). \tag{4}
$$

Here, δ_r is a correction due to the internal bemsstrahlung process (IB). The factor $(m_e/m_\mu)^2$ accounts for the helicity suppression of K_{e2} decay due to the $V - A$ structure of the charged weak current, and, in other words, easy to access to effects beyond the SM. By inserting the particle masses into Eq. (4), the R_K value is calculated as

$$
R_K^{SM} = (2.472 \pm 0.001) \times 10^{-5}. \tag{5}
$$

under the assumption of μ-e universality. Conversely, this ratio can provide a test of μ-e universality as,

$$
g_\mu/g_e = (R_K^{\exp}/R_K^{SM})^{1/2}. \tag{6}
$$

As a result, the SM prediction of R_K^{SM} is known with excellent accuracy $(\Delta R_K/R_K \sim 0.4 \times 10^{-3})$ and this makes it possible to search for new physics effects by a precise measurement of R_K.

2.2 Contribution from MSSM

Over the past forty years, the SM has been very successful in explaining various physics phenomena. However, it is said that the SM is only an effective low-energy description and new physics lies at the
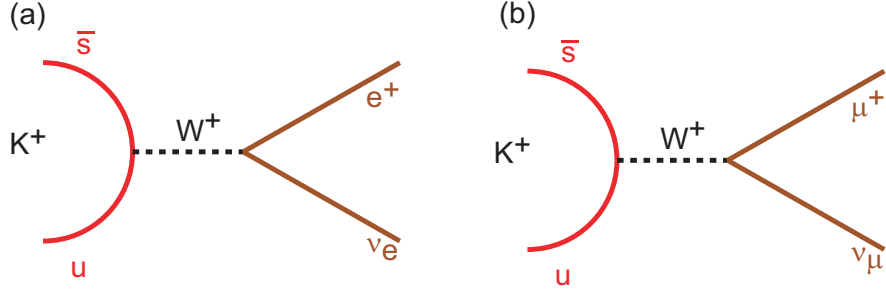
Figure 1: Feynman diagrams of (a) K_{e2} and (b) $K_{\mu 2}$. The hadronic form factor f_K is canceled out by forming the ratio of the decay widths. The SM prediction of R_K is known with excellent accuracy.

energy scale of $\sim$TeV. There is a good chance that the LHC will discover new elementary particles such as various supersymmetric (SUSY) particles. Recently, in the kaon physics field, a minimal SUSY extension of the SM (MSSM) with R parity has also been considered as a candidate for new physics to be tested by R_K [14, 15, 16, 17]. It is well known that models containing at least two Higgs doublets generally allow flavor violating couplings of the Higgs bosons with the fermions. In the MSSM, such Lepton Flavor Violation (LFV) couplings are absent at tree level. However, once no holomorphic terms are generated by loops and given a source of LFV among the sleptons, Higgs-mediated Hll LFV couplings are unavoidable. These effects have been widely discussed in the recent literature through the study of several processes, namely $\tau \to l_j l_k l_k$ [18], $\tau \to \mu\eta$ [19], μ-e conversion in nuclei [20], $B \to l_j \tau$ [21], $H \to l_j l_k$ [22], and $l_i \to l_j \gamma$ [23]. In the case of K_{l2}, in addition to the normal $W^{\pm}$ exchange shown in Fig. 1, a possible mechanism to detect the LFV SUSY effect through a deviation from the μ-e universality has been discussed. A charged Higgs-mediated SUSY LFV contribution, as shown in Fig. 2, can be strongly enhanced by emitting a τ neutrino. This non-vanishing e-τ lepton mixing effect can be described as,

$$R_K^{\mathrm{LFV}} = R_K^{\mathrm{SM}} \left(1 + \frac{m_K^4}{M_{H^+}^4} \cdot \frac{m_\tau^2}{m_e^2} \Delta_{13}^2 \tan^6\beta \right), \tag{7}$$

where M_H is the mass of the charged Higgs. Δ_{13} is the term induced by the exchange of a Bino and a slepton, which represents the contribution of LFV effect generated from the off-diagonal flavor changing entries of the slepton mass matrix. A large enhancement factor m_τ^2/m_e^2 can produce a sizable effect in R_K through change of the K_{e2} width. On the other hand, the $K_{\mu 2}$ branching ratio would be also changed due to non-vanishing μ-τ mixing, however this contribution to $K_{\mu 2}$ is estimated by replacing m_e with m_μ in Eq.(7) to be a factor of $\sim m_e^2/m_\mu^2$ smaller. Taking $\Delta_{13} = 5 \times 10^{-4}$, $\tan\beta = 40$, and $M_H = 500$ GeV, we can obtain $R_K^{\mathrm{LFV}} = 1.013 \times R_K^{\mathrm{SM}}$. Thus, it is possible to reach a contribution at the percent level thanks to the possible LFV enhancements arising in SUSY models. Here it should be noted that the second term in Eq. (7) is proportional to m_K^4, indicating that the μ-e universality test in the pion channel, the measurement of $R_\pi = \Gamma(\pi^+ \to e^+\nu)/\Gamma(\pi^+ \to \mu^+\nu)$, is not sensitive to this model because of the suppression factor of m_π^4/m_K^4, unless the achievable experimental sensitivity of R_π is much higher than that of R_K. Therefore, the advantage of the R_K measurement can be summarized as,

9
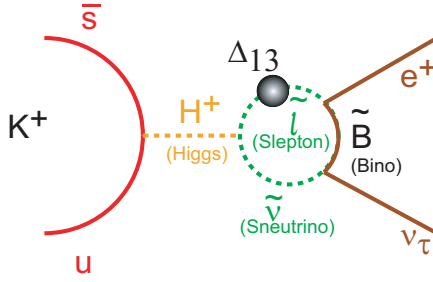
Figure 2: Contribution from charged Higgs-mediated LFV effect arising in SUSY model. Effect from non-vanishing e-τ mixing can be strongly enhanced by emitting a τ neutrino.

- The branching ratio of K_{e2} is very small due to the helicity suppression in the $V - A$ structure. However this makes the K_{e2} decay sensitive to the physics beyond the SM.

- By forming the ratio of the K_{e2} to $K_{\mu 2}$ width, the hadronic form factor is cancelled out and the R_K prediction in the SM becomes highly precise.

- The charged Higgs-mediated LFV effect arising in SUSY models can contribute to the K_{e2} width at the percent level. Since this effect is proportional to m_K^4, the lepton universality test in the kaon channel is much superior to that in the pion channel.

- We can observe the LFV effect as a deviation from μ-e universality by measuring the R_K value with high precision.

2.3 Experimental status of the lepton universality test

The current world average of R_K is composed of three 1970s measurements. Recently, the NA48 and KLOE groups performed measurements, and they reported the results of the R_K values [24, 25]. The results of these measurements are shown in Table 2 .

2.3.1 NA48/2 and NA62 at CERN

The NA62 experiment at CERN collected a large sample of $K^+ \to e^+ \nu$ decays during a dedicated run in 2007-08, which allowed a precise test of lepton universality. The NA48/2 beam line and the experimental setup were used. The running conditions were optimized for the K_{e2} measurement in 2007 using the experience of earlier studies based on the NA48/2 data. The beam line was capable of simultaneously delivering K^+ and K^- beams with a narrow momentum band and a central momentum of 74 GeV/c was adopted in 2007. The momentum of the incoming kaon was not measured directly in event by event, but the averaged beam momentum was monitored by using $K_{\pi 3}$ decays to reconstruct K_{l2} kinematics from the missing mass (M_{miss}). The narrow momentum spectrum ($\delta p_K^{\mathrm{RMS}}/p_K \simeq 2\%$) had the advantage to minimize the contribution to the M_{miss} resolution. The K_{l2} decay signature consisted of a single reconstructed track. Since the incoming K^+ was not tracked, backgrounds

Table 2: Summary of the R_K and R_π measurements. The NA62, the KLOE, and the E36 experiments are compared. Characteristics of the three experiments and the R_π experiments are summarized in the table. E/p is the ratio of the measured energy by a colorimeter and the measured momentum by a spectrometer for PID.

Measurement	Kaon Beam	PID	R_K $(\times 10^{-5})$	$\Delta R_K/R_K$
PDG [26]			2.45±0.11	4%
KLOE [27]	In-flight $(\phi \rightarrow K^\pm)$	E/p and TOF	2.493±0.025±0.019	1.3%
NA62 [24]	In-flight $(\mathrm{p}(K^\pm) =$ 74 GeV/c)	E/p	2.488±0.007±0.007	0.4%
SM [28]			2.472±0.001	0.04%

Measurement	Pion Beam	PID	$R_\pi(\times 10^{-4})$	$\Delta R_\pi/R_\pi$
PDG [26]			1.230±0.004	0.3%
PIBETA [29]	stopped π^+	E/p	1.2346±0.0035±0.0036	0.4%
Britton et al. [30]	stopped π^+	$\pi \rightarrow \mu \rightarrow e$	1.2265±0.0034±0.0044	0.4%
PEN [31]	stopped π^+	E/p		< 0.05%
PIENU [32]	stopped π^+	$\pi \rightarrow \mu \rightarrow e$		< 0.1%
SM [26]			1.2353±0.0004	0.03%
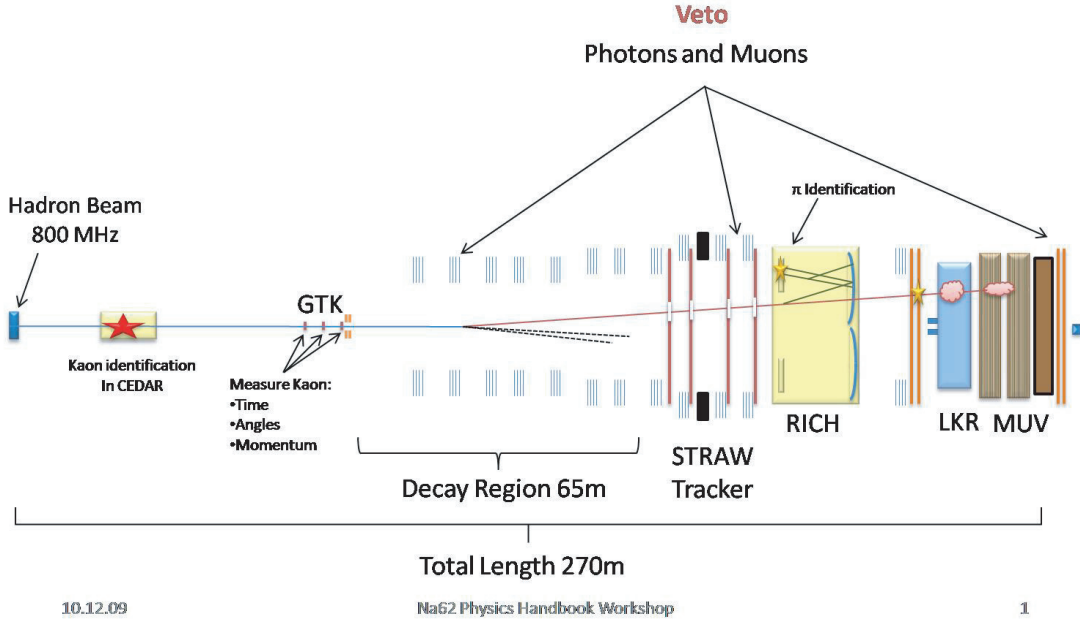
Figure 3: Cross sectional side view of the NA62 experiment. The beam line is capable of simultaneously delivering K^+ and K^- beams with a narrow momentum band. Among the sub-detectors located downstream of the vacuum decay volume, a magnetic spectrometer, a plastic scintillator hodoscope, and a liquid krypton electromagnetic calorimeter are principal for the measurement.

induced by the beam halo had to be carefully considered. The performance of the muon sweeping magnet system resulted in lower background in the K_{e2}^+ sample ($\simeq 1\%$) than in the K_{e2}^- sample ($\simeq 20\%$). The halo background was directly measurable using the samples of reconstructed K_{l2} candidates. Among the sub-detectors located downstream of a vacuum decay volume, a magnetic spectrometer, a plastic scintillator hodoscope, and a liquid krypton electromagnetic calorimeter were principal for this measurement. The spectrometer, which was used to detect charged products from kaon decays, was composed of four drift chambers and a dipole magnet. A beam pipe traversing the center of the detectors allowed undecayed beam particles and muons from decays of beam pions to continue their movement in vacuum.

The number of K_{l2} candidates is $N(K_{e2}) = 145{,}958$ and $N(K_{\mu2}) = 4.282 \times 10^7$. The finall NA62 result was[24]

$$R_K = [2.488 \pm 0.007(stat.) \pm 0.007(syst.)] \times 10^{-5} \tag{8}$$
$$= (2.488 \pm 0.010) \times 10^{-5}, \tag{9}$$

which is consistent with the SM expectation.

12

2.3.2   KLOE at DAφNE

The KLOE detector operated at DAφNE which was the Frascati $e^+ e^-$ collider system working at a center of mass energy $W \sim m_\phi \sim 1.02$ GeV. ϕ mesons were produced with a cross section of $\sim 3.1\mu$b and a transverse momentum of ~ 12.5 MeV$/c$ directed toward the center of the collider rings. The coordinates of the beam's interaction point and the ϕ momentum were determined, run by run, with high precision from Bhabha scattering events. The KLOE detector consisted of a large drift chamber (DC) surrounded by an electromagnetic calorimeter (EMC). A superconducting coil provides an axial magnetic field of 0.52 T. The DC was a cylinder of 4 m diameter and 3.3 m in length. The momentum resolution for tracks at large polar angle was $\sigma_p/p \sim 0.4\%$. The EMC was a lead-scintillating fiber sampling calorimeter consisting of a barrel and two endcaps covering 98% of the solid angle. The photon energy and timing resolutions were $\sigma_E/E \sim 5.7\%/\sqrt{E/\text{GeV}}$ and $\sigma_t = 54$ ps$/\sqrt{E/\text{GeV}} \oplus 50$ ps.

Physics Letters B 672(3):203-208
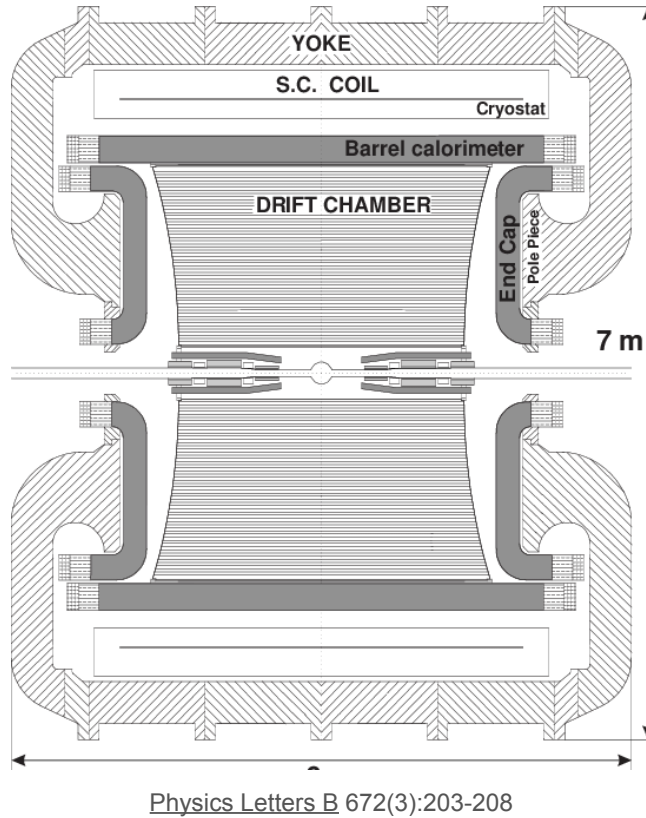
Figure 4: Cross sectional side view of the KLOE expreiment. the KOLE detector consists of a large drift chamber (DC) surrounded by an electro-magnetic calorimeter (EMC). The R_K analysis was performed by using the data collected for an integrated luminosity of 2.2 fb^{-1}.

The R_K analysis was performed using the data collected for an integrated luminosity of 2.2 fb^{-1}. The number of collected events for $K^+ \rightarrow e^+\nu(\gamma)$ and $K^- \rightarrow e^-\nu(\gamma)$ were 7064±102 and 6750±101, respectively. 89.8% of these events had $E_\gamma < 10$ MeV. The signal-to-background correlation was 20% and the χ^2/ndf was 113/112(140/112) for $K^+(K^-)$.

From a fit to the missing mass (m_l^2) distribution, the number of $K_{\mu 2}$ events was obtained to be 2.878×10^8 for $K_{\mu 2}^+$ and 2.742×10^8 for $K_{\mu 2}^-$. The fraction of background events under the muon events is estimated from MC to be less than 1×10^{-3}. The difference between the K^+ and K^- counts was mainly due to K^- nuclear interactions in the material traversed. They performed a comprehensive study of the $K_{e2\gamma}$ process. The ratio of the $K_{e2\gamma}$ and $K_{\mu 2}$ widths for photon energies smaller than 10 MeV was carefully checked to remove any systematic bias from the $K_{e2\gamma}^{\rm SD}$ component. The R_K value was obtained to be[25]

$$R_K = [2.493 \pm 0.025(stat.) \pm 0.019(syst.)] \times 10^{-5}, \tag{10}$$

which is also in agreement with the SM prediction. The experimental sensitivity was $\Delta R_K / R_K = 1.3\%$.

2.4 Physics Motivation of the structure dependence radiative $K^+ \to e^+ \nu \gamma (K_{e2\gamma}^{\rm SD})$ decay

In the R_K determination, the radiative $K^+ \to e^+ \nu \gamma$ decay, which is the K_{e2} decay accompanied with photon emission, has to be taken into account. There are two $K_{e2\gamma}$ processes [33, 34]: the internal bremsstrahlung (IB) process, $K_{e2\gamma}^{\rm IB}$, mostly with low-energy photon emission, and the structure dependent (SD) process, $K_{e2\gamma}^{\rm SD}$, with high-energy photon emission roughly in the same and opposite directions of the e^+ motions, respectively (see below).

The diagram of the $K_{e2\gamma}$ IB and SD process is shown in Fig. 5. Also, the correlation plot for the γ energy and e^+-γ opening angle is shown in Fig. 6. The SD process can be described as the emission of photons from virtual hadronic states, as shown in Fig. 5, and is parameterized in terms of form factors in the standard description (see below), which provides a powerful tool to investigate the hadronic structure of kaons.

Internal Bremsstrahlung (IB)   Structure Dependent (SD)
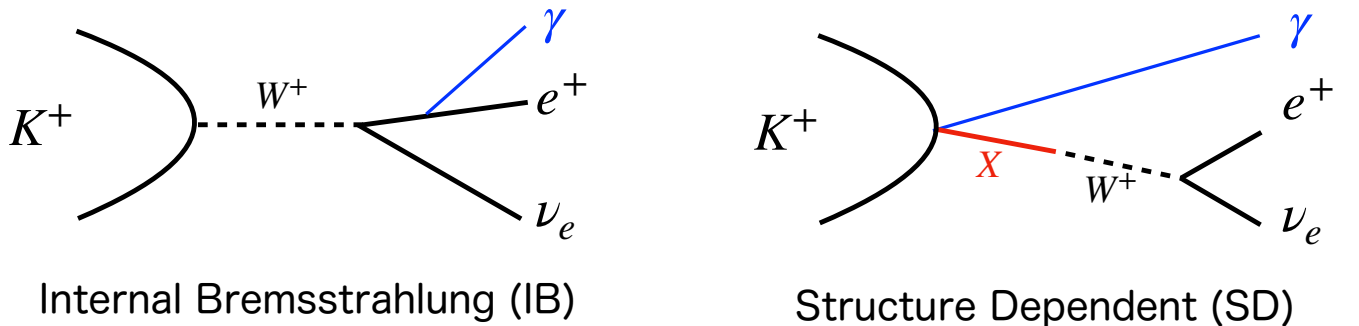
Figure 5: The diagram of the $K_{e2\gamma}$ IB and SD process. The radiative photon from the SD process is emitted from the intermediate state with particular structures.

In order to compare the experimental value with the SM prediction, the IB process has to be included in the K_{e2} sample ($K_{e2(\gamma)} = K_{e2} + K_{e2\gamma}^{\rm IB}$) because it is impossible to experimentally separate the IB process from the K_{e2} decay due to the infrared divergence at $E_\gamma = 0$. On the other hand, the
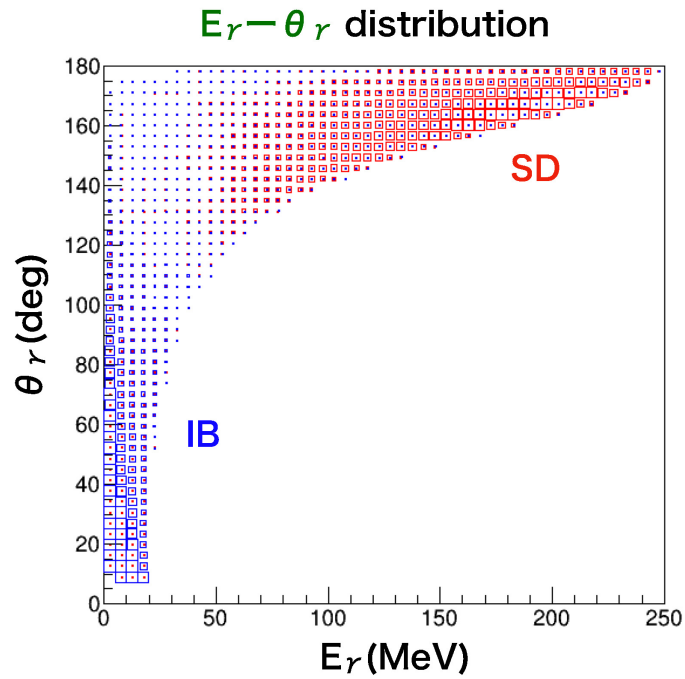
Figure 6: The correlation plot for the γ energy and e^{+}-γ opening angle for the IB and SD processes in the region of $P_{e^{+}} > 230$ MeV. As can be easily understood, the spectral shapes are quite distinct and it can be concluded that a separation of the IB and SD processes is quite feasible.

SD process, which has a large hadronic uncertainty, is regarded as a background for R_K and has to be subtracted from the observed e^+ events. The $K_{e2(\gamma)}$ branching ratio is strongly suppressed down to $\sim 10^{-5}$ due to the helicity suppression mechanism of the weak charged current. The SD process is not subject to the above helicity suppression, and the $K_{e2\gamma}^{\mathrm{SD}}$ branching ratio is comparable to that of $K_{e2(\gamma)}$ due to the existence of the radiative photon, as shown in Fig. 7. In the R_K analysis, the $K_{e2\gamma}^{\mathrm{SD}}$ decay with a missing photon cannot be discriminated from the observed $K_{e2(\gamma)}$ sample. Therefore, the $Br(K_{e2\gamma}^{\mathrm{SD}})$ value is very important for the $K_{e2\gamma}^{\mathrm{SD}}$ subtraction in the R_K analysis process. In addition, the SD process is sensitive to the electroweak structure of the kaon and has been the subject of extensive theoretical studies [33, 34, 35, 36], since the $K_{e2\gamma}^{\mathrm{IB}}$ can be reliably calculated as a higher order QED correction in the SM theory.
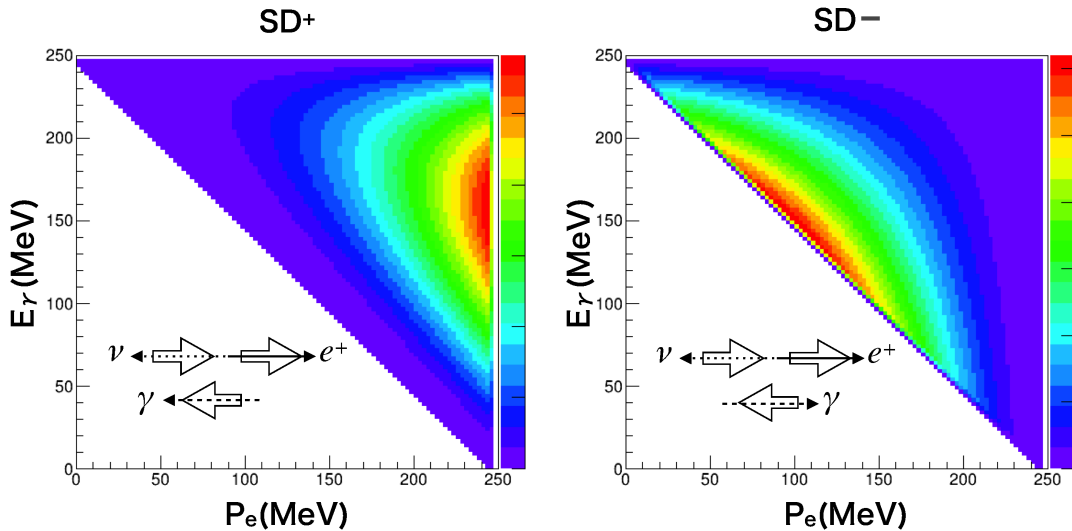
Figure 7: The Dalitz distribution of (left) SD$^+$ and (right) SD$^-$ processes. Owing to the fact that kaon is spinless and e^+ and ν have fixed helicities, SD$^+$ and SD$^-$ have different angular correlation of the decay particles. For SD$^+$, the γ is emitted preferentially anti-parallel to the e^+ motion, whereas for SD$^-$, the γ is emitted preferentially anti-parallel to the ν motion. Consequently, the e^+ momentum spectrum for SD$^+$ is peaked at the maximum energy $E_{\mathrm{max}} = 247$ MeV/c, whereas it is peaked at $1/2 E_{\mathrm{max}}$ for SD$^-$.

The Dalitz density of the $K_{e2\gamma}^{\mathrm{SD}}$ decays can be described using the theoretical scheme of vector and axial-vector transitions [33, 34] as

$$\frac{d^2\Gamma(K_{e2\gamma}^{\mathrm{SD}})}{dxdy} = \frac{G_F^2 \alpha m_K^5 \sin^2\theta_c}{64\pi^2} \times [(V+A)^2 f_{\mathrm{SD}^+} + (V-A)^2 f_{\mathrm{SD}^-}], \tag{11}$$

where G_F is the Fermi constant, α is the fine structure constant, m_K is the kaon mass, and θ_c is the Cabibbo angle. The form factors V and A represent the vector and axial-vector transitions, respectively. The kinematical density distribution for both helicity terms f_{SD^+} and f_{SD^-} can be described as,

$$f_{\mathrm{SD}^+} = (x+y-1)^2(1-x) \quad \text{and} \quad f_{\mathrm{SD}^-} = (1-y)^2(1-x), \tag{12}$$

16

by ignoring small $\mathcal{O}(m_e/m_K)$ contributions, where $x = 2E_\gamma/m_K$ and $y = 2E_e/m_K$ are dimensionless photon and e^+ energies, respectively, and m_e is the positron mass. It should be noted that the SD^-, IB, and IB/SD^+ interference are negligibly small in the high-momentum e^+ region $230 < p < 250$ MeV/c and in the large (e^+, γ) opening angle region [33], which cannot be detected by the E36 experiment. Owing to the fact that kaon is spinless and e^+ and ν have fixed helicities, SD^+ and SD^- have different angular correlation of the decay particles. For SD^+, the γ is emitted preferentially anti-parallel to the e^+ motion, whereas for SD^-, the γ is emitted preferentially anti-parallel to the ν motion. Consequently, the e^+ momentum spectrum for SD^+ is peaked at the maximum energy $E_{\max} = 247$ MeV/c, whereas it is peaked at $1/2 E_{\max}$ for SD^-.

Here, V was assumed to have the momentum transfer dependence $V = V_0[1 + \lambda(1 - x)]$, while A was constant, according to the Chiral Perturbation Theory (ChPT) model at $\mathcal{O}(p^6)$ [35, 36]. The λ and A/V_0 parameters were taken to be $\lambda = 0.3 \pm 0.1$ and $A/V_0 = 0.4 \pm 0.1$[1], respectively, which is the current theoretical conceivable range of ChPT $\mathcal{O}(p^6)$ model calculations [34]. The $K_{e2(\gamma)}$ decay with the IB component, calculated including re-summation of the decay probability for multiple photon emission [37].

The KLOE group reported the experimental result of the branching ratio of $Br(K_{e2\gamma}^{\mathrm{SD}})$ relative to that of the $K_{\mu 2}$ decay in the partial phase space where the charged particle momentum (p^{KLOE}) and photon energy (E_γ^{KLOE}) are higher than 200 MeV/c and 10 MeV, respectively, to be $Br(K_{e2\gamma}^{\mathrm{SD}}, p^{\mathrm{KLOE}} > 200$ MeV/c, $E_\gamma^{\mathrm{KLOE}} > 10$MeV)/$Br(K_{\mu 2}) = (1.483 \pm 0.066 \pm 0.011) \times 10^{-5}$ [38]. The branching ratio of the $K_{e2\gamma}^{\mathrm{SD}}$ reported by the KLOE group was used in the NA62 analysis, and this SD contribution was subtracted from the observed $K_{e2(\gamma)}$ samples. Therefore, an experimental check of the SD branching ratio with a systematically different approach from KLOE is important. In this thesis, I present a new measurement of the branching ratio of the $K_{e2\gamma}^{\mathrm{SD}}$ decay relative to that of the $K_{e2(\gamma)}$ decay, $\mathrm{Br}(K_{e2\gamma}^{\mathrm{SD}})/\mathrm{Br}(K_{e2(\gamma)})$, performed with the J-PARC E36 experiment, which is also aiming at testing lepton universality violation with a precise R_K measurement [39, 40].

---

[1]The difference of the A/V_0 value obtained by the $\mathcal{O}(p^4)$ and $\mathcal{O}(p^6)$ calculations is adopted as a systematic uncertainty.

3 The E36 experiment at J-PARC

3.1 Overview of $\mathrm{Br}(K_{e2\gamma}^{\mathrm{SD}})/\mathrm{Br}(K_{e2(\gamma)})$ measurement in the E36 experiment

This experiment was performed at J-PARC employing a stopped K^+ beam in conjunction with a 12-sector iron-core superconducting toroidal spectrometer. The detector drawing to explain the concept of the E36 experiment is shown in Fig. 8 (a). The $K_{e2(\gamma)}$ and $K_{e2\gamma}^{\mathrm{SD}}$ decays at rest are accepted by analyzing charged particle momenta using the spectrometer. In order to measure the structure dependence process in radiative $K^+ \to e^+\nu\gamma$ ($K_{e2\gamma}^{\mathrm{SD}}$) decays, the radiative photon was measured by the photon calorimeter. The $K_{e2\gamma}^{\mathrm{SD}}$ decay is carefully studied using events with e^+ sample with the photon detection, and the $K_{e2\gamma}^{\mathrm{SD}}$ fraction is calculated by correcting for the photon detector acceptance and subtracted from the e^+ sample for the R_K analysis, as shown in Fig 8 (b).
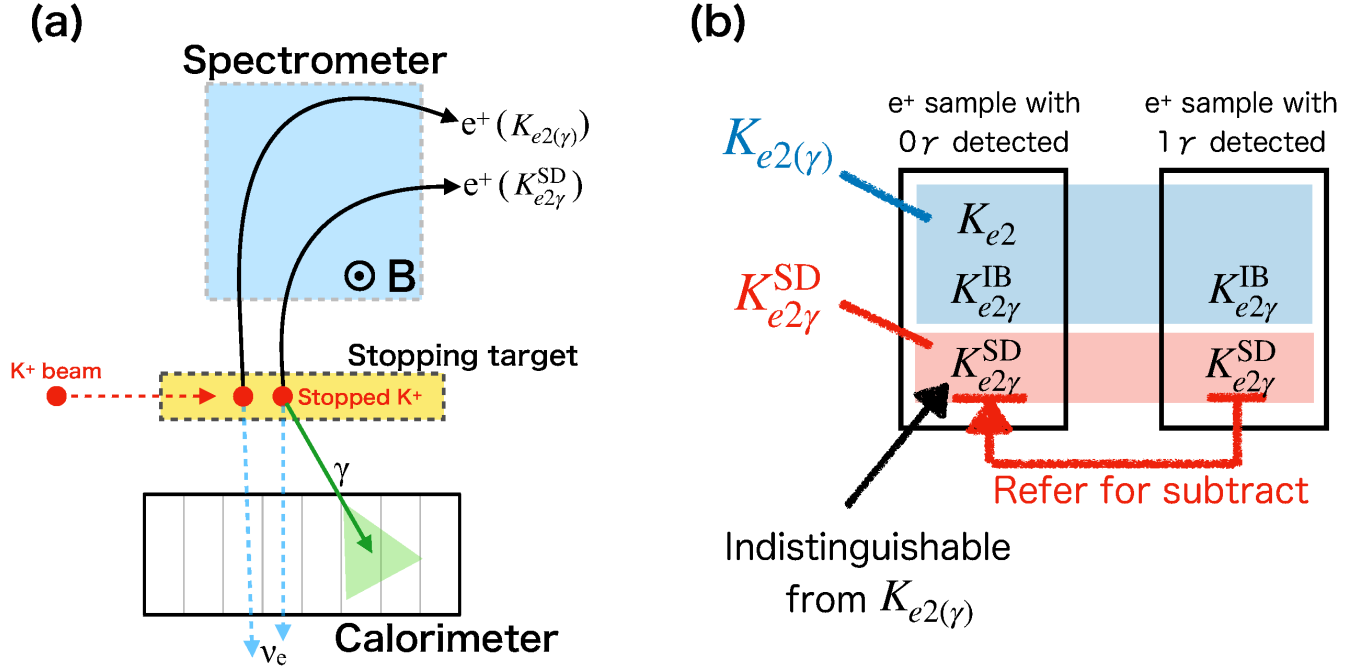
Figure 8: (a) The detector drawing to explain the concept of the E36 experiment and (b) the analysis procedure for the branching ratio determination of $K_{e2\gamma}^{\mathrm{SD}}$ and the $K_{e2\gamma}^{\mathrm{SD}}$ subtraction for the R_K analysis. The $K_{e2(\gamma)}$ and $K_{e2\gamma}^{\mathrm{SD}}$ decays at rest are accepted by analyzing charged particle momenta using the spectrometer. In order to extract the structure dependence process in radiative $K^+ \to e^+\nu\gamma$ ($K_{e2\gamma}^{\mathrm{SD}}$) decays, the radiative photon was measured by the photon calorimeter.

Schematic cross sectional side and end views of the detector system are shown in Fig. 9. The value is derived from the numbers of the accepted $K_{e2(\gamma)}$ and $K_{e2\gamma}^{\mathrm{SD}}$ events by correcting for the detector acceptance. Charged kaons were produced by the 30-GeV proton beam impinging on the Pt production target. A separated 780-MeV/c K^+ beam was extracted using the J-PARC K1.1BR beam line. The beam was slowed down by a degrader and stopped in a position-sensitive fiber target. Charged particles from the target are tracked and momentum-analyzed using Spiral fiber tracker

End View

GSC
Cryostat
Iron Pole
e^+
TOF1, SFT
AC
C2
TGT
CsI(Tl)
γ

Side View

Cryostat
C4
C3
PGC
GSC
Iron Pole
e^+
Lead
Shield
C2
TOF2
BC
CsI(Tl)
TGT
K^+
TOF1, SFT
AC
Degrader
γ

0   0.5   1.0 m

Figure 9: Cross sectional end and side views of the setup for the R_K experiment and the heavy neutrino search. The momentum vectors of charged particles and photons are determined by the toroidal spectrometer and the CsI(Tl) calorimeter, respectively. The assembly around the target system is shown in Fig. 21.

(SFT) and three multi-wire proportional chambers (C2, C3, C4) in each toroidal sector. The $K_{e2(\gamma)}$, $K^{\mathrm{SD}}_{e2\gamma}$ and other kaon decays were collected for central magnetic field of the spectrometer, $B = 1.5$ T. The SFT detector was placed at the central part of the E36 apparatus surrounding the fiber target. The C2 and C3-C4 chambers were set at the entrance and exit of the magnet gaps, respectively. In order to remove K_{e3}, $K_{\mu3}$ and $K_{\mu2}$ backgrounds, $K_{e2(\gamma)}$ and $K^{\mathrm{SD}}_{e2\gamma}$ events were identified by requiring the charged particle momentum to be higher than the $K_{\mu2}$ endpoints ($P^{\mathrm{Max}}_e = 236$ MeV/c, as shown in schematically Fig. 10. Particle discrimination between e^+ and μ^+ was carried out using an aerogel Cherenkov (AC) counters, and lead glass (PGC) Chere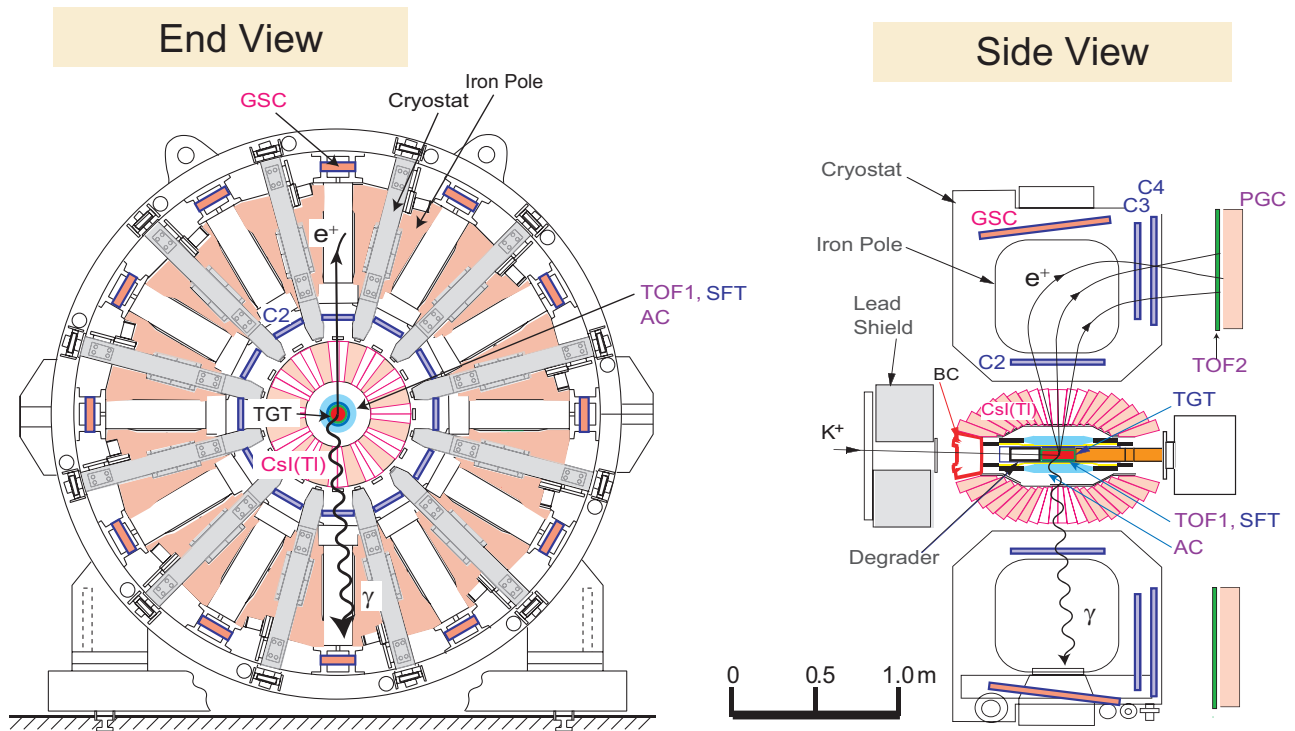nkov counters, and by measuring the time-of-flight (TOF) between the TOF1 and TOF2 scintillation counters. TOF1 and AC surrounded the SFT+target system. TOF2 was located about 90cm behind C4, and PGC was set just after TOF2. The γ detector, an assembly of 768 CsI(Tl) crystals, covers 75% of the total solid angle. Since photons produce electro-magnetic showers, their energy was shared among several crystals. The photon energy and hit position were obtained by summing the energy deposits and by determining the energy-weighted centroid, respectively. A Pb-plastic sandwich detector as the gap photon counter (GSC) was set at the outer radius of the magnet pole to detect photons passing through the photon detector holes. The 0γ and 1γ events were accepted as $K_{e2(\gamma)}$ or $K^{\mathrm{SD}}_{e2\gamma}$ samples. The number of
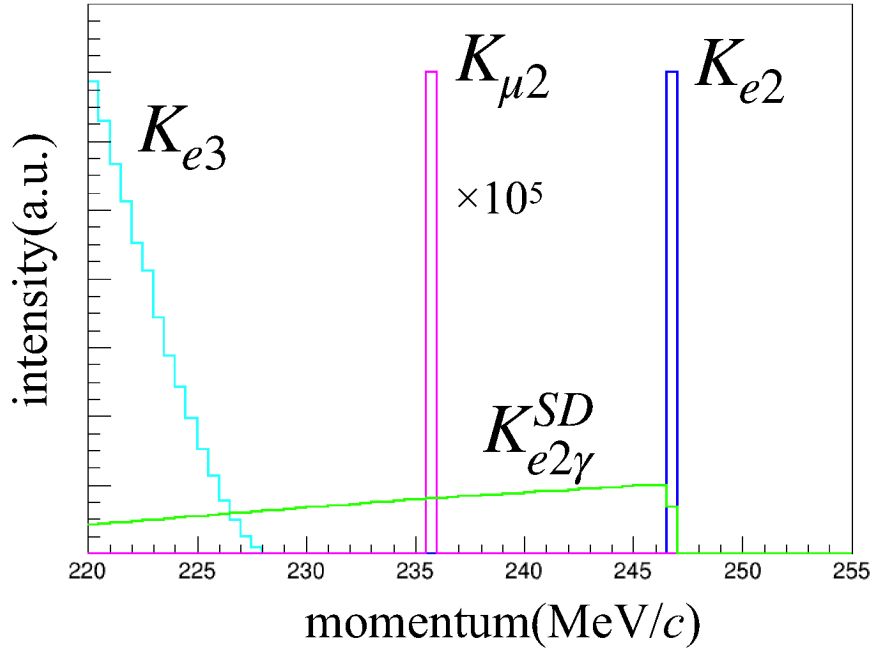
Figure 10: Schematic momentum spectra of K_{e2}, K_{e3}, $K^{\mathrm{SD}}_{e2\gamma}$ and $K_{\mu2}$. The accessible region in this experiment is above the K_{e3} endpoints. The K_{e2} and $K^{\mathrm{SD}}_{e2\gamma}$ momenta are imposed to be higher than the endpoints of K_{e3}.

accepted events, $K_{e2(\gamma)} = K_{e2} + K^{\mathrm{IB}}_{e2\gamma}$ and $K^{\mathrm{SD}}_{e2\gamma}$, after background subtraction can be described as

$$N(K^{\mathrm{SD}}_{e2\gamma}) = N_K \times \Omega(K^{\mathrm{SD}}_{e2\gamma}) \times Br(K^{\mathrm{SD}}_{e2\gamma}) \tag{13}$$

$$N(K_{e2(\gamma)}) = N_K \times \Omega(K_{e2(\gamma)}) \times Br(K_{e2(\gamma)}). \tag{14}$$

20

Here N_K is the number of stopped kaon in the target, Br is the branching ratio, and Ω is the acceptance. Therefore, the $Br(K_{e2\gamma}^{\mathrm{SD}})/Br(K_{e2(\gamma)})$ ratio can be obtained by making the ratio of the accepted $K_{e2(\gamma)}$ to $K_{e2\gamma}^{\mathrm{SD}}$ event numbers corrected for the detector acceptance as,

$$\frac{Br(K_{e2\gamma}^{\mathrm{SD}})}{Br(K_{e2(\gamma)})} = \frac{N(K_{e2\gamma}^{\mathrm{SD}})}{N(K_{e2(\gamma)})} \cdot R_\Omega = \frac{N(K_{e2\gamma}^{\mathrm{SD}})}{N(K_{e2(\gamma)})} \cdot \frac{\Omega(K_{e2(\gamma)})}{\Omega(K_{e2\gamma}^{\mathrm{SD}})}, \tag{15}$$

The detector acceptance is calculated by Monte Carlo simulation. In contrast to the previous KLOE experiment which determined $Br(K_{e2\gamma}^{\mathrm{SD}})$ relative to $Br(K_{\mu2})$, the present experiment was able to disentangle both the number of $N(K_{e2(\gamma)})$ and $N(K_{e2\gamma}^{\mathrm{SD}})$ events directly from the charged particle momentum spectra. The spectrum was decomposed by simulating the spectrum of each contributing process and fitting the linear combination to the measured spectrum. In addition, $Br(K_{e2\gamma}^{\mathrm{SD}})$ was further constrained with the data where a photon was detected in coincidence with the CsI(Tl) calorimeter or the GSC. Details of the $Br(K_{e2\gamma}^{\mathrm{SD}})/Br(K_{e2(\gamma)})$ determination will be described in section 6.2.

3.2 Details of the experiment

The E36 experiment was performed by the upgraded KEKPS-E246 detector and details of the E246 detector system are well documented in Ref. [11, 41, 42]. Here I would like to explain the J-PARC facility, the K1.1BR beamline for the K^+ transportation, and the E36 detector elements, as follows.

3.2.1 J-PARC facility

J-PARC is a high intensity proton accelerator facility (see Fig. 11). It is a joint project between KEK and JAEA and is located at the Tokai campus of JAEA. J-PARC aims for the frontier in material an life science, and nuclear and particle physics, which create high intensity secondary beams of neutrons, hadrons, and neutrinos. J-PARC includes three main parts: the 400 MeV proton linear accelerator, the 3 GeV Rapid Cycling Synchrotron (RCS), and the 30 GeV Main Ring (MR) synchrotron. There are two main experimental areas: the Materials and Life Science Experimental Facility (MLF), where the proton beam from the RCS is used to create beams of either neutrons or muons for further study, and the Hadron Beam Facility, where the beam from the main ring is used to create heavy hadronic particle such as pions and kaons. The main ring beam is also used to create neutrino beams for neutrino oscillation studies at the Kamioka laboratory, located approximately 300 km to the west. A planned project also allow for research into accelerator-driven nuclear waste transmutation. The E36 experiment was performed in the Hadron Beam Facility.

3.2.2 K1.1BR beamline

The K1.1BR beamline was used for the E36 experiment to transport the K^+ beam to the experimental area in the Hadron Beam Facility [43]. Fig. 12 shows the layout of the K1.1BR beamline to transport the K^+ beam to the experimental area. The calculated envelope of the K^+ beam using a TRANSPORT code are shown in Fig. 13(b) in vertical (top) and horizontal (bottom) directions. The black and red lines of the horizontal envelope correspond to the result of the 1st and 2nd order
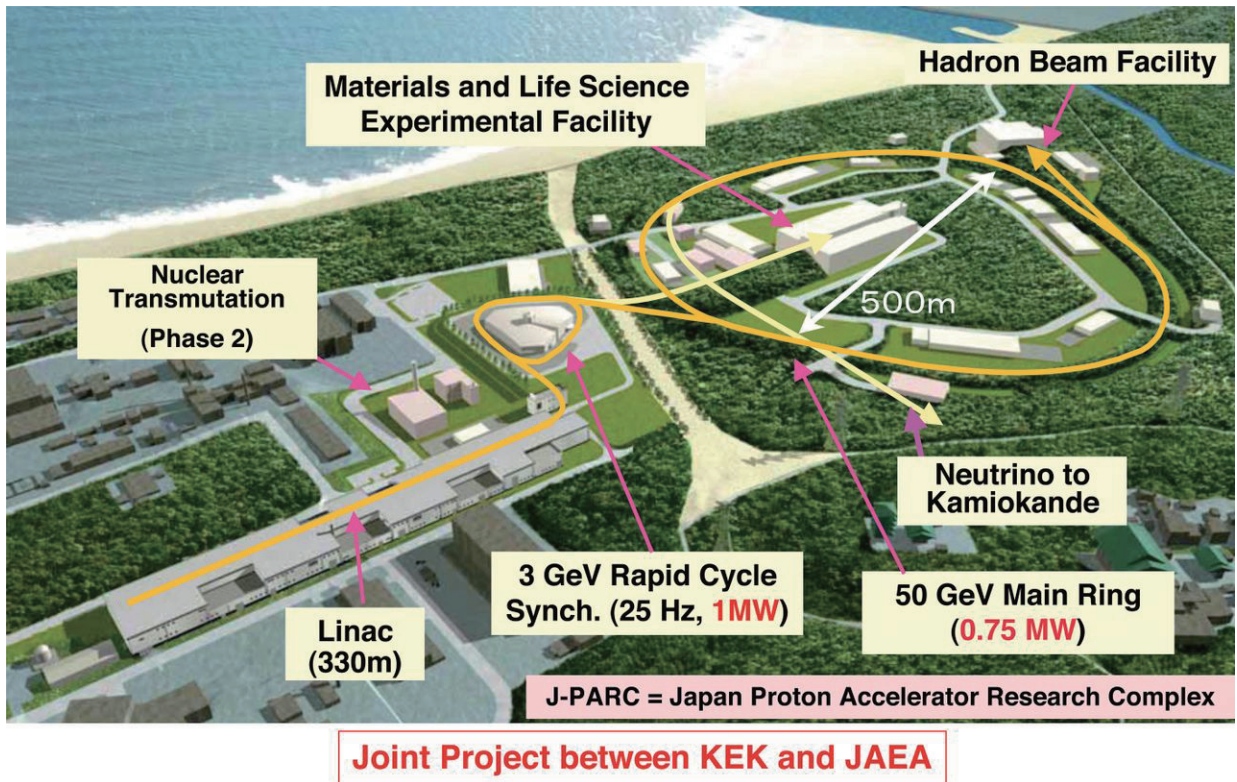
Figure 11: J-PARC is a high intensity proton accelerator facility. J-PARC aims for the frontier in material an life science, and nuclear and particle physics, which creates high intensity secondary beams of neutrons, hadrons, and neutrinos. The E36 experiment was performed in the Hadron Beam Facility.

matrix calculation, respectively. A separated K^+ beam with a low momentum of 0.78 GeV/c with $\pm 3\%$ momentum spread from the K1.1BR was used, which was mainly adjusted by the combination of three dipole magnets of D1-D2-D3. Details of this beam are described in the report submitted to the FIFC in 2007 [44]. The beam optics were designed by J. Doornbos of the TREK collaboration by keeping the upstream layout design of K1.1, as its short branch with a total length of 20.3 m. Although there was only a single electro-static separator (ESS), the existence of a vertical focus (IFY) using the D1-Q1-Q2-D2 elements before the ESS played an important role to improve the K/π ratio. Mass slit 1 (MS1) was located at the IFY position to remove halo component which were generated from K_S decays around the K^+ production target and scattered π^+s during the beam transportation. After MS1, the beam was defocused by the Q3-Q4 doublet and entered into ESS which applied an electric field of ± 300 kV/12 cm in the vertical direction, along with a correction magnetic (CM) field generated by a magnet in the horizontal direction. The Q5-Q6 doublet line-focused the K^+ beam onto mass slit 2 (MS2), and most of π^+s originating from the direct generation at the production target were shifted from the K^+ beam profile at MS2 and rejected because of the mass dispersion of the K1.1BR beamline. The dispersion-free horizontal focus at HFOC after the sector type magnet D3 played an important role in removing any remaining pions by setting an additional slit in the horizontal direction. We obtained a round beam spot using the Q7-Q8 doublet after bending by D3 at the final focus (FF) with a full width at half maximum of 1 cm horizontally and vertically, a K^+ stopping target was placed at FF. The beamline acceptance was estimated to be 4.5 msr%[$\Delta p/p$] using a TURTLE beamline code[2]. The K1.1BR beamline had sextapole and octapole components, however they did not significantly improve the K1.1BR performance. The spot was free from dispersion (R_{16}), but with finite R_{26} [3]. Fig. 13(a) shows a typical mass separation curve which was obtained as a function of the CM field strength. The blue and red lines correspond to counting rates of K^+s and π^+s, respectively, measured by the beam Cherenkov counter (see below). The K^+ beam intensity was 1.0×10^6 with a K/π ratio of ~ 1 in a 2-s spill duration and 6-s repetition rate at 30 kW of accelerator beam power. The parameters of the K1.1BR beamline are summarized in Table 3.

3.2.3 Fitch-type Cherenkov counter for K^+ trigger

Although the K^+ beam was enriched in the π^+ background, it still contained about the same intensity as K^+s. Therefore, it was necessary to make K^+ identification to extract useful K^+ decay events. In order to trigger only on kaons in the beam, we prepared a Fitch-type differential Cherenkov counter (beam Cherenkov counter) [45], whose structure is as shown in Fig. 14 and whose parameters are given in Table 4. The basic principle of the particle identification made use of different Cherenkov angle from the acrylic radiator when the K^+ and π^+ beams passed the radiator. Kaons and pions vertically entering into a 40 mm-thick acrylic radiator emit Cherenkov light with characteristic polar angles according to their velocities. Namely, the Cherenkov angle were 38° for K^+ and 47° for π^+ at 780 MeV/c. Since the critical angle of acrylic for the total reflection is 42.2°, the Cherenkov light from K^+s was refracted at the rear surface (exited from the surface) while that of π^+s was reflected (total reflection). The Cherenkov light from pions is reflected by a mirror around the radiator and

---

[2]msr is milli(m) steradian(sr).

[3]R_{16} and R_{26} are the elements of the 1st-order transport matrix. R_{16} is the measure of horizontal dispersion, and R_{26} is the measure of focusing point depth in the experimental target.
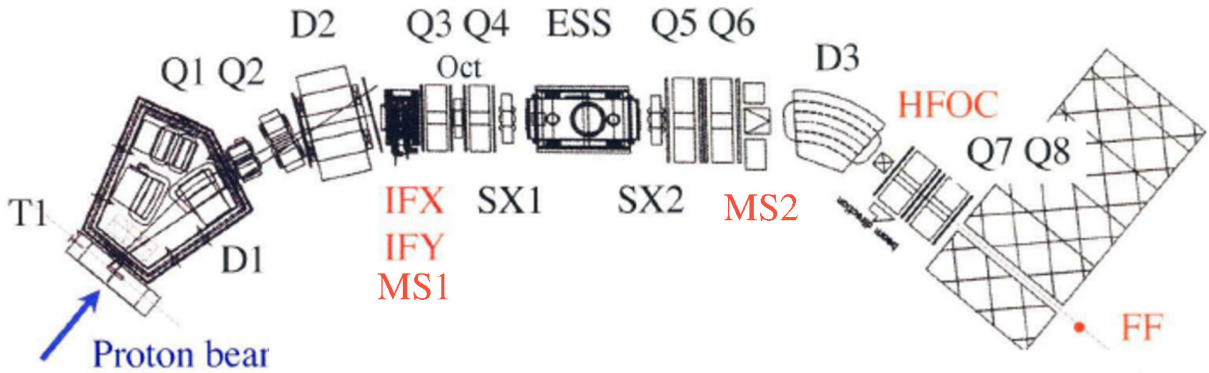
Figure 12: Layout of the K1.1BR beamline. Although there is only a single electro-static separator (ESS), the existence of a vertical focus (IFY) before the ESS played an important role to increase the K/π ratio. D1−D3 are bending magnets and Q1−Q7 are quadrupole magnets. SX and OCT are the sextupole and octapole magnets, respectively. Most of π^+ background were rejected by combining slits at MS1, MS2, and HFOC. Details of this beam is described in the report submitted to FIFC in 2007 [44].
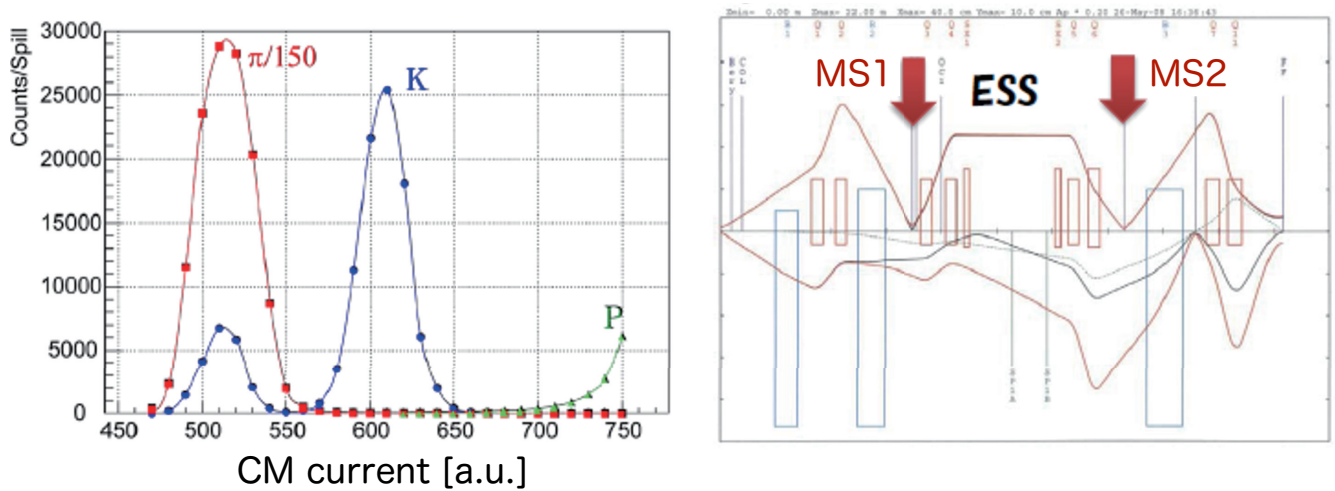
Figure 13: (a) Typical mass separation curve which was obtained as a function of the CM field strength and (b) calculated envelope of the K^+ beam using a TRANSPORT code in vertical (top) and horizontal (bottom) directions. The black and red lines in (a) correspond to counting rates of K^+s and π^+s, respectively, measured by the beam Cherenkov counter. The black and red lines of the horizontal envelope correspond to the result of the 1st and 2nd order matrix calculation, respectively.

24

Table 3: Main parameters of K1.1BR. A separated K^+ beam with low momentum (0.78 GeV/c) from the K1.1BR beamline was used in the E36. Details of this beam are described in the report submitted to FIFC in 2007 [44].

Operation beam momentum	780 MeV/c
Extraction angle	6 degree
Length of the beam line	20.3 m
DC separator	single stage
K^+ intensity at FF	1×10^6/2s
K^+/π^+ ratio at FF	~ 1
Beam spot size at final focus	1 cm [H], 1 cm[V] (FWHM)
R_{16}, R_{26}	$R_{16} <$0.1 cm/%, R_{26}=17.6 mr/%
Acceptance	4.5 msr% ($\delta p/p$)
Momentum bite	± 3%
Position of MS1	-1.4 and 1.92 mm
Position of MS2	-1.4 and 2.9 mm
Position of IFX slit	-80 and 80 cm
Position of HFOC slit	-15 and 15 cm

detected by an inner photomultiplier (PMT, Hamamatsu R1398) ring (π-ring). The light from kaons was reflected by a backward parabolic mirror and detected by an outer PMT (Hamamatsu R58UV) ring (K-ring). Each ring was composed of 14 PMTs with a Winston cone at the entrance. However, due to the finite K^+ beam emittance, beam particles cannot enter the Cherenkov radiator vertically, which do not satisfy the above ideal reflection and refraction conditions, and some photons cannot reach the PMT. In order to solve this problem, the threshold level to the number of the hit PMTs (PMT multiplicity) was set to 7, and the K^+ efficiency was obtained to be higher than 99% (see section 4.2). This can be considered that Cherenkov photons from the radiator can be detected half of the PMTs even for the case of large incident angle.

This counter was very similar to the counter developed for the KEK E246 experiment, but the momentum range was different. The designed momentum range is $740-800$ MeV/c, whereas the original momentum range was $620-700$ MeV/c. We modified the focal length of the K-ring parabolic mirror to compensate for the Cherenkov emission angle shift due to this momentum difference. The PMT hit multiplicity in each ring was used for an online trigger.

3.2.4 K^+ stopping target

The kaons were slowed down by a BeO degrader and stopped in an active target, which consist of 256 3.1×3.1 mm^2 thin scintillating bars of 20-cm length forming a cylindrical bundles with a 5.6-cm diameter, located at the center of the detector assembly. A segmented active target identified the stopping kaon and its decay vertex, and provide the initial tracking information for decay particles as well as energy-loss correction to the momentum determination in the spectrometer. The fine
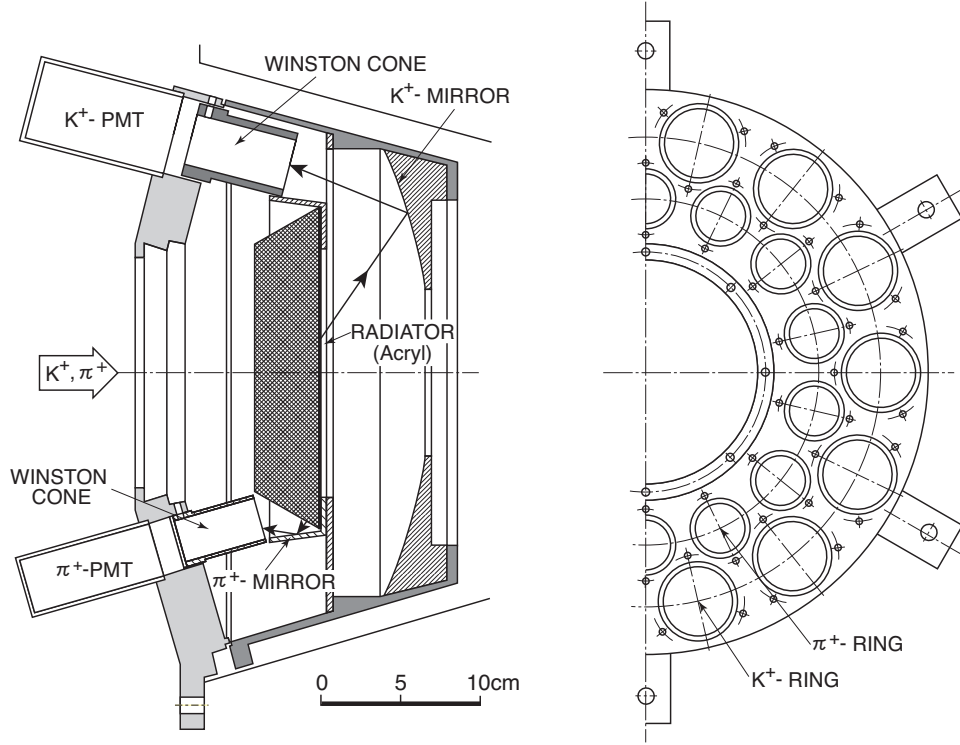
Figure 14: Side view and end view of the beam Cherenkov counter. The beam with $740-800$ MeV/c momentum emits the Cherenkov light with an angle of $38°$ for K^+ and $47°$ for π^+. The critical angle of the radiator for the total reflection is $42.2°$.

Table 4: Main parameters of the beam Cherenkov counter. The K^+ momentum is expected to be $740-800$ MeV/c. The K^+ efficiency is obtained to be higher than 99% by setting the threshold level of a PMT hit multiplicity at 7 among 14.

Parameter	Value
Accepted K^+ momentum	$740-800$ MeV/c
Radiator material	acrylic ($n_D = 1.49$)
Effective aperture	12-cm diameter
Number of PMTs	14 for kaon and 14 for pion
K^+ efficiency	>99%
π^+ misidentification as K^+	<1%

segmentation was also necessary to suppress backgrounds in reconstructed trajectories. Therefore, this segmentation level is a trade-off between position resolution and rate handling from fine segmentation on the one hand, and energy and timing resolution from minimum ionizing particles on the other hand. The radial extent of the target was optimized to match the kaon beam profile, while minimizing the material to be traversed by exiting decay positrons and photons from the $K_{e2\gamma}^{\mathrm{SD}}$ decays. In each fiber a thin wavelength shifter (WLS) fiber was embedded in a groove and the light through the about 1 m WLS fiber was read by a multi pixel photon counter (MPPC) i.e. a Geiger mode APD from Hamamatsu. An input of a sufficient number of photons into the MPPC was successfully observed. The K^+ stopping efficiency was typically $\sim$0.25 relative to the number of K^+ obtained by the Fitch Cherenkov counter. Other K^+s stopped in the degrader or stuck out from the degrader-target system before reaching the target due to hadronic interaction with a degrader material. A K^+ track was identified by the prompt timing with high energy deposit and the K^+ decay vertex was determined by the intersection of this K^+ track and the outgoing lepton track determined from the spectrometer analysis (see section 4.3). The K^+ stopping profile had a round shape with a Gaussian-like distribution with $\sigma_z \sim 4$ cm in the beam direction.
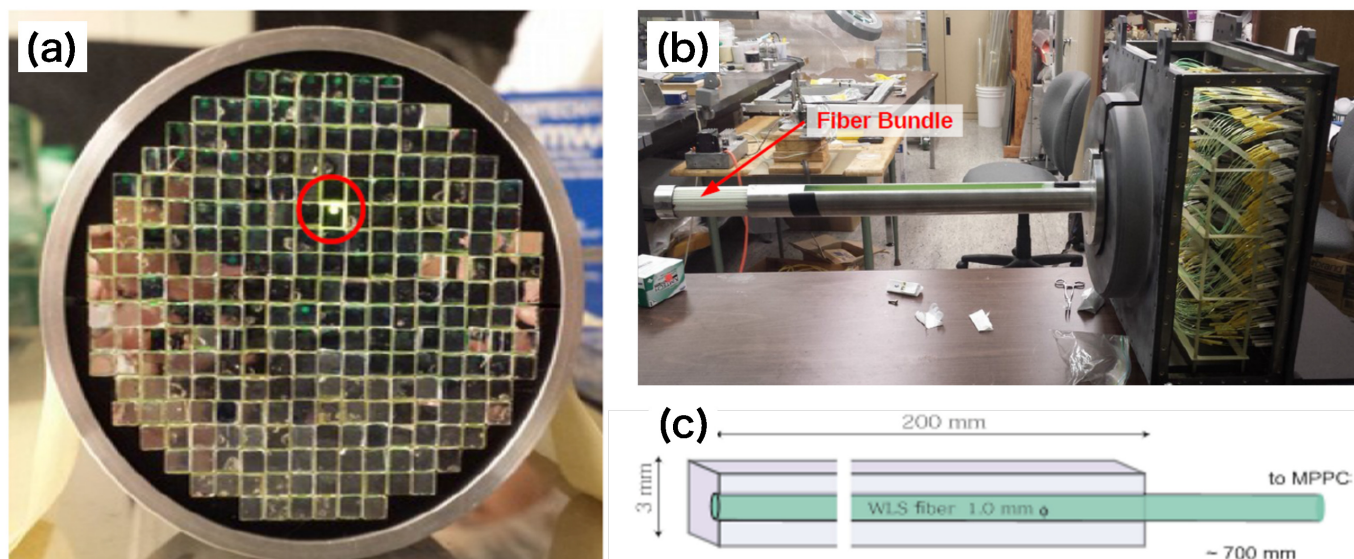
Figure 15: (a) and (b) are front view and end view of the active target. (c) is the schematic view of a scintillating bar with the WLS fiber readout. The active target consisted of 256 3.1×3.1 mm^2 thin scintillating bars of 20-cm length forming a cylindrical bundles with a 5.6-cm diameter. In each fiber, a thin wavelength shifter fiber was embedded in a groove and the light through the about 1 m WLS fiber was read by a MPPC.

3.2.5   Spectrometer and tracking system

The superconducting toroidal magnet, comprising 12 identical sectors, has rotational symmetry of 30 degrees. Each sector comprises an iron core and superconducting coil. The coil was made of winding of NbTi-Cu monolithic wire cooled by two-phase helium. Each iron sector was magnetized

Table 5: Parameters of the toroidal magnet

Parameter	value
Total weight	38 tons
Number of sectors	12
Pole gap	20 cm
Pole face	82×76 cm^2
Conductor	NbTi-Cu
Maximum field	1.83 T
Maximum field on wire	2.5 T
Ampere-turns per coil	369 kA
Operation current	1150 A at 1.5 T
	434.0 A at 0.65 T
Stored energy	2.2 MJ

by the coils, and a field up to 1.8 T can be excited. The parameter of the toroidal magnet are listed in Table 5, and some details concerning this magnet are described elsewhere [41, 46]. Each spectrometer gap has a uniform gap size (20 cm) with a rectangular pole face (82×76 cm^2 in the radial and beam directions). The number of sectors (12) was determined by optimizing the solid angle for charged particles and field strength. To realize a large solid angle and wide momentum acceptance with relatively small detectors, a quasi-focal plane was formed at the gap exit. Thus, a sold angle of more than 6% ×4π str as well as a wide momentum range of 220 to 260 MeV/c was achieved at 1.5 T.

The field distribution of the spectrometer was given as a superposition of the dipole field from the iron core and the toroidal field from the coils. The field map of the magnet was calculated by a three-dimensional field code "TOSCA" [47]. In the setting of 1.8 T, an iron saturation effect is large. Charged particles from the target located in the center of the magnet were bent by ∼90 degrees and tracked by the SFT and MWPCs at the entrance and exit of the gap. The validity of the map was checked using the measured monochromatic momentum spectra of muons from $K_{\mu2}$ and pions from $K_{\pi2}$.

Charged particles from the target were tracked and momentum-analyzed using the above four trackers, as shown in Table 6. For the C2, C3, and C4 chambers, we reused the existing MWPC chambers which were used in the previous E246 experiment. They were placed at the entrance (C2) and exit (C3, C4) of each magnet gap, as shown in Fig. 9. Since the C2, C3, and C4 chambers have to be operated under the strong field of the spectrometer, a planar MWPC with cathode readout was adopted. The anodes were 20-μm gold-plated tungsten wires strung with 2 mm pitch along the momentum-sensitive directions (the beam direction for C2 and radial direction for C3 and C4). The two cathode planes were located above and below the anode wires, and the distance between the cathode and anode planes was 6mm. The cathode plans were made of a 25 μm Kapton foil with copper coating strips of 18 μm in thickness. The width of the strip was 9 mm in width and the spacing between strips was 1 mm. A mixed gas of Ar (50%) and ethane (50%) was used as the operating gas whih was supplied C2-C3-C4 in series for each gap and finally discharged outside the Hadron Hall
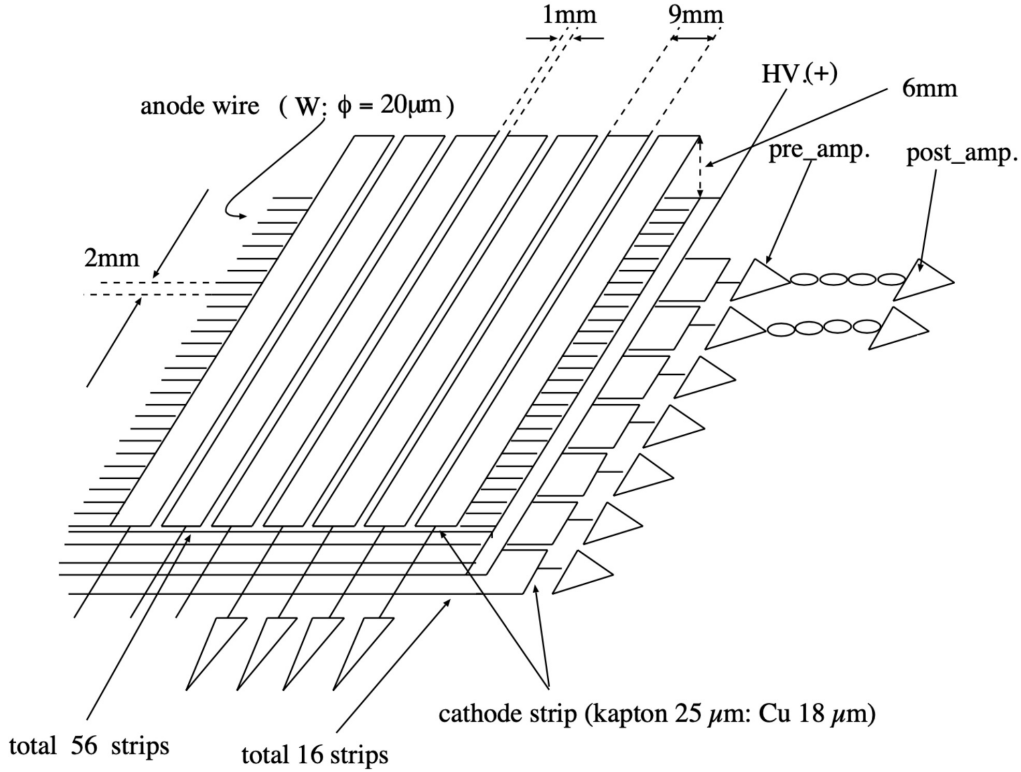
Figure 16: Schematic view of C2, C3, and C4 chambers. The two cathode planes, made of a 25 μm Kapton foil with Cu coating, are located above and below the anode plane. The distance between the cathode plane and the anode wire was 6mm. The width of the strip on the cathode was 9mm with 1 mm spacing.

through a exhaust port. High voltage of +4.0 kV was supplied to the anode, and the cathode was connected to ground. The induced charge on the cathode plane was absorbed by the pre-amplifier, and was converted into an electric signal by the pre-amplifier and the post-amplifier, and measured by the charge-sensitive ADC. Typical position resolutions of the C2, C3, and C4 chambers were $\sim$200 μm. Parameters of the MWPC chambers are summarized in Table 6.

In order to reject in-flight-decay events and scattered events during the transportation through the spectrometer, an additional tracker element was essential which should be placed near the K^+ stopping target to satisfy redundant conditions in the momentum determination. The vertex detector for the beam direction (SFT) has to be accommodated inside of the CsI(Tl) calorimeter together with the target, TOF1 scintillators and the aerogel counter, as shown in Fig. 17. A novel technique was employed to spiral the pre-made scintillating fiber ribbons around a thin drum and to read out light from both ends of the ribbons. Unfortunately, the photon yields from the both ends were not very high, and it was difficult to keep the detection efficiency of 100%. In the designing the SFT, it was essential to wind the fiber ribbons clockwise and counter-clockwise to have two different helicities with positive θ_L and negative θ_R in order to obtain a crossing point in orthogonal projection between

Table 6: Parameters of the C2, C3 and C4 MWPCs. Since the C2, C3, and C4 chambers have to be operated under the strong field of the spectrometer, a planar MWPC with cathode readout was adopted.

	C2	C3	C4
Effective area ($x \times y$ mm^2)	560×160	640×200	720×200
Half gap		6 mm	
Anode wire		gold plated tungsten, $\phi = 20$ μm	
Anode pitch		2 mm	
Cathode strip		9 mm width and 1 mm spacing	
		18 μm Cu on 35 μm Kapton film	
Gas mixture		Ar 50% + Ethane 50%	
Operation voltage	3.9 kV	4.0 kV	4.0 kV
Resolution		less than 200 μm for up to 10° inclined incident	

fibers in different layers [4]. Here, it was essential to take different $|\theta_L|$ and $|\theta_R|$ in order to resolve the degeneracy of azimuthal angle ϕ determination. Thus, different ribbon widths must be adopted for the left-helicity and right-helicity ribbons, and the number of 1 mm fibers in the ribbons was adopted as $N_L = 15$ and $N_R = 17$. This choice enabled the structure with two L-helicity layers and two R-helicity layers, which can raise the overall SFT detection efficiency. The development of the SFT winding is schematically illustrated in Fig. 17, showing a single layer from each helicity with 17-fiber L-helicity and 15-fiber R-helicity ribbons. A charged particle produces a signal in both the L- and R-ribbons. The relevant hit fibers are indicated with a blue strip for the L-helicity and a red one for the R-helicity. However, it is not known in which turn of the ribbon the occurs and there are several candidates of the intersection points, as shown in Fig. 18. By using the azimuthal angle information from the MWPC analysis, the real hit position can be uniquely determined which can provide the correct z-coordinate with an accuracy equal to the fiber diameter. Plastic scintillating fibers Kuraray SCSF-78MJ of 1 mm diameter and Hamamatsu MPPC S10362-11-50C were chosen for the SFT fibers and their photon readout.

The particle hit position in the z direction, Z_{12} for layer12 (right helicity) and Z_{34} for layer34 (left helicity), can be expressed using the number of turns (n_{12} and n_{34}) as,

$$Z_{12} = (\theta' + 2\pi n_{12}) \cdot l_{12}/2\pi + \frac{f_{12} - 0.5}{15} \cdot l_{12} - 10 - Z_{12}^0 \tag{16}$$

$$Z_{34} = (\theta + 2\pi n_{34}) \cdot l_{34}/2\pi + \frac{f_{34} - 0.5}{17} \cdot l_{34} - 10 - Z_{34}^0 \tag{17}$$

$$l_{12} = \frac{w_{12}}{\cos \phi_{12}} \tag{18}$$

$$l_{34} = \frac{w_{34}}{\cos \phi_{34}} \tag{19}$$

---

[4]This smart idea was originally invented by H. Kawai, Chiba University
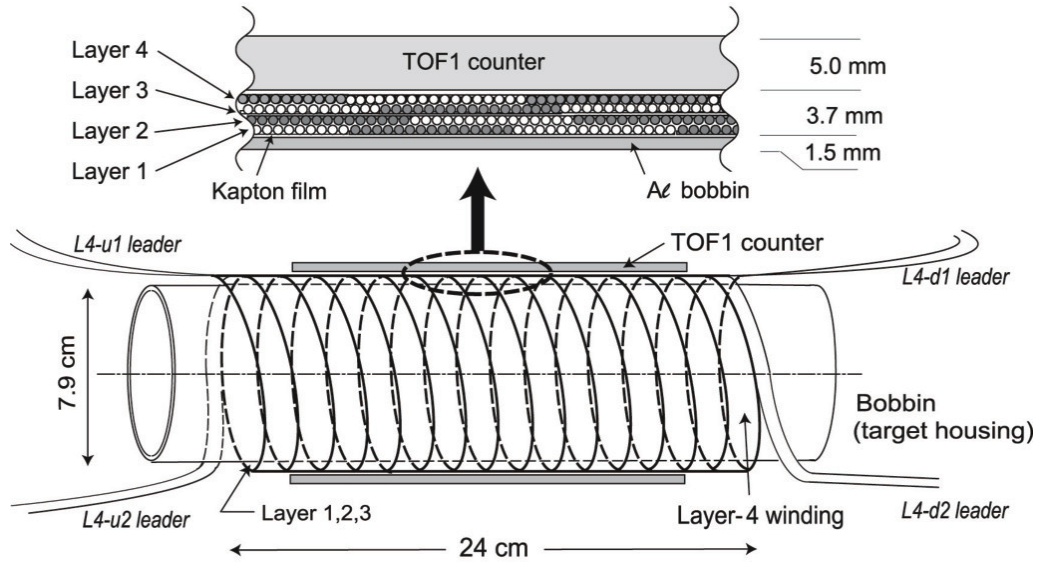
Figure 17: Schematic view of the SFT assembly. Only the winding of the 4th layer is shown for simplicity. The cross section of the four coiled ribbon later is shown enlarged, where open and filled circle indicate neighboring turns of the same ribbon. The ribbons are separated at each end into two bundles for routing the fibers to the photo-devices.
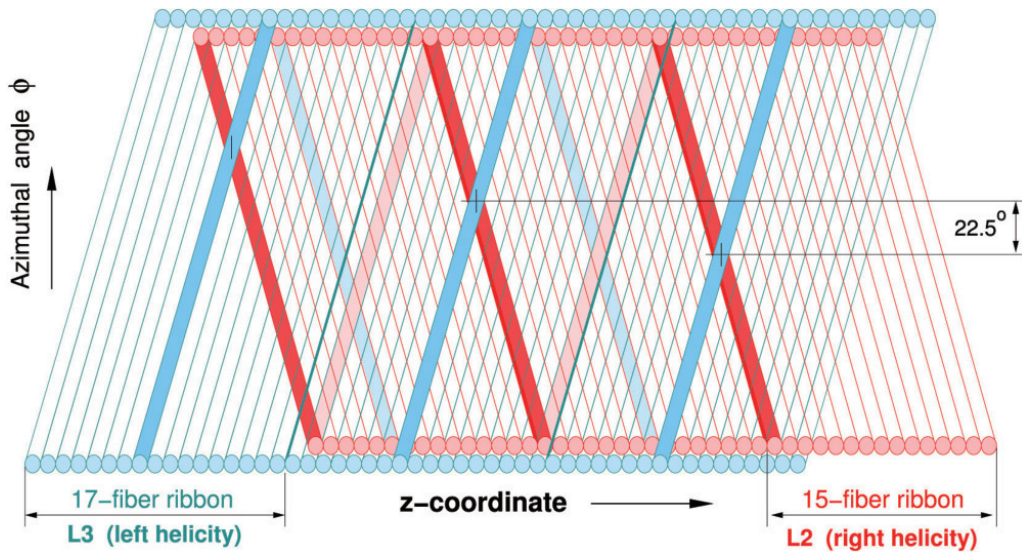
Figure 18: Development of the SFT coil schematically drawn with the exaggerated stereo angle. The L-helicity ribbon with 17 fibers and R-helicity ribbon with 15 fibers are indicated in blue and red, respectively. The azimuthal angle ϕ of crossing point of the hit fibers changed by 22.5 degree from turn to turn.

31

$$\sin \phi_{12} = \frac{w_{12}}{\pi d_{12}} \tag{20}$$

$$\sin \phi_{34} = \frac{w_{34}}{\pi d_{34}} \tag{21}$$

where θ and θ' are the angles in x-y plane looking from downstream and upstream of SFT, respectively, as shown in Fig. 19. The hit fibers are denoted as f_{12} and f_{34} with the condition of $0 \leq f_{12} - 0.5 \leq 15$ and $0 \leq f_{34} - 0.5 \leq 17$, ϕ is stereo angle for the ribbon winding, and w is the ribbon width (l is 1 turn effective width in z direction). Here the initial Z position of the ribbon winding, Z_{12}^0 and Z_{34}^0 are introduced in Eq. (16),(17), where the condition of $0 \leq Z_{12}^0 \leq l_{12}$ and $0 \leq Z_{34}^0 \leq l_{34}$ are satisfied. The Z^0 values have to be experimentally determined using the tracking information (see below). The fiber ribbons for Layer12 (34) are wound in clockwise (counter-clockwise) direction looking from downstream. Therefore, Z_{12} increases with decreasing θ' and increasing f_{12}, and Z_{34} increases with increasing θ and increasing f_{34}.

Here, requiring the conditions of

$$Z_{12} = Z_{34}, \tag{22}$$

$$\theta' + \theta = 2\pi, \tag{23}$$

the θ angle of the fiber intersection point (θ_{SFT}) can be determined by substituting Eq. (22),(23) into Eq. (16),(17) to be

$$\theta_{SFT} \cdot (\frac{l_{12} + l_{34}}{2\pi}) = (n_{12} + 1)l_{12} - n_{34}l_{34} - \frac{f_{12} - 0.5}{15} \cdot l_{12} + \frac{f_{34} - 0.5}{17} \cdot l_{34}$$
$$- Z_{12}^0 + Z_{34}^0 + l_{12} \tag{24}$$

Because of the condition of $l_{12} \neq l_{34}$, it can be easily understood that θ_{SFT} jumps by $\delta\theta_{SFT} = \pi/8$ in adjacent turns and varies in the entire SFT region depending on n_{12} and n_{34} values. Using the charged particle tracks obtained by the target and spectrometer analysis, n_{12} and n_{34} can be determined to minimize the difference of θ_{SFT} and θ_{track}. The associated Z value (Z_{SFT})is finally calculated from n_{12}, n_{34}, f_{12}, and f_{34} to be

$$Z_{SFT} = \frac{l_{12}l_{34}}{l_{12} + l_{34}} \cdot (n_{12} + 1 + n_{34}\frac{f_{12} - 0.5}{15} + \frac{f_{34} - 0.5}{17} - h_{12} - h_{34})$$
$$- 10. \tag{25}$$

Here h_{12} and h_{34} parameters describing the initial Z^0 values are introduced as,

$$Z_{12}^0 = h_{12}l_{12} \tag{26}$$

$$Z_{34}^0 = h_{34}l_{34} \tag{27}$$

where $0 \leq h_{12} \leq 1$, $0 \leq h_{34} \leq 1$.

Any efficiency difference of SFT and MWPCs between e^+ and μ^+ would introduce a systematic uncertainty into the R_K measurement. In the E36 experiment, the redundancy in the number of chambers allows to directly determine the chamber efficiencies. In principle, it is possible to reconstruct the particle trajectory using three tracking elements. Since four tracking elements were used for the track reconstruction, the efficiency was determined by comparing signals from a particular element with the tracks reconstructed by others. For example, SFT signals are checked by reconstructing particle tracks from C2, C3, and C4. Details are discussed in Section 4.4.
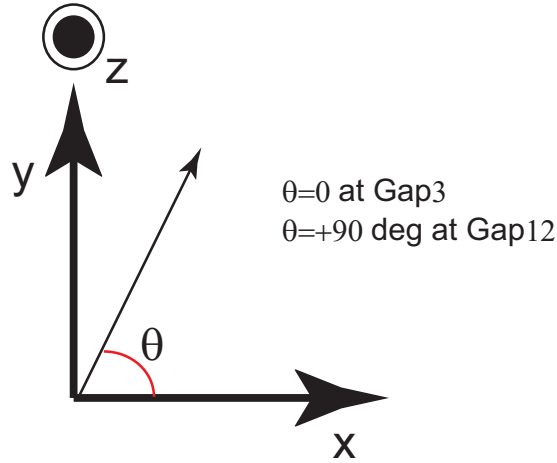
Figure 19: The definition of θ angle in the local coordinate of the E36 experiment. $\theta = 0°$ and $90°$ corresponds to the Gap3 and Gap12 direction, respectively.

3.2.6 Particle identification

Because of the huge difference of the K_{e2} and $K_{\mu2}$ branching ratios, $Br(K_{e2})/Br(K_{\mu2}) \sim 10^{-5}$, reliable discrimination of K_{e2} is very important to remove the $K_{\mu2}$ contamination. In order to satisfy these conditions, the simultaneous use of an AC counter, a PGC counter, and a TOF measurement between TOF1 and TOF2 were adopted in the E36 experiment.

TOF measurement Particle discrimination between the e^+ and μ^+ mainly for the low energy region is carried out by a time-of-flight measurement between TOF1 and TOF2 (see Fig. 20). The TOF1(TOF2) counter size and thickness were 200×20 mm^2 and 5 mm (800×200 mm^2 and 200 mm), respectively. TOF1 was located surrounding the K^+ target system and TOF2, which consist of two TOF2 counters arranged without gaps in the azimuthal direction, was located about 90 cm behind C4 resulting in a typical path length of 2.7 m from TOF1, as shown in Fig. 9.

Fast response BC404 plastic scintillator was used as the TOF counter materials. Hamamatsu H3171-03 and H1161 photomultiplier (PMT) were used for TOF1 and TOF2, respectively, which were set both ends of the counters. The main parameters of the counters for the TOF measurement are summarized in Table 7. Output signal of both the PMTs were sent to the counting room through co-axial cables. The output signal was divided into two signals by an analog divider. One of them was sent to the leading edge discriminator and the other was sent to a charge sensitive ADC. For timing adjustment, the output signal of the discriminator and the other was sent to a charge sensitive ADC. For the timing adjustment, the output signal of the discriminator was delayed by using co-axial cable and fed to a high resolution TDC of 25 ps/channel. The time difference between the e^+ and μ^+ from the K_{e2} and $K_{\mu2}$ decays is approximately 0.5 ns for a typical trajectory. The uncertainty of the light propagation time from the particle hit position to the photo multiplier is suppressed by reading signals from both ends of the TOF counters. For optimal separation of K_{e2} and $K_{\mu2}$, a timing resolution of $\sigma_t = 150$ ps for the TOF measurement was needed, however the actually timing

33

Figure 20: The TOF2 counter. The counter size was 800×200 mm² and 200 mm, which was located about 90 cm behind C4 resulting in a typical path length of 2.7 m from TOF1.

Table 7: Main parameters of TOF1 and TOF2. The TOF resolution was obtained to be $\sqrt{(250 \text{ ps})^2 + (100 \text{ ps})^2} \sim 260$ ps.

	size (mm²)	thickness (mm)	scintillator	PMT	resolution (ps)
TOF1	200×30	5	BC404	H3171-03	250
TOF2	800×200	20	BC404	H1161	100

resolution in the E36 experiment was obtained to be 260 ps. Note that the TOF2 counters were used for the $K_{\mu 2}$ trigger and the TOF1 counters were used as the detector to define the fiducial region of the K^+ stopping target in the beam direction.

AC Cherenkov counter A threshold type silica (SiO₂) aerogel Cherenkov (AC) counter [48] was used for the e^+ identification, which was installed surrounding the TOF1 counter, as shown in Fig. 21. This type of a Cherenkov counter is widely used for particle identification by many experiments such as BELLE [49]. Since it was placed in front of the magnet gap, namely before charged particle spectroscopy, it was highly necessary that the detector was made of light materials. The β value of μ^+ from $K_{\mu 2}$ is 0.913, therefore a Cherenkov radiation material with refractive index (n) from 1.01 to 1.095 is necessary to discriminate e^+ and μ^+. Normally, the refractive index of aerogel ranges from 1.01 to 1.08, and an increase of Cherenkov photons with increasing refractive index is expected, so that we choose an aerogel material with n of 1.08 to obtain the highest photon yield. The typical number of Cherenkov photons per e^+ passing through this counter was estimated to be about 500, and a wavelength region of photons measured by this counter ranges from 350 nm to 700 nm. An opening angle of Cherenkov radiation with respect to the e^+ trajectory is as small as 35.5°. Thus, the minimization of the path length for the Cherenkov photon transport to the photon detector was a key issue to maximize number of photons emitted from the aerogel. The AC system was composed of 12 counter units corresponding to the magnet gaps, which had up- and down-stream symmetry. Two aerogel tiles with a thickness of 20 mm and a length of 18 cm were mounted in a housing box, as shown in Fig. 21. Cherenkov photons were mostly emerging into the air gap and they were reflected
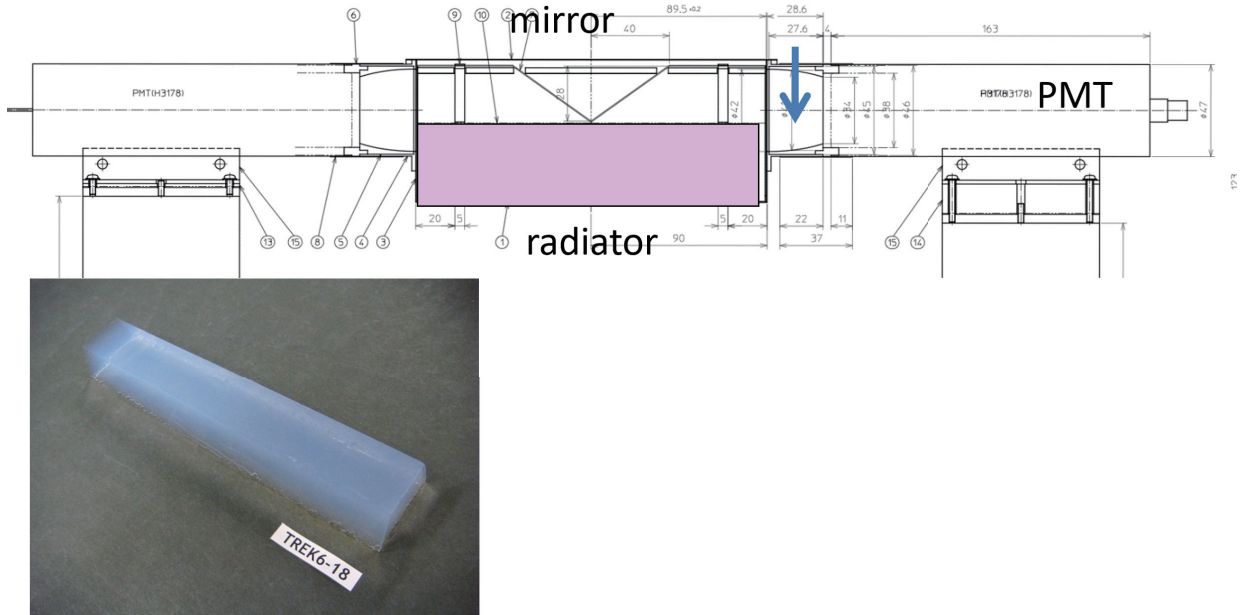
Figure 21: The experimental configuration of the aerogel Cherenkov counter in a unit. The AC system was composed of 12 counter units corresponding to the magnet gaps, which had up- and down-stream symmetry, which were placed surrounding the TOF1 counter system.

by a special-shape mirror in the box, then collected through a Winston cone on each end. Solar blind PMTs (Hamamatsu H3178) shielded by a μ-metal magnetic material located at the both ends of the AC detector were used as a photo sensor to operate properly in a non-negligible magnetic field from the toroidal magnet.

Lead glass Cherenkov (PGC) Counter   In a lead-glass material, a positron generates an electromagnetic shower, but not the case for a muon. Therefore, Cherenkov photon yield in lead-glass material produced by a positron hit is much higher than that by a muon hit, the particle identification can be performed by comparing pulse heights generated from a photon detector. The lead-glass modules used in the TOPAZ experiment at KEK TRISTAN [50] have been adopted as the PGC for use in the J-PARC E36 experiment. The module mass is 26.7 kg, and the size is 122 mm (7.2 radiation length) in thickness and 340 mm in length. The top surface of each module is tilted at an angle of 3.72 deg. so that the height of a module increases linearly from 113 to 135 mm. The lead-glass material is SF6W; the chemical composition and physical properties are summarized in Ref. [50]. They were assembled with 7 modules stacked in a radial direction behind the TOF2 counters, as shown in 22. The lead-glass surfaces were mirror-polished, and a Hamamatsu R1652 [51] phototube was attached to the block for the Cherenkov photon detection. This configuration will allow us to construct a compact detector with enough thickness to contain most of the shower energy generated by the e^+s from K_{e2} decay. In the E36 experiment, using a polyethylene degrader of 10 cm to slow down the charge particle momentum in front of the PGC, the PGC performance was highly improved

35

Figure 22: The PGC system was assembled with 7 lead-glass modules stacked in a radial direction behind the TOF2 counters. A polyethylene degrader of 10 cm in front of the PGC slowed down the charge particle momentum and improved the PGC performance as a PID detector

by making a more difference between the e^+ an μ^* Cherenkov photon yields [52].

3.2.7 CsI(Tl) calorimeter for photon measurement

The photon detector, a barrel of 768 CsI(Tl) crystals, covered ∼70% of the total solid angle [41, 53, 54]. There are 12 holes for outgoing charged particles and 2 holes for the beam entrance and exit, as shown in Fig. 23. Each crystal had a coverage of 7.5° along both the polar and azimuthal directions. The length of the CsI(Tl) crystal was 25 cm (13.5 radiation length), which was enough to obtain sufficient energy resolution as well as avoid nuclear counter effects from the rear end. However, the hardware threshold at 17 MeV unfortunately made deterioration of the energy resolution (see section 4.7.3). Parameters of the calorimeter are summarized in Table 8. Since the CsI(Tl) calorimeter had to be operated under relatively strong fringing field from the toroidal magnet where PMTs would be difficult to use, the PIN photodiode (PIN diode) were employed to read out the scintillation light of the CsI(Tl) crystals. Due to the compactness of the PIN diode, the length of the CsI(Tl) modules. Each crystal with the associated PIN diode and the pre-amplifier was assembled in an Al container of 0.1 mm thickness. The charge sensitive pre-amplifier with a time constant of 600 μs and a gain of 0.5 T/pC was directly attached to the PIN diode.(Fig. 24) Very high yield of 11,000 photo-electrons/MeV and very low noise level of ENL (equivalent noise level)=65 keV were achieved due to good light collection and large size of PIN diodes. The output signals from the pre-amplifier was clipped by a pole-zero-compensation method giving 44 μs time constant and fed to a shaping amplifier with 1 μs shaping time.

The waveforms of the shaping amplifier were recorded by VF48 flash ADC manufactured by the
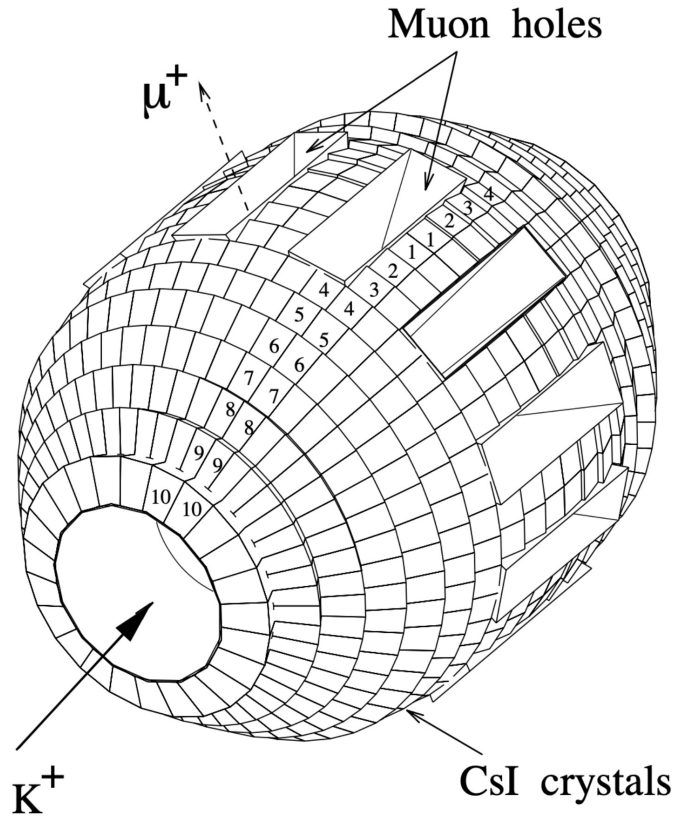
Figure 23: Schematic view of the CsI(Tl) calorimeter which comprised 768 CsI(Tl) crystals and covered 70% of of the total solid angle. There were 12 holes for the outgoing charged particles and 2 holes for the beam entrance and exit.
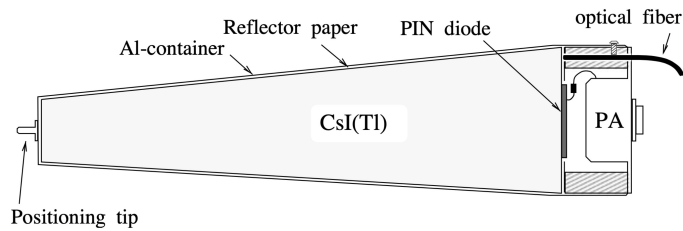
Figure 24: Schematic cross section of a CsI(Tl) crystal module. Scintillating light was converted to an electric pulse by the PIN diode and charge sensitive pre-amplifier. The length of the CsI(Tl) crystal was 25 cm (13.5 radiation length), which was enough to obtain sufficient energy resolution as well as to avoid shower leakage from the rear end.

Table 8: Main parameters of the CsI(Tl) calorimeter

Parameter	value
Segmentation	$\Delta\theta = \Delta\phi = 7.5°$ (partly $\Delta\phi = 15°$)
Number of crystals	768
Length of crystals	25 cm (13.5 X_0)
Inner radius	20 cm
Outer radius	50 cm
Solid angle	75% of 4π
Total weight of crystals	1.7 ton
Readout	PIN diode (18×18 mm, partly 28×28 mm)
Light yield	11,000 photoelectrons / MeV
Equivalent noise level	65 keV
Energy resolution	$\sigma_E/E = 3.0\%$ at 200 MeV
Position resolution	$\sigma_p = 1.0$ cm
Time resolution	$\sigma_T = 6.5$ ns for $E = 10-220$ MeV
π^0 mass resolution	$\sigma_{\pi^0} = 14$ MeV/c^2 for $K_{\pi2}^+$

TRIUMF national laboratory [55]. VF48 had 10 μs time range to be operated with a 25 MHz external clock signal. In order to reduce the data size of VF48, a hardware threshold at $\sim$17 MeV was set.

3.2.8 Gap sandwich counter for photon measurement

The gap sandwich counter (GSC) was installed to detect the escaping photons passing through the holes in the calorimeter, as shown in Fig. 25 [5] The GSC was a standard Pb-plastic sandwich detector with 2.7 radiation length which was set in each sector at the outer radius of the magnet pole. Photon conversion efficiency in the Pb plate was not 100% and this effect was taken into account in the simulation calculation. There were four layers, and the size of each layer was 900 mm×196 mm and thickness was 3.7 mm (10 mm) for Pb(plastic). The scintillation photons from the four plastic layers were transported to the phototubes through acrylic light guide. Due to the geometrical restriction, the scintillation photons were collected from one end (upstream) of the detector. The GSC signal was converted into a logic signal by the leading-edge discriminator by setting a particular threshold level and fet to TDC.

The CsI(Tl) calorimeter only covered the finite acceptance of the photon measurement. All of the radiated photon from the $K_{e2\gamma}^{SD}$ decay cannot be detected only by the calorimeter, and a part of the escaping photons through the hole hit the GSC counters. The photon detection by the calorimeter and the GSC counter is alternative, and therefore, the consistency check of the $K_{e2\gamma}^{SD}$ result obtained by independent the CsI(Tl) calorimeter and the GSC analysis is very important for the reliable

---

[5]The GSC was originally installed to "veto" the escaping photon in the KEK-PS E470 experiment.
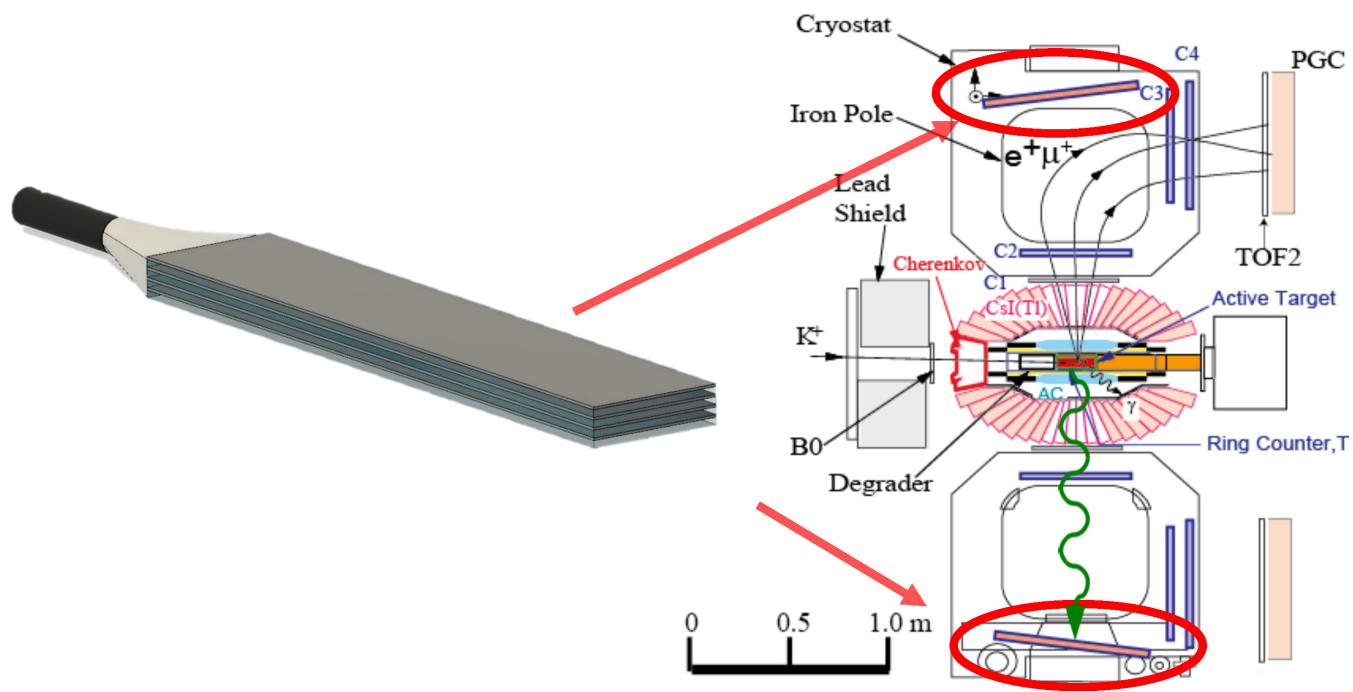
Figure 25: Schematic view of the GSC counter. The GSC counter was installed to detect the escaping photons passing through the holes in the calorimeter. We can measure the radiated photon from the $K_{e2\gamma}^{\mathrm{SD}}$ decay using the GSC counter, as well as the CsI(Tl) calorimeter.

Table 9: Detectors and readout devices

Detector	Number of channels	ADC	TDC
Beam Hodoscope	24		VT48 (625 ps)
Fitch Cherenkov	28		VT48 (625 ps)
TOF counter	72	TKO ADC	TKO HR-TDC (25 ps)
Trigger Counter	17	CAEN V792	VT48 (625 ps)
Lead Glass Counter (PGC)	84	CAEN V792	VT48 (625 ps)
Gap Sandwith Couner (GSC)	12	CAEN V792	VT48 (625 ps)
Aerogel Cherenkov (AC)	24	TKO ADC	VT48 (625 ps)
MWPC (C2, C3, C4)	496	TKO ADC	
Fiber Target	256	Network EASIROC	
Spiral Fiber Tracker (SFT)	128	Network EASIROC	

$Br(K_{e2\gamma}^{\mathrm{SD}})$ determination, although the GSC cannot provide the energy information of the radiative photon. Note that single rate of GSC was very low, which was located far from the beam line and the spectrometer field swept out charged particles, and accidental backgrounds in GSC was much lower than those in CsI(Tl).

3.2.9 Electronics and data acquisition

The data acquisition (DAQ) subsystems of the detectors were not unified by the effective readout of its detectors and had three type s of the readout interfaces, TKO, VME, and the TCP/IP Ethernet network. Table 9 summarizes the detector elements and their readout devices.

TKO is a KEK local standard DAQ readout developed for the KEK experiments in the 1980's. The data in the TKO front-end modules are collected and stored in the partner memory module. TKO was used to readout the 25-ps high-resolution TDCs for the TOF counters and the ADCs for the AC, TOF, and MWPCs in the E36 experiment. VME was used to read ADCs (CAEN V792) and TDCs (TV48) for PGC, GSC, AC, and several other counters. VT48 is a multi-hit TDC with 625-ps time-counter developed at TRIUMF. VME was also applied to read the waveform of CsI(Tl) with VF48 FADCs. VF48 is a 10-bit FADC module developed at TRIUMF, which can sample tha data at up to 60 MHz. In the E36 experiment, a sampling frequency of 25 MHz was applied to read the CsI(Tl) signal. A network-oriented SiPM readout board was used to read the MPPC signals of the fiber target and SFT. This board had a controller and a TCP/IP network engine both based on FPGA.

Fig. 26 shows the configuration of the DAQ network. We used the common network to integrate many different type of the DAQ subsystems. The DAQ system had controllers which can connect to the network. The performance of the network interfaces and network switches were sufficiently high to transfer all detector data. The data rate was estimated be around 20 MB/s, while The current network technology can handle over 100 MB/s of data flow. The common high-speed storage devices such as the RAID hard disk drive can record data faster than 100 MB/s. Therefore, we designed a network based distributed DAQ system to integrate various readout systems. An overview of the

network based distributed DAQ system is shown in Fig. 26.
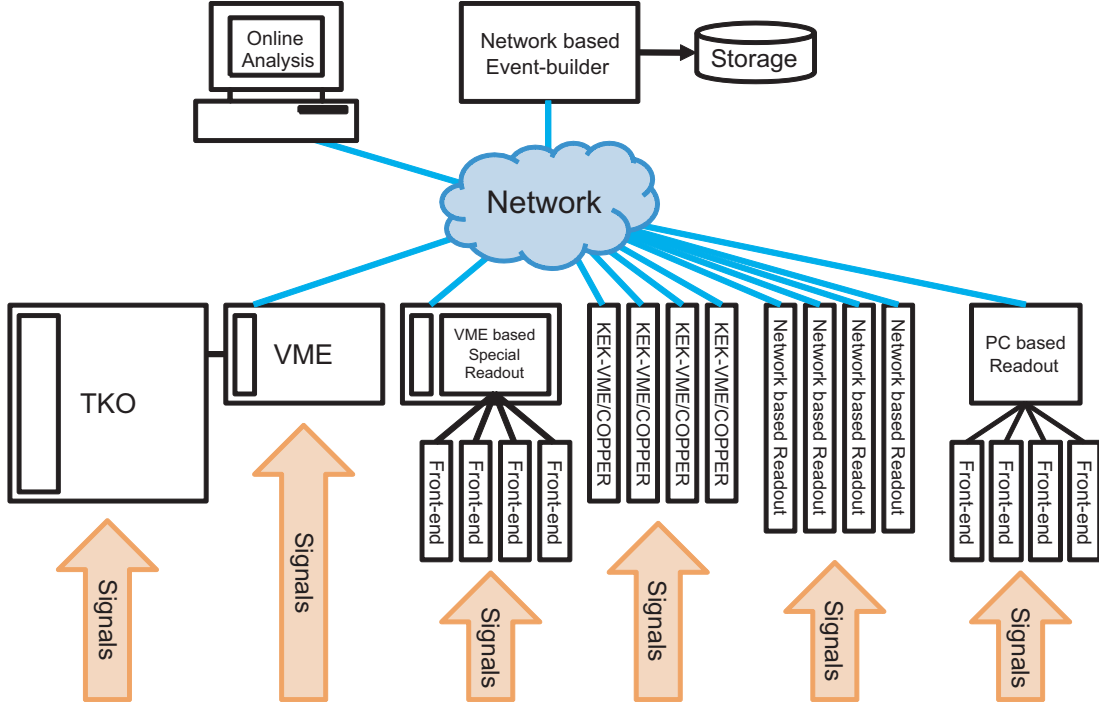
Figure 26: Network DAQ system

3.2.10 Event trigger for the J-PARC E36 experiment

In the E36 experiment, the $K_{e2(\gamma)}$ and $K_{e2\gamma}^{\mathrm{SD}}$ decays at rest were accepted by analyzing charged particle momenta using the toroidal spectrometer. Therefore, the following conditions were required for the trigger construction as

- The K^+ particle came to the experimental area through the K1.1BR beamline.

- The K^+ entered the K^+ stopping target and decayed.

- The secondary charged particle from the K^+ decay hit TOF1, passed through the spectrometer gap, and hit TOF2.

- There was the finite transit time in the target due to K^+ lifetime.

Therefore, a basic trigger logic was made using the signals from the detector elements of the beam Cherenkov counter, K^+ stopping target, TOF1, and TOF2 as

$$TRG = C_K \otimes Tar \otimes \Sigma_i^{12}[TOF2_i \otimes (TOF1_{i-1} \oplus TOF1_i \oplus TOF1_{i+1})] \tag{28}$$

where

41

- C_K is the multiplicity condition of the Cherenkov K-ring > 7 (see section 3.2.3),

- Tar is the energy deposit in the target,

- $TOF2_i$ is the counter TOF2 hit condition in the ith magnet sector,

- $TOF1_{i-1} \oplus TOF1_i \oplus TOF1_{i+1}$ is the hit condition in the ith TOF1 counter or its adjacent counter.

Here C_K is necessary to discriminate K^+ from π^+ by the beam Cherenkov counter. The Tar, $TOF1$, and $TOF2$ requirements are to confirm that a charged particle was transported from the kaon stopping target and reached TOF2 through the toroidal spectrometer. C_K and $TOF1$ carried the timing of the incoming K^+ and the outgoing secondary particle, respectively, and a wide coincidence window for C_K and $TOF1$ was set to 60 ns ($5\times K^+$ lifetime). Using the above TRG condition, the major K^+ decay components such as $K_{\mu2}$ and $K_{\pi2}$ are selected and the data cannot be taken by the E36 DAQ system. In order to solve this problem, a mixed trigger scheme was adopted in the E36 experiment as

- Requirement of an AC and PGC coincidence with very low threshold levels for the e^+ selection safely at the trigger stage. The $K_{e2(\gamma)}$, $K_{e2\gamma}^{\mathrm{SD}}$, etc. are efficiently chosen.

- Thinning out TRG to reduce the trigger rate and DAQ dead time. The $K_{\mu2}$ events are collected and used for the R_K analysis by correcting for this reduction factor.

Therefore, an event was accepted when the following mixed trigger requirements were satisfied:

$$TRG \otimes AC \otimes PGC \oplus TRG \otimes SC(\mathrm{N}), \tag{29}$$

where AC and PGC are the signals from AC and PGC, respectively, and $SC(\mathrm{N})$ is a preset-scaler with a scaling factor of N. It should be noted that no requirements for the photon measurement were applied at the trigger stage and any CsI(Tl) and GSC data were accepted. A typical TRG rate was 125 k trigger/s which was subject to the $K_{\mu2}$ rate. Adopting the N parameter to be 0.02, the trigger rate was reduced down to 2.5k trigger/s, where the trigger from the $K_{e2(\gamma)}$ and $K_{e2\gamma}^{\mathrm{SD}}$ was still negligible. This trigger rate could be easily controlled by changing the N value to match the DAQ capability. Since all decay modes were collected simultaneously, normalization of the stopped kaon number does not contribute to the systematic uncertainties at all.

4 Analysis of $K_{e2\gamma}^{\mathrm{SD}}$ and $K_{e2(\gamma)}$ decays using the E36 detector system

4.1 Calibration for ADC and TDC data

During the E36 experiment, we sometimes changed the experimental conditions such as trigger timing, high voltage to detectors, cable length, cable swapping, trigger logic, etc., and the ADC and TDC data were affected by these modifications. In particular, in the beginning of the E36 experiment, these conditions were often changed for the hardware tuning. In order to remove these effects, we performed the data calibration of all detectors to correct ADC pedestal, ADC gain, and TDC time0 as,

- **ADC pedestal**
  AC, target fibers of low and high gains, TOF1 counter, TOF2 counter, PGC, GSC, SFT of low and high gains, MWPC

- **Time zero offset**
  AC, target fiber, TOF1counter, TOF2 counter, PGC, GSC, SFT, Beam Cherenkov counter

- **ADC Gain**
  AC, target fibers of low and high gains, PGC, MWPC

Peak positions were automatically determined by fitting the spectra using a Gaussian or asymmetric Gaussian function. However, correctness of the calibration was checked by eye using the special scanning technique[6].

In the beginning of the E36 experiment, the data were taken during the commissioning runs dedicated to K^+ beam and PID detector tuning. They were used as systematic-control data (Crun), in which the $K_{\mu2}$ background events increased. After finishing the commissioning, the data were stably collected, which are entitled as physics runs (Prun). The E36 analysis was mainly performed using the Prun data, and the Crun data were used for the estimation of systematic effects due to the $K_{\mu2}$ background subtraction uncertainty.

4.2 K^+ Analysis

K^+ beam particles were identified by the beam Cherenkov counter, and mis-identification is not a problem because these events are easily rejected by other analyses. The K^+ decay vertex was determined as intersection point of a K^+ track and an e^+ or μ^+ track in the scintillating fibers of the target. Although the DC separator in the K1.1BR line was in operation, the beam likely still contained about the same number of π^+. Therefore, it is essential to pick up the K^+ by using the K-ring PMT. The K^+/π^+ separation using the multiplicity cut of K-ring and π-ring PMTs was quite

---

[6]This technique was developed by S.Kimura and A.Kobayashi

satisfactory. Since K^+ produce a signal in the K-ring with high multiplicity and in the π^+-ring with low multiplicity, we can set the threshold to a certain value of the multiplicity for both the K-ring and π-ring PMTs in order to extract the K^+ particles, as shown in Fig. 27.
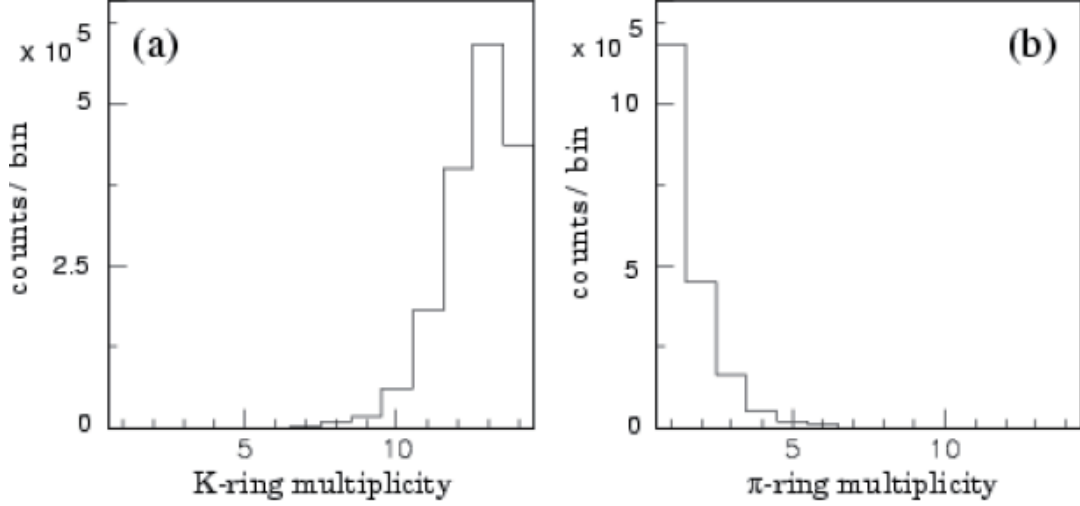

Figure 27: Distribution of PMT-hit multiplicity obtained using the physics run data. (a) is for the K-ring multiplicity and (b) is for the π-ring multiplicity, when a K^+ passed the beam Cherenkov counter. By setting a threshold for the PMT multiplicity to 7, the K^+ efficiency is expected to be higher than 99%. The π^+ mis-identification probability as K^+ is less than 1%.

In the case of in-flight K^+ decay, the momentum of e^+ and μ^+ was modified and a systematic bias would be introduced in the event reconstruction of $K_{e2(\gamma)}$ and $K_{e2\gamma}^{\mathrm{SD}}$. Since the E36 Monte Carlo simulation started from K^+ decays at rest, in-flight K^+ decays were not taken into account. Therefore, the simulation could not reproduce in-flight K^+ events and we should remove these in-flight decays by the event selection cuts. The most reliable quantity to reject these events in the timing of the beam Cherenkov counter. Events with the in-flight K^+ decays concentrate around the prompt timing obtained by the beam Cherenkov counter. The K^+ stopping condition in the target was checked by using the timing information of the beam Cherenkov counter, because in-flight K^+ decays occurred promptly, while the events due to stopped K^+ were delayed following an exponential curve with the K^+ lifetime of 12.4 ns, Here, the timing of an incoming K^+ (K-time) was determined by the average time of the K-ring PMTs by measuring time difference of the $K+$ decay time determined by TOF1. The K-time distribution selected with the conditions of 2γ hits in the calorimeter and $p > 230\,\mathrm{MeV}/c$, which mainly accepted in-flight K_{e3} and $K_{\mu3}$ decays, has a peak structure at 0 ns with an exponential tail part, as shown in Fig. 28. This prompt peak is enhanced/enriched by selecting apparent in-flight K^+ events using the above conditions. In order to reduce the $K_{\mu2}$ contribution as low as possible, 2γ from π^0 decay were required in the CsI(Tl) analysis. This peak position corresponds to the prompt timing and is fitted by a Gaussian function with $\sigma \sim 0.8$ ns. The time constant of the tail part was obtained to be $\sim$12 ns which is consistent with the proper K^+ lifetime. In the present analysis, the K-time cut point was set to 1.5 ns, as shown in Fig. 28 indicated by green dotted line, and the

systematic uncertainty should be estimated by changing this cut point (see systematic uncertainty section). The faction of the in-flight K^+ decay was determined by fitting the K^+-time distribution selected with the normal conditions (not specific for the in-flight K^+ decay) to be 3.3%. Then, the in-flight K^+ fraction after the prompt cut was estimated to be 0.1%.
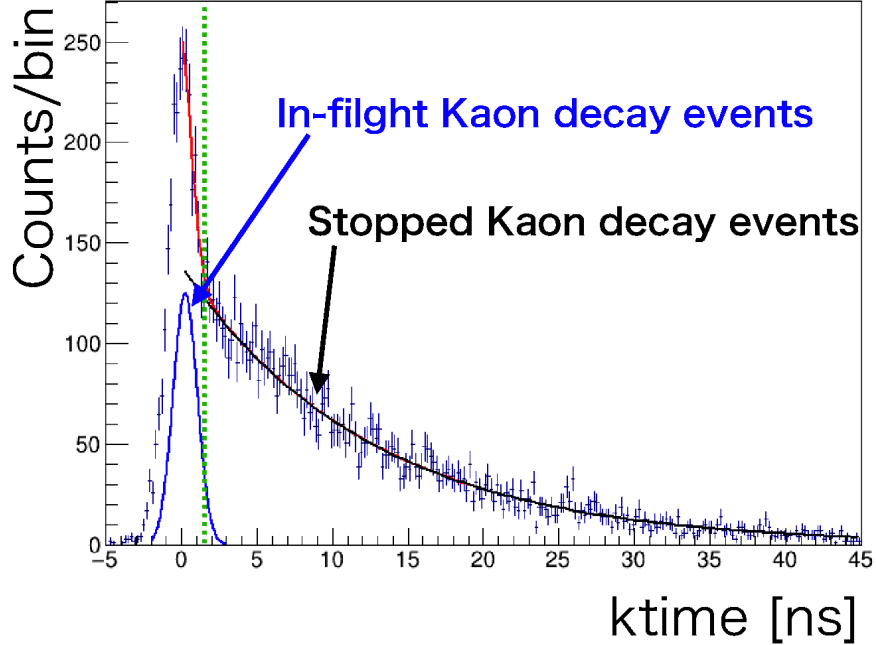
Figure 28: The K-time distribution selected with the conditions of 2γ hits in the calorimeter and $p > 230$ MeV/c. The peak structure around 0 ns represents in-flight kaon decay events. The tail component with the time constant of 12 ns corresponds to stopped kaon events. The K-time cut point was set to 1.5 ns, indicated by green dotted line.

4.3 K^+ Stopping distribution obtained by active K^+ target

The K^+ decay vertex was determined by checking the pattern of the K^+ track and secondary charged particle track in the scintillating fiber target. For the incoming K^+ beam, the energy deposit in one of the fibers was much larger than that for decay particles emitted radially from the target. Also, the timing of the incoming K^+ coincided with the beam Cherenkov counter, while that of the outgoing particle was delayed. The K^+ track was recognized from the energy deposit and timing information of each fiber and the e^+/μ^+ track was determined by the spectrometer analysis (see below in the tracking section), and the intersection point was treated as the K^+ decay vertex in the x-y plane. Typical event displays of the fiber target using the ADC data are shown in Fig. 29, where red lines are the e^+/μ^+ track was determined from the spectrometer tracking analysis. Fig. 30 shows the K^+ stopping distribution in the x-y plane, in which the K^+ vertex is concentrated at the central part of the target.
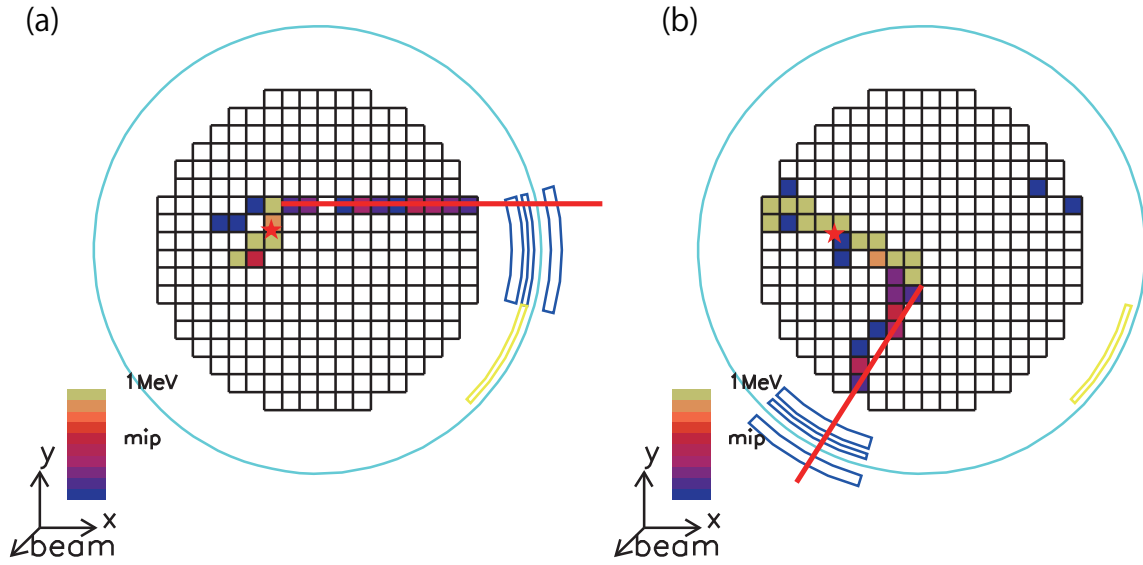
Figure 29: Typical event display of the fiber target obtained using the ADC data. The brightness is proportional to energy deposit in each fiber. A kaon trajectory has large energy deposit while a decay particle trajectory has only minimum ionization loss.
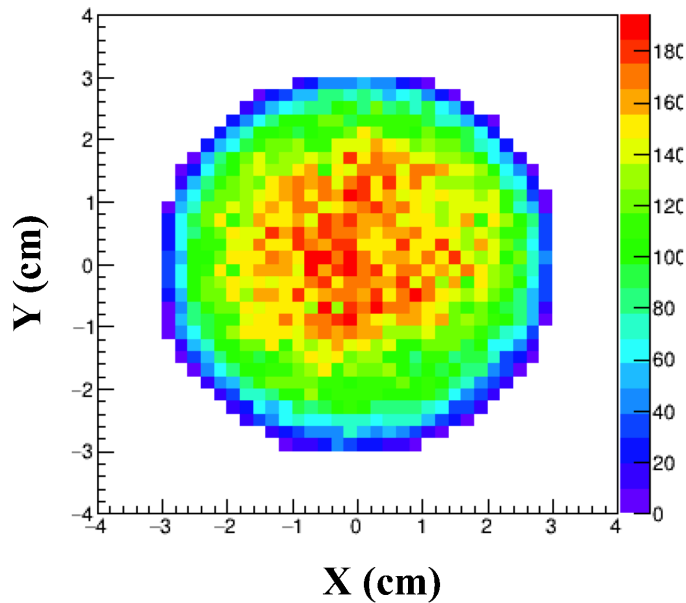
Figure 30: The K^+ stopping distribution in the x-y plane. The intersection point of the K^+ track and trajectory obtained from the spectrometer analysis was adopted as the K^+ decay vertex. The K^+ vertex is concentrated at the central part of the target.

4.4   Momentum determination of charged particles

4.4.1   Hit position determination in tracking detectors

Charged particles from the target were tracked using 3MWPCs C2, C3, and C4, as well as by the edge lepton fiber in the target and SFT. A hit position of the chambers was calculated from the induced charges on the cathode strips by the so-called charge ratio method. The passage of a charged particle induces a point-like charge avalanche at some point on the anode wire, thus producing the charge distribution along several cathode strips. In the current analysis, we required signals at least two neighboring strips to reduce inefficiency due to broken channels in amplifiers and ADCs. The determination of the SFT [56, 57, 58] hit position is explained in section 3.2.5. About 70% of the events can be determine the intersection point of the left- and right- handed layers, however we have to use the single layer information for remaining 30% events. The analysis and calibration procedures are summarized in technical note [59].

4.4.2   Momentum determination by track reconstruction

Charged particle momentum (p) was calculated by reconstructing a track under the spectrometer field using a Runge-Kutta tracking method. A trajectory of charged particles could be determined by assigning the following 5 parameters : (1) hit position of the x and y coordinates in the MWPC plane, (2) azimuthal and polar angles of charged particles, (3) momentum at C4 chamber. Since the single rate of the C3 and C4 chambers was relatively low, the track was reconstructed by tracing back to the target system from C4 and the parameters at C4 were adopted in the tracking analysis. These parameters were determined in an iteration calculation so as to minimize the χ^2 value defined as,

$$\chi^2 = \Sigma(v_{fit,i} - v_{data,i})^2/\sigma_i^2 \tag{30}$$

where i is the number of the tracking devices. v_{fit} and v_{data} are the calculated and experimental hit position of the ith devices, respectively. The spatial resolution of the tracker in the simulation and the weight parameters σ were carefully tuned to reproduce the experimental residual distributions by the simulation. Here it should be noted that we can separate the tracking analysis into two methods depending on the SFT hit pattern. In the 5p- an 5s-tracking, the SFT hit position obtained as intersection point and single layer (only hit fiber selection), respectively, were used for the momentum determination. In the χ^2 calculation, separate weight parameters for the 5p- and 5s-tracking were introduced. The χ^2 distribution obtained in the tracking analysis is shown in Fig. 31(a) for the experimental data (black) and the simulation (red) . Since the peak position of this residual distribution is located around 0 cm, the fitting should be successful by constrained by the SFT hit position. Also, the distance of the K^+ decay vertex from the track is shown in Fig. 31, although this constraint was not sensitive to the momentum determination. The reconstructed trajectories are displayed in Fig. 32(a).

Here, p is the momentum in the spectrometer (outside the target) and should be corrected for the energy loss in the target. The K^+ vertex was determined by extrapolating the reconstructed trajectory into the target. For the incoming K^+ beam, the energy deposit in each fiber is much larger than for decay particles emitted radially from the target. The K^+ fibers were selected by requiring the energy deposit higher than 5 MeV. The 3-dimensional K^+ vertex is interpreted as the point on the
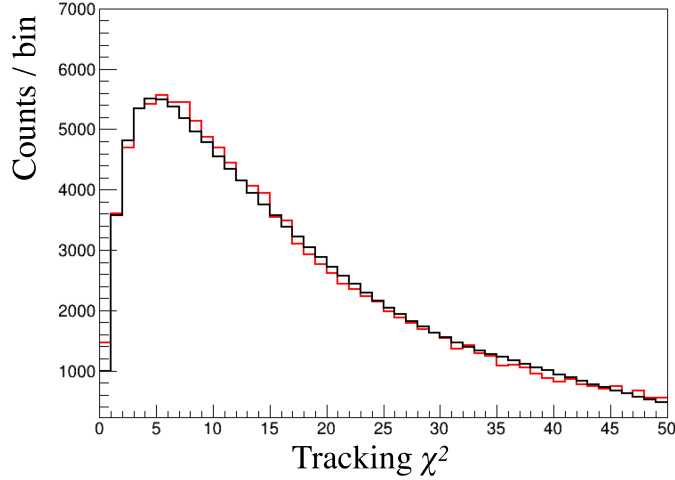
Figure 31: The χ^2 distribution obtained in the tracking analysis for the experimental data (black) and the simulatiion (red).

trajectory which is the nearest position from the K^+ fibers. The energy loss correction in the target was performed using flight pass length in the target. The observed momentum was once converted to the range in plastic and the momentum at birth was obtained using the corrected range* of (range + path length). The momentum spectrum before imposing the PID analysis is shown in Fig. 32(b). Two peaks due to $K_{\mu 2}$ and $K_{\pi 2}$ decays are clearly visible, although the $K_{\pi 2}$ events are reduced due to the lower spectrometer acceptance.Since the spectrometer field was optimized for $K_{e2(\gamma)}$, π^+s from $K_{\pi 2}$ decays were steeply bent in the spectrometer and a probability to reach TOF2 decreased. The momentum resolution is obtained to be 2.0 MeV/c at 235 MeV/c, which is dominated by energy loss fluctuation in the target.

4.4.3 K^+ stopping distribution

The K^+ stopping distribution can be determined by projecting the K^+ decay vertex in x, y, and z directions. Since we can just observe the K^+ distribution corrected for the spectrometer acceptance, it is very difficult to determine the original kaon stopping distribution. Note the observed K^+ distribution depends on the decay channel (Needless to say the original distribution is identical). In order to correct for the spectrometer acceptance and to determine the original kaon stopping distribution, the $K_{\mu 2}$ events of the experimental and MC data were used.

Here, the observed kaon stopping distribution density in z direction, $\rho_{obs}(z)$, can be represented by the original one, $\rho_{org}(z)$, as,

$$\rho_{\mathrm{obs}}(z) = \int \varepsilon(z, p_e)\rho_{\mathrm{org}}(z)dp_e, \tag{31}$$

where $\varepsilon(z,\ p_e)$ is the spectrometer acceptance as a function of e^+ momentum vector p_e and position z. Here, the momentum acceptance of the spectrometer depends on z , and this effect has to be corrected to determine the K^+ stopping profile in the z direction. It is impossible to determine the
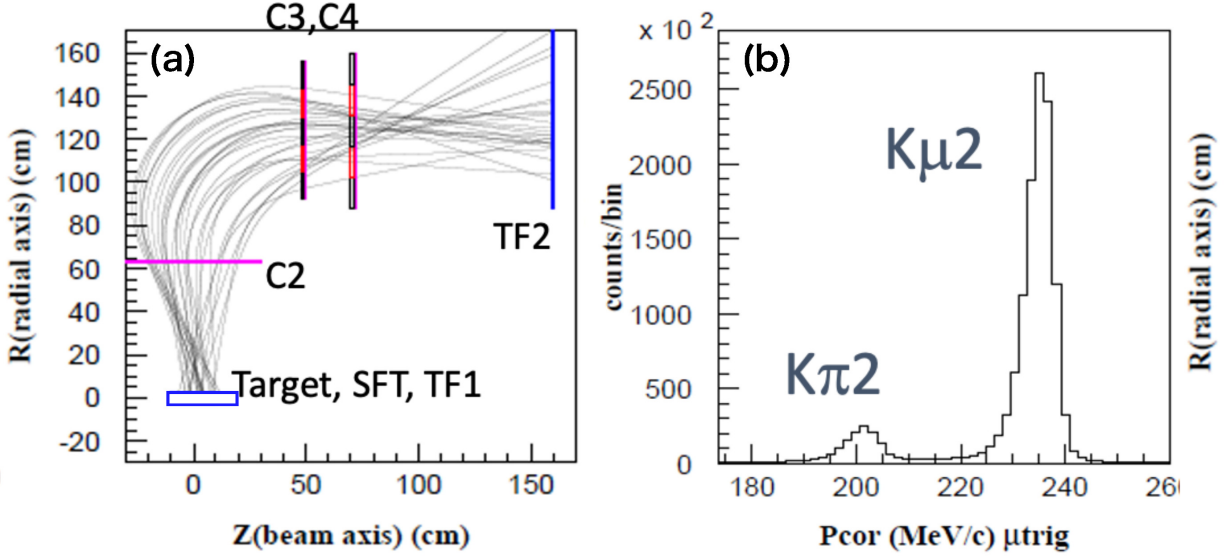
Figure 32: (a) Particle trajectories obtained in the tracking analysis and (b) the momentum spectra corrected for the energy loss in TGT before the e^+ requirement by the PID system. The charged particle momentum was calculated by reconstructing the track under the calculated spectrometer field using a Runge-Kutta tracking method. The peak structure due to the predominant $K_{\mu2}$ and $K_{\pi2}$ decays is seen at 236 MeV/c and 205 MeV/c, respectively.

$\varepsilon(z,\, p_e)$ acceptance experimentally, and $\rho_{\rm obs}(z)$ has to be calculated by the Monte Carlo simulation, in which the $\varepsilon(z,\, p_e)$ effect was automatically taken into account. Here, the acceptance information can be purely extracted from the observed $\rho_{\rm obs}^{\rm (MC)}(z)$ distribution in the simulation assuming $\rho_{\rm org}(z) = 1$ flat original distribution as,

$$\rho_{obs}^{(MC)}(z) = \int \varepsilon(z, p_e) dp_e. \tag{32}$$

Figure 33 (left) shows the $\rho_{\rm obs}^{\rm (MC)}(z)$ (red) and $\rho_{\rm obs}^{\rm (exp)}(z)$ (blue) distribution using the $K_{\mu2}$ events. Therefore, it is possible to reproduce the experimental $\rho_{\rm obs}(x)$ distribution using the original K^+ distribution of

$$\rho_{\rm org}(z) = \rho_{\rm obs}^{\rm (exp)}(z)/\rho_{\rm obs}^{\rm (MC)}(z) \tag{33}$$

in the simulation calculation. We studied this K^+ stopping distribution using the $K_{\mu2}$ events because of high statistical accuracy, and we also confirmed the kaon position density obtained using the K_{e3} and $K_{\mu3}$ events are consistent with the above result.

In order to estimate a systematic uncertainty due to imperfect reproducibility of the K^+ stopping distribution, we compared the experimental $\rho_{obs}^{\rm (exp)}$ of the $K_{\pi2}$ events with the simulation results taken int account the above original K^+ distribution, as shown in Fig. 33 (right). Since the π^+ tracks in the spectrometer were far from the central trajectory, it is very difficult to reproduce the $K_{\pi2}$ experimental conditions by the simulation. Because of this inaccurate $K_{\pi2}$ acceptance function, these distributions are slightly different, and this effect was estimated as the systematic uncertainty of the $Br(K_{e2\gamma}^{\rm SD})$ value.
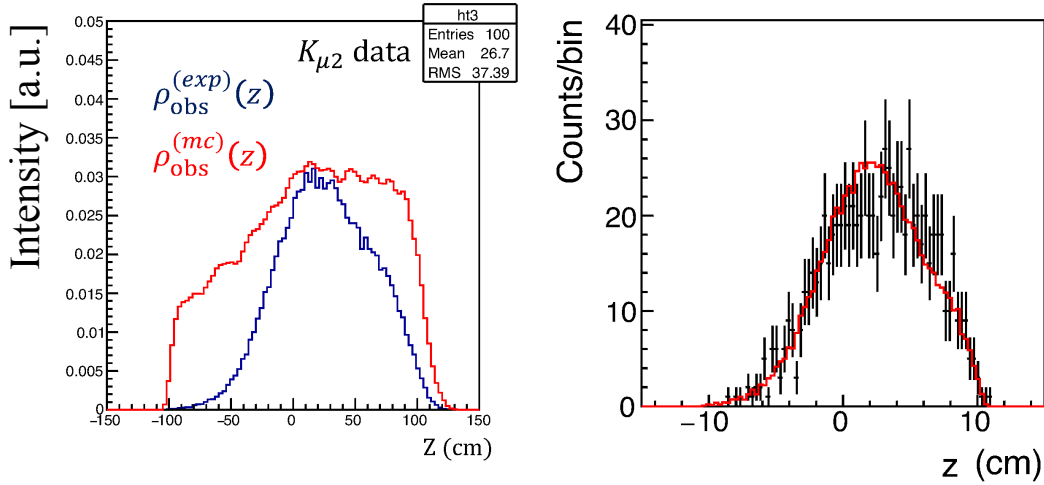
Figure 33: (Left) The observed K^+ stopping distribution using the $K_{\mu2}$ events for (blue) the experimental data and (red) the simulation. Ratio of these distributions were used as the original K^+ distribution in the simulation. (Right) the distribution of z-vertex using the $K_{\pi2}$ events for the experimental data (black dot) and the simulation calculation (red).

4.5 Particle Identification (PID) performance

The e^+ discrimination from other particles is one of the most essential issues in the E36 experiment. Also, the detection efficiency for the e^+ and μ^+ measurement should be controlled with an accuracy better than 10^{-3}. Charged particles generated in the target passed through TOF1, AC, TOF2, and PGC, and all the signals were recorded in the data. Details of the TOF analysis such as timing calibration, time-walk correction, etc. were reported in Technical note 2. For the AC and PGC analysis, fine tuning of the selection gates for ADC and TDC values is very important. It should be noted that we did not use likelihood quantities for PID in this $K_{e2\gamma}^{\mathrm{SD}}$ studies.

4.5.1 Aerogel Cherenkov (AC) Counter

The AC performance for the e/μ identification was estimated using the e^+ and μ^+ samples from the K_{e3} and $K_{\mu2}$ decays, respectively using a so-called sandwich method. The K_{e3} channel is one of major K^+ decay modes and the statistical uncertainty of the e^+ efficiency determination can be reduced. Also, $K_{\mu2}$ backgrounds in the e^+ sample can be efficiently removed by imposing the π^0 detection by CsI(Tl). Here, the K_{e3} and $K_{\mu2}$ events were selected with the tight cut conditions of TOF and PGC, as shown in Table 10.

Since the AC counters were placed close to the K^+ beam and their single counting rates were rather high, in order to reduce effects of accidental beam backgrounds, it is very important to select the AC module which charged particles passed using the tracking information. From the reconstructed particle trajectory, the particle hit positions at the inner and outer radius of the AC detector were determined, which are denoted as $x_{AC}^{(in)}$ and $x_{AC}^{(out)}$, respectively. From the x_{AC} and y_{AC} configuration, the AC address at the inner and outer radius position can be assigned ($G_{AC}^{(in)}$ and $G_{AC}^{(out)}$). The AC

Table 10: The K_{e3} and $K_{\mu2}$ selection conditions to determine the AC performance. A sandwich method was adopted here, and the events were selected using only the TOF and PGC analysis.

	$K^+ \to e^+\pi^0\nu_e$ (K_{e3})	$K^+ \to \mu^+\nu_\mu$ $(K_{\mu2})$
M_{TOF} (MeV^2/c^4)	< 0	none
p_e(MeV/c)	< 220	$(220, 240)$
A_{PGC}	> 200	< 100
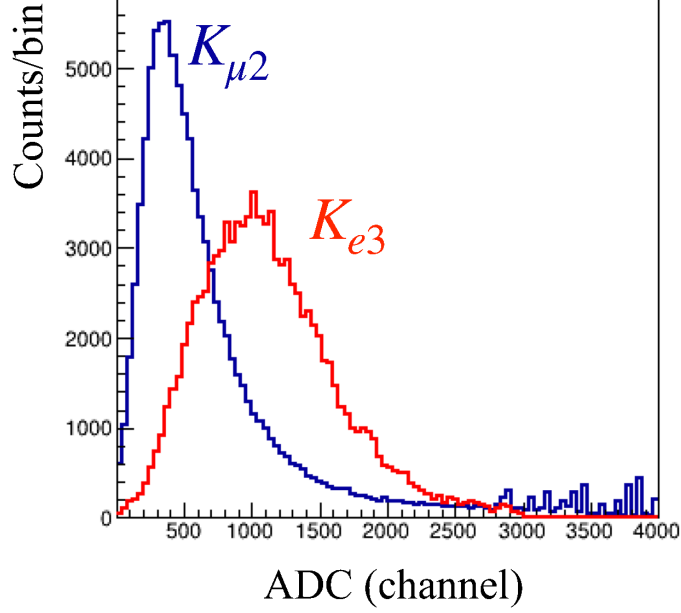
Figure 34: The AC ADC spectra for (red) positron and (blue) muon, which were obtained by selecting the K_{e3} and $K_{\mu2}$ decays. The cut point was determined to minimize the systematic uncertainty of the $K_{\mu2}$ background subtraction.

counter has two PMTs (upstream and downstream PMTs, called U/D), and the AC ADC values from the U and D PMTs were obtained which are denoted as A_{AC}^U and A_{AC}^D, respectively, as shown in Fig. 35.

Then, the AC performance was optimized using the above parameters as follows. The AC ADC value was set to zero if there was no proper timing data. The main selection criteria is $Gap^{in} = Gap^{our}$ or $Gap^{in} \neq Gap^{our}$, and then depending on the particle hit position z_{AC} along the beam direction, the most sensitive PMT signals were chosen. By this analysis method, noise signals due to beam backgrounds were effectively reduced.

4.5.2 PGC Counter

In the PGC analysis, the K_{e3} and $K_{\mu2}$ decays were used for the performance check of the e/μ separation. As discussed in the AC performed check, a sandwich method was again employed, and these events were selected by the TOF and AC analysis without using PGC. These selection criteria
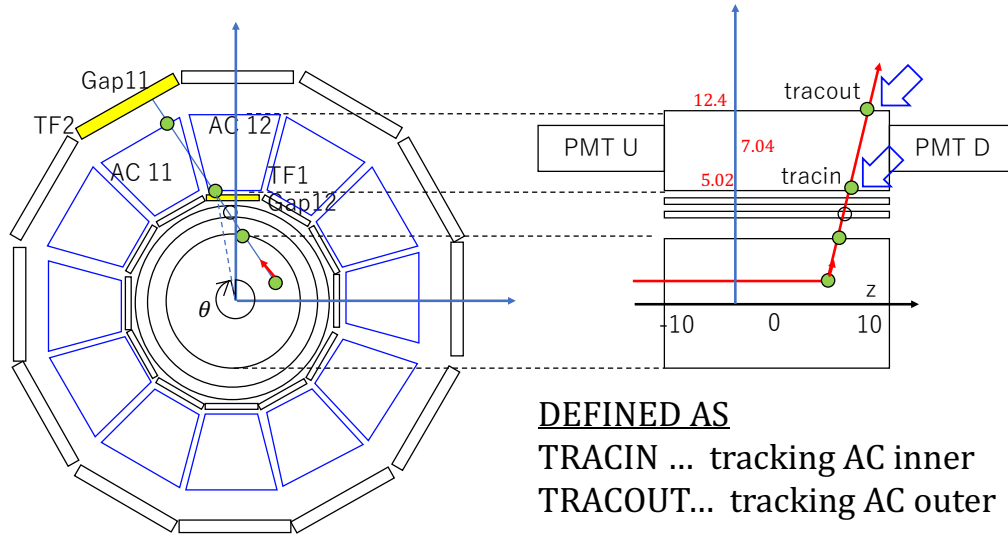
Figure 35: Typical hit pattern of charged particle on the AC counters. The AC analysis was optimized by switching the selection condition referring the tracking information.

are summarized in Table 11.

Table 11: The K_{e3} and $K_{\mu2}$ selection conditions to determine the PGC performance. A sandwich method was adopted here, and the events were selected using only the TOF and AC analysis.

	$K^+ \to e^+\pi^0\nu_e$ (K_{e3})	$K^+ \to \mu^+\nu_\mu$ ($K_{\mu2}$)
M_{TOF} (MeV^2/c^4)	< 0	none
e^+ momentum (MeV/c)	$p_e < 220$	$220 < p_e < 240$
A_{AC}	> 600	< 10

The pulse height of the output signals depends on the particle hit position on PGC. Events with short distance of the hit position from the PMTs have very high pulse height due to steep increase of the photon collection efficiency. Here, the particle hit position can be determined by extending the reconstructed trajectory to PGC, and the ADC cut points A_{PGC} were carefully studied to optimize the particle separation, as follows. We checked the efficiency by changing A_{PGC} in the 4 regions where the distance of particle hit position from PMT (d_{PGC}) is 0-10 cm, 10-20 cm, 20-30 cm, and 30-40 cm. Fig. 36 (top) shows the K_{e3} and $K_{\mu2}$ ADC spectra in these regions. The e^+ efficiency (red) and the μ^+ mis-identification probability (black) were obtained using the above K_{e3} and $K_{\mu2}$ events as a function of A_{PGC} in each region, as shown in Fig. 36 (bottom). Setting A_{PGC}=105 (blue line in Fig. 36 for the events with $d_{\mathrm{PGC}} = 0$-10 cm, the e^+ efficiency (red) and the μ^+ (black) rejection efficiency were estimated to be 90% and 70%, respectively, where these blue lines correspond to 90% of the e^+ (red) survived efficiency in the 4 regions. In the Monte Carlo simulation, the e^+ efficiency of the PGC analysis was taken into account. We have checked stability or shifts of the $Br(K^{\mathrm{SD}}_{e2\gamma})$ values by the PGC cut points.
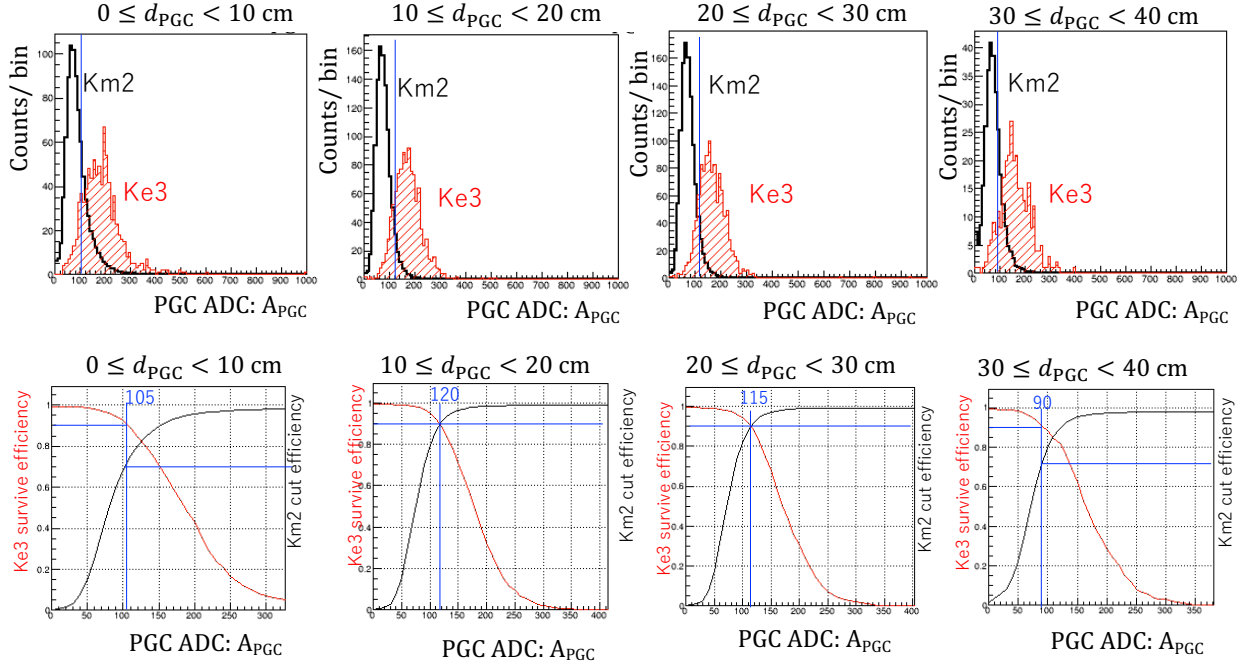
Figure 36: ADC spectra of the K_{e3} (red) and $K_{\mu2}$ (black) events for d_{PGC} = 0-10 cm, 10-20 cm, 20-30 cm, and 30-40 cm (top). The e^+ efficiency (red) and the μ^+ mis-identification probability (black) were obtained using these K_{e3} and $K_{\mu2}$ events as a function of A_{PGC} in each region (bottom).

However, the PGC detector was operated as a calorimeter and the pulse height depends on particle energies. Therefore, we have to evaluate the detector performance using e^+ particles in the $K_{e2\gamma}^{\mathrm{SD}}$ and $K_{e2(\gamma)}$ momentum region, which is higher than the K_{e3} endpoint. To solve this problem, we used in-flight K_{e3} events by selecting the prompt timing of the beam Cherenkov counter (other conditions were the same as the normal K_{e3} selection). As a result, the e^+ momentum can be raised up to 300 MeV/c which can cover the $K_{e2\gamma}^{\mathrm{SD}}$ and $K_{e2(\gamma)}$ region, which will be discussed in section 4.6.

4.5.3 Time-of-Flight (TOF) measurement

The particle hit times on TOF1 and TOF2 (t_{TOF1} and t_{TOF2}) were determined by the average time of the two PMTs at both ends in order to remove effects from the particle hit position. The Time-of-Flight (TOF) between TOF1 and TOF2 were obtained using an offset value (δt) as,

$$TOF_a = t_{TOF2} - t_{TOF1} + \delta t. \tag{34}$$

The δt can be determined using the mono-energetic charged particle of π^+ and μ^+ from the $K_{\pi2}$ and $K_{\mu2}$ decays, respectively. Actual flight time between TOF1 and TOF2 could be calculated from the

event-by-event observed information and flight path length by the track reconstruction analysis as,

$$TOF(K_{\mu 2}) = \frac{L}{c}\frac{\sqrt{p^2 + m_\mu^2}}{p}, \quad TOF(K_{\pi 2}) = \frac{L}{c}\frac{\sqrt{p^2 + m_\pi^2}}{p} \tag{35}$$

where L is the flight path length, c is the light speed, and p is the charged particle momentum in the spectrometer. The δt value was obtained by adjusting the peak position of the $\Delta(K_{\mu 2} = TOF_a - TOF(K_{\mu 2})$ distribution to be zero using the B=0.65 T data, as shown in Fig. 37. In this figure, the *delta* correction is already applied and the peak position is located at 0 ns. A time-walk correction for leading edge discriminators were also applied for both TOF and TOF2, however the effect is not significant to improve the TOF timing resolution.
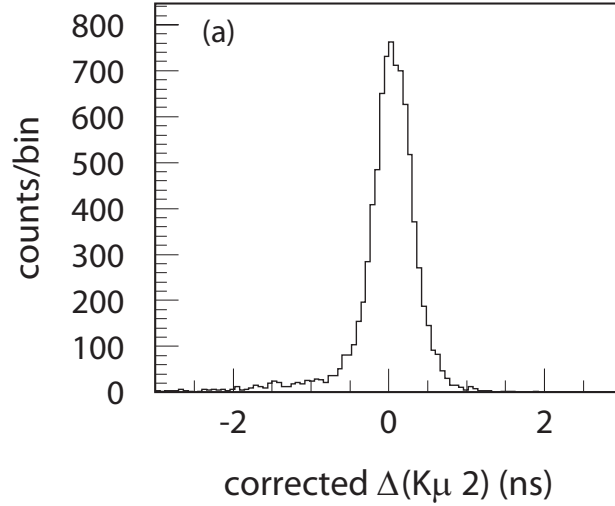
Figure 37: The $\Delta(K_{\mu 2})$ distribution after applied the δ correction, and the peak position is located at 0 ns. The TOF quantity is correctly converted from the TDC values of TOF1 and TOF2. The *delta* offset was also determined using $\Delta(K_{\mu 2})$

Then, β and mass squared (M_{TOF}^2) was obtained as,

$$\beta = \frac{L}{TOF \cdot c} \tag{36}$$

$$M_{\text{TOF}}^2 = p^2(1/\beta^2 - 1). \tag{37}$$

In the TOF analysis, the K_{e3} and $K_{\mu 2}$ decays were also used for the performance check of the M_{TOF}^2 selection and some other calibrations before the $K_{e2(\gamma)}$ and $K_{e2\gamma}^{\text{SD}}$ analysis. The sandwich method discussed above was adopted again here, These events were selected by the TOF and PGC cuts, and these selection criteria are summarized in Table 12. The e^+ efficiency and μ^+ mis-identification curves are shown in Fig 43 (right).

4.6   Dependence of PID performance on e^+ momentum

In this analysis, it is very important to study the e^+ efficiency difference between the $K_{e2\gamma}^{\text{SD}}$ and $K_{e2(\gamma)}$ decays. However, the K_{e3} endpoint momentum is 228 MeV/c, and the control e^+ sample higher than

Table 12: The K_{e3} and $K_{\mu2}$ selection conditions to determine the TOF performance. A sandwich method was adopted here, and the events were selected using only the AC and PGC analysis.

	$K^+ \to e^+\pi^0\nu_e$ (K_{e3})	$K^+ \to \mu^+\nu_\mu$ ($K_{\mu2}$)
e^+ momentum (MeV/c)	$p_e < 220$	$220 < p_e < 240$
A_{PGC}	> 175	< 100
A_{AC}	> 600	< 10
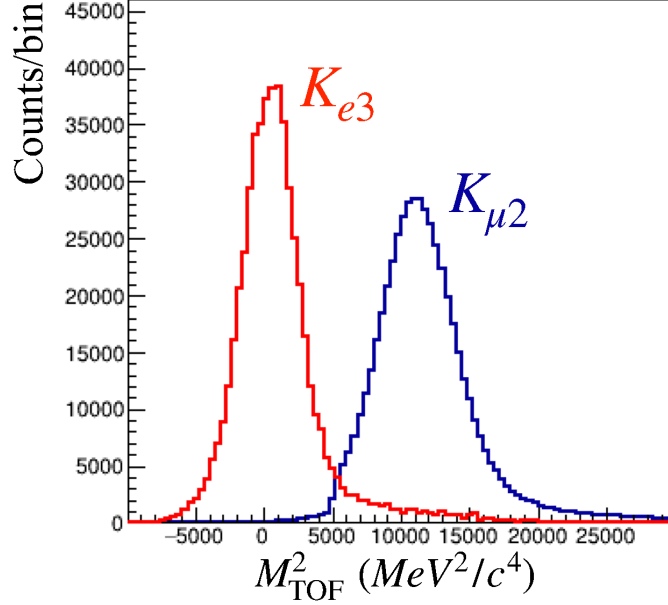
Figure 38: The M^2_{TOF} spectra for (red) positron and (blue) muon, which were obtained by selecting the K_{e3} and $K_{\mu2}$ decays. The cut point was determined to minimize the systematic uncertainty of the $K_{\mu2}$ background subtraction.

the K_{e3} endpoint momentum was not easily prepared. To solve this problem, we decided to use the in-flight K_{e3} decay whose e^+ momentum was boosted in the region higher than the K_{e3} endpoint. Using e^+ samples in the region of ~ 250 MeV, we checked the particle identification efficiency for the AC, PGC, and TOF detectors. Then, the simulation spectrum was corrected for the decided efficiency to compare all data taken in the E36 experiment.

4.6.1 AC efficiency

In order to check the AC efficiency, the in-flight-K_{e3} events were selected by the following conditions is follows:

$$\text{PGC ADC} > 200 \tag{38}$$
$$-10 < \text{PGC TDC} < 2 \tag{39}$$
$$\text{TOF mass} < 2,000 \text{ MeV}^2/\text{c}^4 \tag{40}$$

$$N_{\text{Cluster}} = 2 \tag{41}$$
$$-0.5 < t_{\text{kstop}} < 0.5 \text{ ns} \tag{42}$$
$$-0.5 < \cos\theta_{\gamma\gamma} < 0.5 \tag{43}$$

In addition, the in-flight K_{e3} events were obtained by imposing the prompt timing of incoming K^+s measured the beam Cherenkov counter as $-0.5 < t_{kstop} < 0.5$. The K_{e3} events were further purified by restricting the $\pi^0 \to \gamma\gamma$ kinematics to be $-0.5 < \cos\theta_{\gamma\gamma} < 0.5$.

The AC detection efficiency dependence on the e^+ momentum was obtained by varying the AC cut point (A_{AC}), as shown in Fig. 39. As a result, we recognized that the AC efficiency has negligible momentum dependence by a linear fitting for the e^+ events in the regions of 200-220 and 240-270 MeV/c, as shown in Fig. 39. These fitted slopes and offsets with the associated error size are listed in Table 13. The event with $p > 270$ MeV/c has low statistics, so we did not adopt over 270 MeV/c region to fit. It should be noted that other PID momentum dependence estimate is used same fitting region. The AC efficiency distribution was taken into account in the analysis. The fitting error is used to estimate the systematic uncertainty for PID efficiency.

Figure 39: Momentum dependence of AC efficiency. In the regions of $200-230$, $230-240$, and $240-300$ MeV/c, the stopped K_{e3} sample was dominated, $K_{\mu2}$ sample could be contaminated, and the in-flight K_{e3} sample was dominated, respectively.

4.6.2 PGC efficiency

Similar with the AC efficiency study in higher e^+ momentum region above the K_{e3} endpoint. The PGC efficiency was also checked using the in-flight K_{e3} decays, which were selected using the following

Table 13: Momentum dependence of the AC efficiency

A_{AC} cut point	slope	offset
100	$(-4.51 \pm 4.16) \times 10^{-4}$	1.04 ± 0.090
200	$(-5.44 \pm 4.51) \times 10^{-4}$	1.04 ± 0.097
300	$(-4.24 \pm 4.71) \times 10^{-4}$	0.98 ± 0.102
400	$(-8.53 \pm 5.51) \times 10^{-4}$	1.04 ± 0.119
500	$(-4.54 \pm 5.95) \times 10^{-4}$	0.91 ± 0.129
600	$(-3.02 \pm 6.40) \times 10^{-4}$	0.83 ± 0.139
700	$(1.49 \pm 6.74) \times 10^{-4}$	0.68 ± 0.146
800	$(3.35 \pm 7.07) \times 10^{-4}$	0.59 ± 0.153
900	$(-2.50 \pm 7.56) \times 10^{-4}$	0.64 ± 0.164

selection conditions:

$$\text{AC ADC} > 500 \tag{44}$$

$$-15 < \text{AC TDC} < 15 \tag{45}$$

$$\text{TOF mass} < 2,000 \text{ MeV}^2/\text{c}^4 \tag{46}$$

$$\text{N}_{\text{Cluster}} = 2 \tag{47}$$

$$-0.5 < \text{t}_{\text{kstop}} < 0.5 \text{ ns} \tag{48}$$

$$-0.5 < \cos\theta_{\gamma\gamma} < 0.5 \tag{49}$$

The PGC detection efficiency dependence on the e^+ momentum was obtained by several PGC cut points of 150–250, as shown in Fig. 40. In the region of $230-240$ MeV/c, the $K_{\mu2}$ background contribution was more serious comparing with the AC efficiency analysis, because the μ^+ rejection power of AC is inferior to that of PGC. Therefore, we could not obtain the reliable result for the efficiency estimation. In the region of $240-300$ MeV/c, the in-flight K_{e3} events were considered to be dominated.

The PGC detection efficiency dependence on the e^+ momentum was obtained by varying the PGC cut point (A_{PGC}), as shown in Fig. 40. Since the PGC output signal is nearl proportional to the e^+ energy, the momentum dependence of the PGC efficiency must be inevitable. The slope parameters obtained by using a linear function for the events in the regions of $200-220$ and $240-270$ MeV/c are shown in Fig. 40. There results are also listed in Table 14. The fitting error is used to estimate the systematic uncertainty for the PID efficiency.

4.6.3   TOF mass efficiency

Similar with the AC and PGC efficiency study in higher e^+ momentum region above the K_{e3} endpoint. The TOF mass efficiency was also checked using the in-flight K_{e3} decays, which were selected using the following selection conditions:
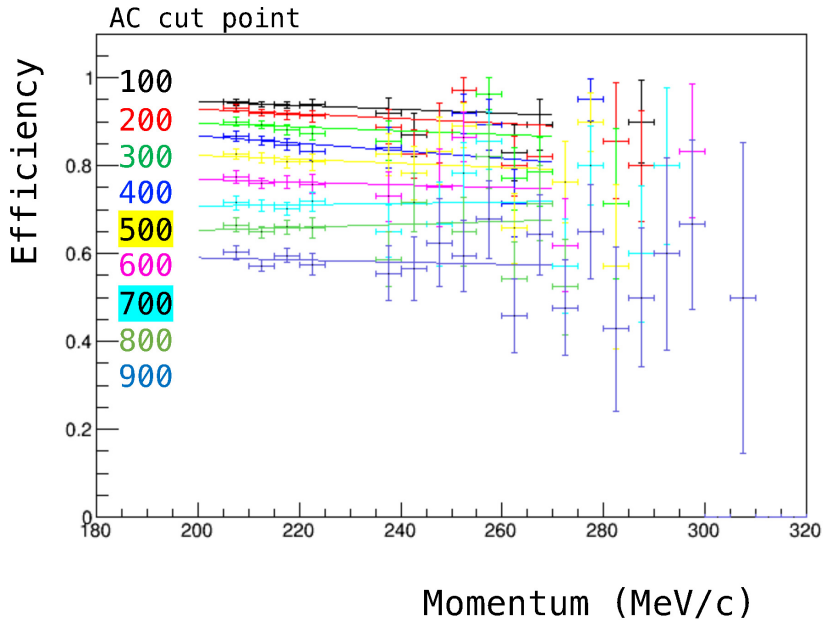
$$\text{AC ADC} > 500 \tag{50}$$

Figure 40: Momentum dependence of the PGC efficiency. In the region $200-230$, $230-240$, and $240-300$ MeV/c, the stopped K_{e3} sample is dominated, $K_{\mu2}$ sample can be contaminated (masked), and the inflight K_{e3} sample is dominated, respectively.

$$-15 < \text{AC TDC} < 15 \text{ ns} \tag{51}$$
$$\text{PGC ADC} > 200 \tag{52}$$
$$-2 < \text{AC TDC} < 10 \text{ ns} \tag{53}$$
$$\text{N}_{\text{Cluster}} = 2 \tag{54}$$
$$-0.5 < \text{t}_{\text{kstop}} < 0.5 \text{ ns} \tag{55}$$
$$-0.5 < \cos\theta_{\gamma\gamma} < 0.5 \tag{56}$$

Here we just repeated the same analysis as the AC and PGC efficiency studies. The e^+ momentum dependence of the e^+ efficiency by the TOF analysis was obtained for several M_{TOF}^2 cut points, as shown in Fig. 41. These fitted slopes and offsets are listed to Table 15.

4.6.4 Combination of the three PID system

Figure 42 shows the e^+ efficiency (solid/red) and the μ^+ rejection probability (dotted/black) at the momentum of 247 MeV/c and 236 MeV/c, respectively, as functions of the (a) AC, (b) PGC, and (c) M_{TOF}^2 cut points. The e^+ efficiency for each PID system was obtained by pre-selecting e^+ from the $K^+ \rightarrow \pi^0 e^+ \nu$ (K_{e3}) and in-flight K_{e3} decays for the momentum region higher than the K_{e3} endpoint momentum (228 MeV/c) by tightening PID conditions for the other two PID systems. The μ^+ rejection probability was determined using μ^+s from the $K_{\mu2}$ decays. As a result, these position selection cuts were chosen to remove most of the $K_{\mu2}$ backgrounds with a μ^+ rejection probability of $(99.934\pm0.002)\%$, while maintaining a reasonable e^+ efficiency of $(75.2\pm0.4)\%$. This was determined

Table 14: Momentum dependence of PGC efficiency

A_{PGC} cut point	slope	offset
150	$(0.47 \pm 0.51) \times 10^{-3}$	0.69 ± 0.11
160	$(1.37 \pm 0.53) \times 10^{-3}$	0.44 ± 0.11
170	$(2.13 \pm 0.56) \times 10^{-3}$	0.21 ± 0.12
180	$(3.29 \pm 0.59) \times 10^{-3}$	-0.11 ± 0.13
190	$(4.04 \pm 0.62) \times 10^{-3}$	-0.34 ± 0.14
200	$(4.78 \pm 0.64) \times 10^{-3}$	-0.57 ± 0.14
210	$(4.86 \pm 0.68) \times 10^{-3}$	-0.66 ± 0.15
220	$(4.65 \pm 0.67) \times 10^{-3}$	-0.68 ± 0.15
230	$(4.31 \pm 0.67) \times 10^{-3}$	-0.66 ± 0.14
240	$(4.16 \pm 0.65) \times 10^{-3}$	-0.68 ± 0.14
250	$(4.05 \pm 0.64) \times 10^{-3}$	-0.70 ± 0.14

Table 15: Momentum dependence of TOF mass efficiency

M_{TOF}^2 cut point	slope	offset
8000	$(-0.79 \pm 0.32) \times 10^{-3}$	1.14 ± 0.07
7000	$(-1.13 \pm 0.39) \times 10^{-3}$	1.21 ± 0.08
6000	$(-1.11 \pm 0.38) \times 10^{-3}$	1.19 ± 0.08
5000	$(-2.09 \pm 0.49) \times 10^{-3}$	1.38 ± 0.11
4000	$(-2.78 \pm 0.58) \times 10^{-3}$	1.49 ± 0.13
3000	$(-3.57 \pm 0.65) \times 10^{-3}$	1.60 ± 0.14
2000	$(-3.65 \pm 0.70) \times 10^{-3}$	1.52 ± 0.15
1000	$(-3.00 \pm 0.76) \times 10^{-3}$	1.25 ± 0.17
0	$(-1.23 \pm 0.73) \times 10^{-3}$	0.72 ± 0.16

to minimize the total uncertainty in the $K_{e2\gamma}^{\mathrm{SD}}$ branching ratio measurement from the $K_{\mu2}$ subtraction (see section 6.2). Fig. 43 shows the demonstration of the PID performance and it can be seen that the muon backgrounds are rejected by the PID detectors.

4.7 Photon analysis using CsI(Tl) calorimeter

Before starting the photon analysis, the number of the hit TOF1 counters was required to be one which was matched to the hit TOF2 address to confirm charged particles transmit TOF1 and the spectrometer, and reach TOF2. Therefore, events with charged particle entering into the CsI(Tl) were basically rejected. Therefore, it is enough to consider positive and negative pair such as π^+/π^- and e^+/e^- for charged particle entrance into CsI(Tl). However, the spectrometer field was adjusted to accept the $K_{e2(\gamma)}$ decay efficiently, and the above three body decays were also removed.
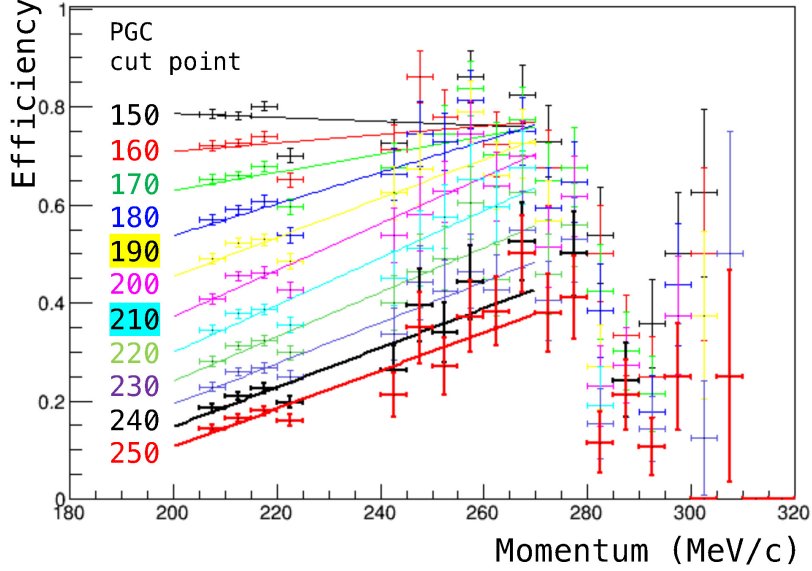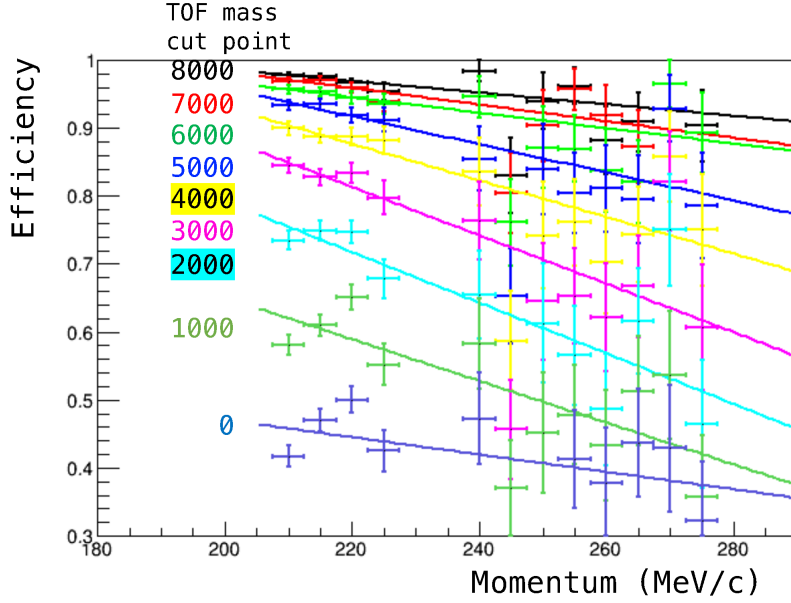
Figure 41: Momentum dependence of TOF mass efficiency. In the region $200-230$, $230-240$, and $240-300$ MeV/c, the stopped K_{e3} sample is dominated, $K_{\mu 2}$ sample can be contaminated (masked), and the inflight K_{e3} sample is dominated, respectively.
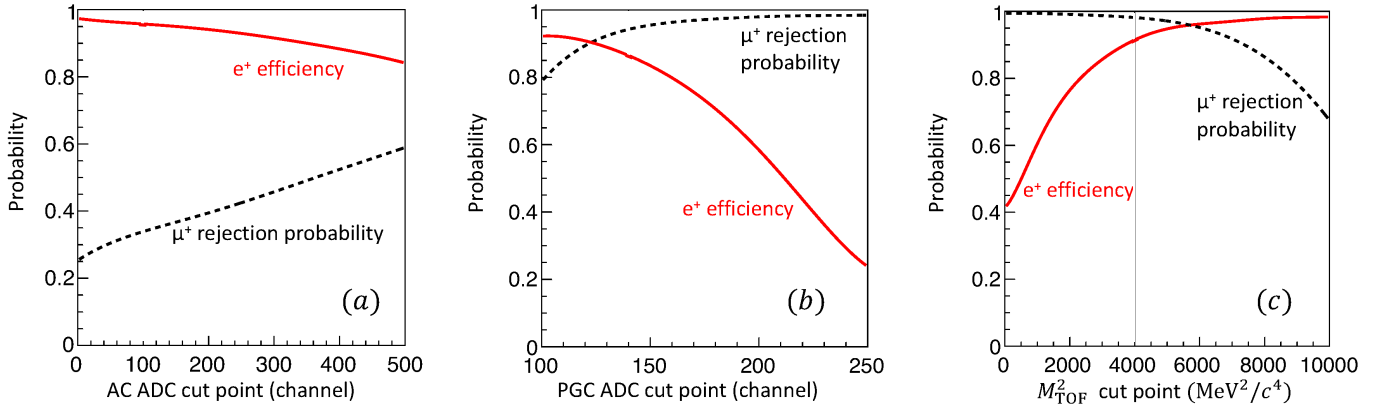
Figure 42: The e^+ detection efficiency (solid/red lines) and μ^+ rejection probability (dashed/black lines) for $p_{e^+} = 247$ MeV/c and $p_{\mu^+} = 236$ MeV/c, as functions of the (a) AC, (b) PGC, and (c) M^2_{TOF} cut points. The cut points adopted for each detector are also shown. As for possible momentum dependence, see the text.
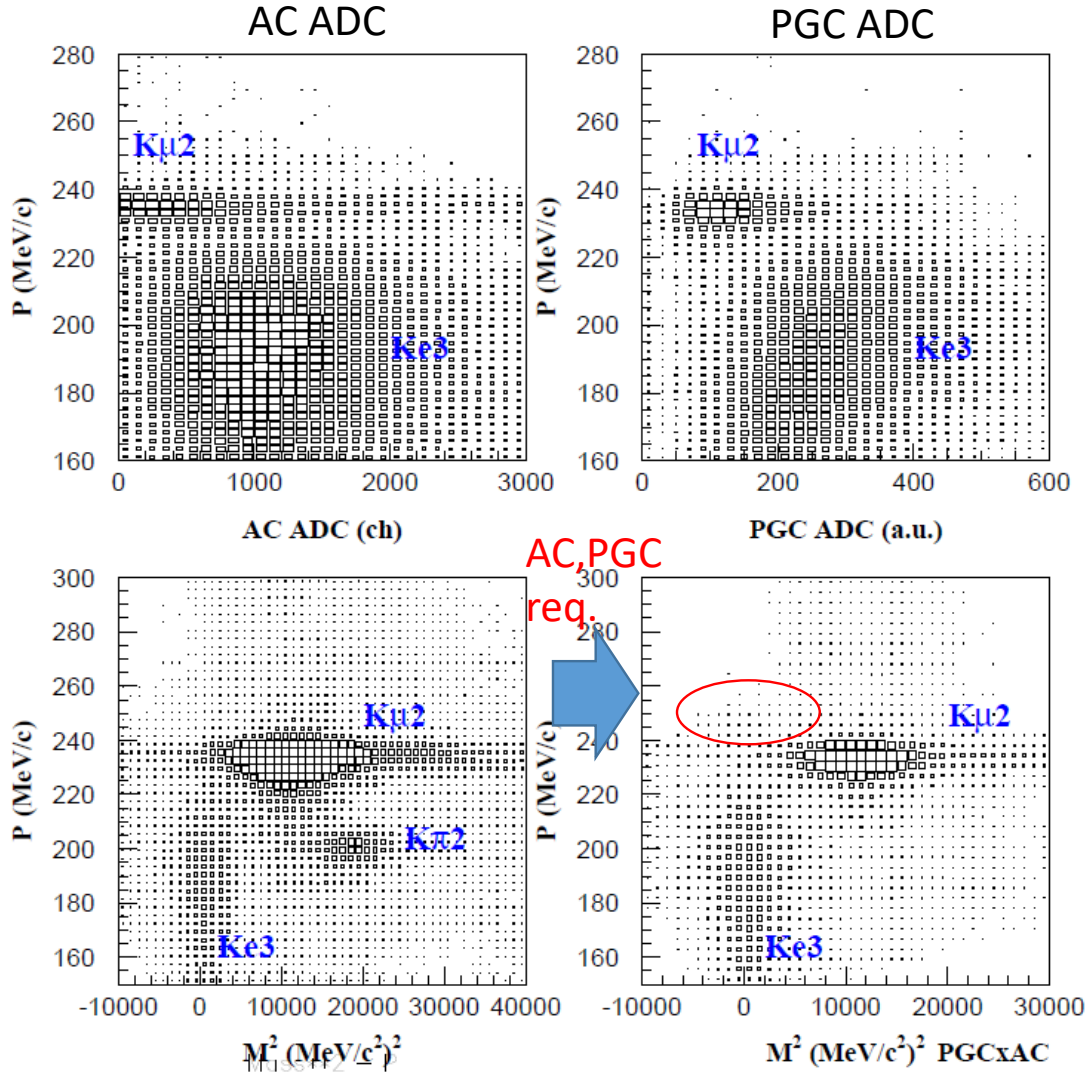
Figure 43: Top is correlation plots of (p, A_{AC}) and (p, A_{PGC}). Bottom is (p, M^2_{TOF}) correction before and after the AC and PGC cuts. The $K_{\mu 2}$ and $K_{\pi 2}$ backgrounds were efficiently removed by the PID analysis. The red ellipse corresponds to the accessible $K_{e2(\gamma)}$ and $K^{\mathrm{SD}}_{e2\gamma}$ region in the E36 experiment.

4.7.1 Waveform analysis

To read out the CsI(Tl) calorimeter, VF48 Flash ADCs [55] with a sampling frequency of 25 MHz were employed to record the waveform data in order to resolve pulse-pileup events with high efficiency. In the waveform analysis, the waveform peak position in the time region of 60-65 TDC channel which corresponds to the K^+ decay timing was once searched for. Even if the fake peak during the above trigger timing due to background pileup effect was accepted, these events could be removed by the subsequent fitting process. On the other hand, the peak was not recognized and the event was rejected by this first check, and it can be recovered by the subsequent fitting.
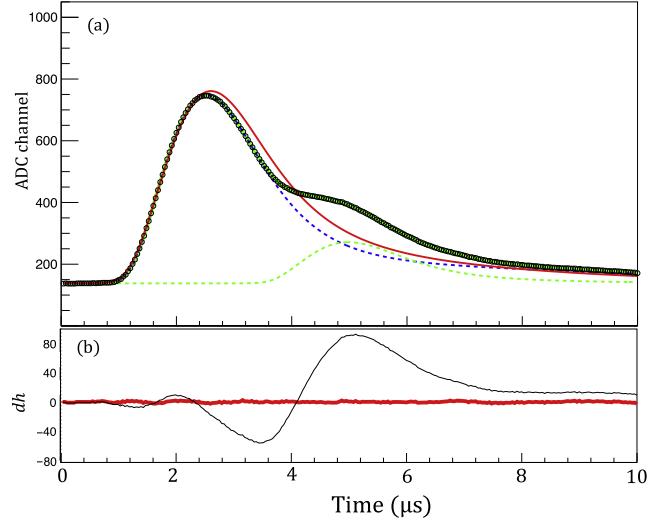
Figure 44: (a) is typical pileup waveform of the CsI(Tl) calorimeter signal. The open circles are the data points. The red line is the result adopting the single-fitting function which cannot reproduce the experimental data. The green and blue dotted lines are the decomposed 1st and 2nd pulses, respectively, using the double-fitting function. (b) is the deviation of each data point from the fit curves. The black and red lines are the results using the single- and double- fitting function, respectively. The experimental data were correctly reproduced by the double-fitting function.

Next, the waveform was fitted by the H-Ito model [60] with an assumption of a single pulse, as shown in Fig. 44, the model function is adopted as,

$$f(t) \;\; = \;\; \frac{A}{1 - \exp\{-(t - \tau_0)/\lambda\}} \times Freq\left(\frac{t - \tau_0 - d}{\mu}\right) \tag{57}$$

$$\times \left\{\frac{t - \tau_0}{\tau_1} \exp\left(1 - \frac{t - \tau_0}{\tau_1}\right) + \frac{t - \tau_0}{\tau_2} \exp\left(1 - \frac{t - \tau_0}{\tau_2}\right)\right\}, \tag{58}$$

where A is amplitude of the pulse and τ_0 is the rise time for the timing determination. The λ, μ, and τ_1, τ_2 parameters are time constants to express the rise and decay parts of the pulse, respectively. $d \sim 1$ μs is introduced for a timing adjustment and $\varepsilon \sim 0.06$ is the ratio of the two decay components.

$Freq(x)$ is known as the frequency function given as

$$Freq(x) = \int_{\infty}^{x} \exp(-t^2/2)dt \tag{59}$$

For the analysis of pileup events, the maximum dh value (dh_{max}) was first determined in the entire region using a single-pulse fitting, where dh is defined as a difference of ADC of data and fitting. The waveforms with $|dh_{max}| > 10$ can be recognized as two or more pulse components. These events were treated as pileup events, and multiple pulses in the fitting were taken into account. We can accept events as a double-pulse waveform with the conditions of (i) a waveform with $|dh_{max}| < 10$ and (ii) the time interval between the 1st and the 2nd signals is greater than 200 ns. The rejected events are treated as events with further multiple signals. The double fitting function was introduced by simply extending the signal pulse method as,

$$F(t) = \sum_{j=1}^{2} f(t; A^{(j)}, \tau_0^{(j)}) \tag{60}$$

The γ events were conducted with the above wave-id for the single and double pulses. The signal with triple pulses and more pulses were rejected by the current analysis. Also, pulses with overflowed amplitudes were not accepted.

Since the VF48 FADC was operated by a 40 MHz external clock, the reference signal originating from the trigger pulse was recorded to correct for random jitter of the clock timing t_{ref}. The timing is determine to $\tau_0 - t_{fer}$, where t_{ref} is a reference time. The pulse height is converted to the energy with the convert coefficient of $k = 2.1 - 2.5 MeV^{-1}$. After the waveform analysis, a photon cluster was constructed from crystals which had a energy deposit larger than the energy cut point and a proper timing. Once these crystals were searched by scanning all the CsI(Tl) modules, and a photon cluster was formed by grouping adjacent hit crystals. The photon energy and hit position were obtained by summing the energy the Cs(Tl) cluster modules and by determining the energy-weighted centroid of the cluster modules, respectively.

4.7.2 CsI(Tl) calorimeter performance

The energy calibration of the CsI(Tl) calorimeter was performed using μ^+s from the $K_{\mu 2}$ decays, and relative gain coefficient for each module was obtained. The signal waveform model for a double-pulse fitting was developed by the muon signal and the subsequent e^+ signal from the muon decay, and the energy and timing resolutions were obtained to be 2.63% (σ) and 10.7 ± 0.1 ns (σ) for the muon kinetic energy of 153 MeV, respectively [60]. Fig. 45 shows the μ^+ energy spectrum from the $K_{\mu 2}$ decay obtained taking into account the energy loss in the target. The red and blue spectra indicate the calibrated energy spectrum with and without the target energy loss correction, respectively.

Then, using π^0 events from the $K^+ \rightarrow \pi^+ \pi^0$ ($K_{\pi 2}$) decays, the experimental spectra were compared with the Monte Carlo simulation, and the consistency check was carefully performed, as shown in Fig. 46. Here the above relative coefficient was re-adjusted by introducing global(common) gain coefficient ($G_{gl} = 0.93$) to reproduce the $M_{\gamma\gamma}$ spectrum of the π^0 decay. In this analysis, accidental backgrounds mentioned below were not taken into account, and instead we required the selection conditions of $\cos\theta_{\pi\pi} < 0.99$ to remove accidental backgrounds. In the figure, π^+ momentum (p_{π^+}), γ
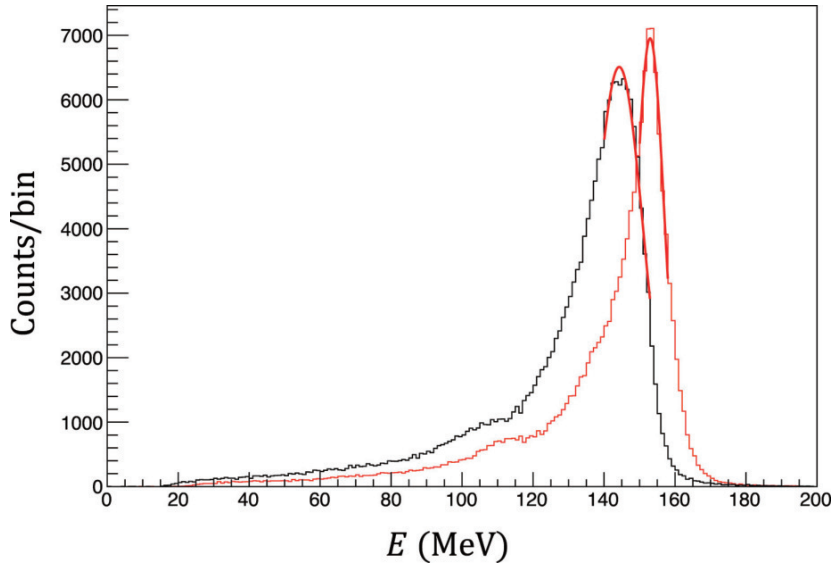
Figure 45: The calibrated energy spectra obtained using the $K^+ \to \mu^+\nu$ decays. The red spectrum includes a correction for the energy loss in the target.

energy (E_γ), opening angle between 2γ $(\cos\theta_{\gamma\gamma})$, and invariant mass of π^0 (IM), and some additional spectra are shown. It should be noted that IM is smaller than the nominal π^0 rest mass because of the γ shower leakage from the CsI(Tl) crystal and the hardware threshold energy in each CsI(Tl) module. These effects were taken into account in the simulation calculation, which can correctly reproduce the experimental data, as shown in Fig. 46.

4.7.3 Photon energy threshold

The VF48 hardware threshold corresponding to approximately 17.5 MeV was set in the experiment, however this threshold was not constant due to finite gain distribution and DC level difference of each CsI(Tl) module. Therefore, we have to set a new common threshold a little above the hardware threshold to remove efficiency difference from the threshold uncertainty.

After the energy calibration, we carefully checked a rising structure of the photon energy spectrum around the threshold energy region. We selected the K_{e3} sample which were fully reconstructed events with $K^+ \to e^+\pi^0\nu$ and $\pi^0 \to \gamma\gamma$ by the conditions of:

$$\text{AC ADC} > 500 \tag{61}$$
$$\text{PGC ADC} > 500 \tag{62}$$
$$\text{TOF mass} < 2000 \tag{63}$$
$$\text{N}_\gamma = 2 \tag{64}$$
$$-0.5 < \cos\theta_{\gamma\gamma} < 0.5 \tag{65}$$

The invariant π^0 mass of ~ 100 MeV/c^2 was successfully observed using the K_{e3} events. Details of the π^0 reconstruction using the $K_{\pi2}$ decays were already discussed in section 4.7.2, and the results

64
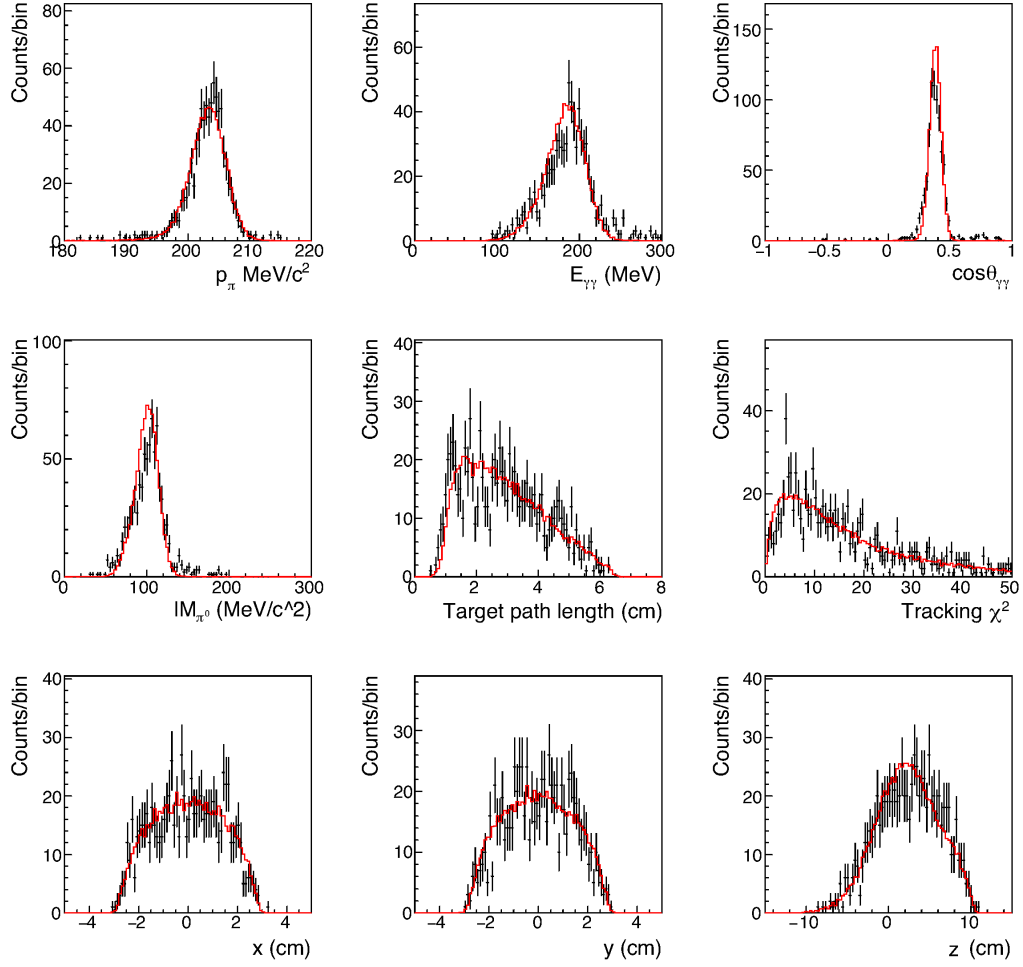
Figure 46: The $K^+ \to \pi^+\pi^0$ spectra with the selection conditions of $\cos\theta_{\pi\pi} < -0.99$. The accidental backgrounds for the simulation events mentioned in section 5.5 were not taken into account. The p_π, $E_{\gamma\gamma}$, $\cos\theta_{\gamma\gamma}$, and M_{π^0} distributions are shown. Black(dot) and red(line) histograms are the experimental data and the simulation, respectively. In addition, the distributions of flight-path length in the target, tracking χ^2, and kaon stop position are shown.
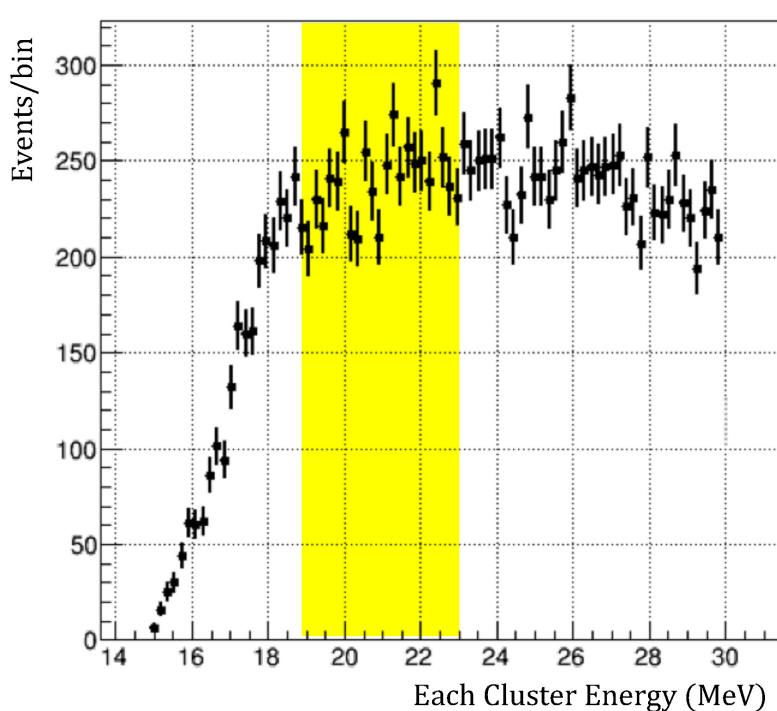
Figure 47: The CsI(Tl) cluster energy distribution around the threshold region using the K_{e3} sample, which is focused to E<30 MeV.The plateau component of $19-23$ MeV just above the raising part is seen. The energy threshold of 21 MeV was adopted for the photon detection.

were shown in Fig. 46. The cluster energy distribution of the selected K_{e3} events around threshold region is shown in Fig. 47. The center of the rising region is 17 MeV which corresponds to the VF48 hardware threshold. Yellow hatched area in the $19-23$ MeV region is the plateau component above the threshold region. Here we decided that the new energy threshold is 21 MeV for the photon detection.

4.8 Photon analysis using GSC

The GSC data based on a standard ADC and TDC measurement were taken in the E36 experiment, as shown in Fig. 48. The discriminator threshold was set for the particular level of the phototube output. Low and high channel regions in the ADC spectrum were rejected by the leading-edge discriminator and ADC saturation effect, respectively. It should be emphasized that information of the photon energy and hit position are used in the CsI(Tl) analysis by imposing the $K_{e2\gamma}^{\rm SD}$ kinematics in the event selection. On the other hand, although the GSC counters could not provide the energy and hit position of the radiative photons, the e^+ momentum spectra of the $K_{e2\gamma}^{\rm SD}$ decays were successfully obtained by requiring only the GSC hits without imposing any kinematical constraints (see section 5). In addition, since the timing resolution of the GSC was 1 ns, as shown in Fig. 48(b), which was about 1/10 of that of CsI(Tl) and the singles GSC rate was much lower than the singles CsI(Tl)

rate, the $K_{\mu 2}$ backgrounds with an accidental hit can be efficiently removed. As a result, the PID condition for the μ^+ rejection in the GSC analysis could be relaxed and the e^+ efficiency increased.

Figure 48: The GSC (a) ADC and (b) spectra. Low and high channel regions in the ADC spectrum were rejected by the leading-edge discriminator and ADC saturation effect, respectively.

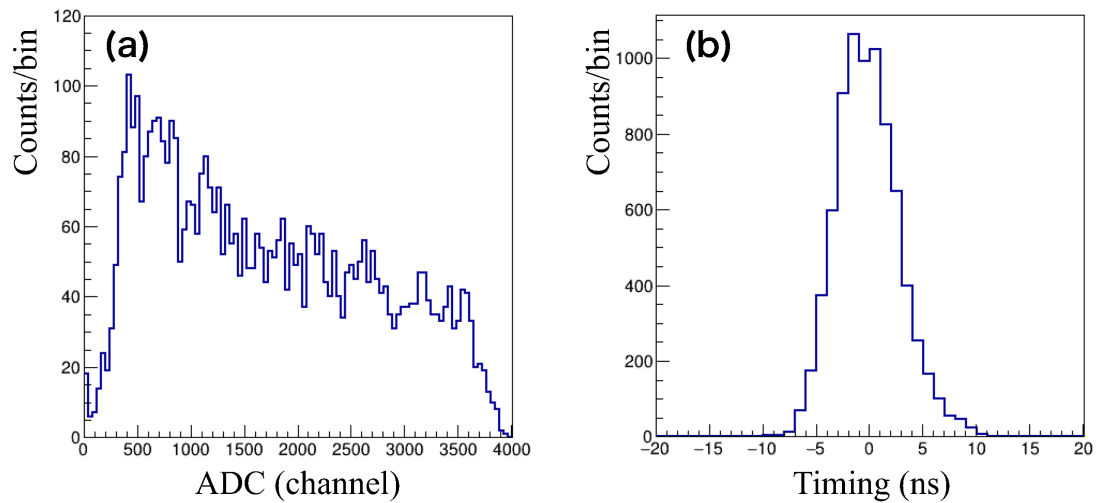# 5 Monte Carlo Simulation

5.1 General description

The interactions between basic particles and ordinary materials in the E36 detector complex was taken into account in the Monte Carlo simulation calculation based on a GEANT4 code. So far, the simulation program entitled "G4E36" using GEANT 4.10.1 has been developed. Here, the detector configuration installed in the simulation is shown in Fig. 49. It should be noted that the G4E36 start the simulation from K^+ decays at rest without taking into account the K^+ beam history and pursue all particles generated from the K^+ decay in this study. Therefore, the K^+ stopping distribution is very important input to the simulation calculation.

The experimental reproducibility of the experimental condition by the simulation calculation was carefully checked using major K^+ decay channels such as $K_{\mu 2}$, $K_{\pi 2}$, and K_{e3} events. The experimental spectra of chamber profiles, kaon stopped position, momentum distributions, γ energy, angle distributions, etc., were in good agreement with the simulation calculation. The $K_{e2\gamma}^{\text{SD}}$ events were once generated with the assumption of the form factor, λ, calculated by the ChPT model at $\mathcal{O}(e^3 p^6)$.

Then, the number of the $K_{e2\gamma}^{\text{SD}}$ events (normalization parameter) for the acceptance calculation was determined by comparing the experimental $K_{e2\gamma}^{\text{SD}}$ spectra with the simulation using a fitting method. In the present study, the λ parameter of the SD form factor was fixed to the theoretical calculation. On the other hand, an acceptance change due to the λ uncertainty was treated as the systematic uncertainty. The difference between the experimental spectra with the simulation was minimized by adjusting these parameters, and the associated parameter values were treated as the best fitting results. It should be emphasized that the common analysis codes accessed both of the experimental and simulation data in order to reduce a systematic uncertainty due to the analysis, and these results were used for the event number($N(K_{e2\gamma}^{\text{SD}})$, $N(K_{e2(\gamma)})$ and acceptance ($\Omega(K_{e2\gamma}^{\text{SD}})$, $\Omega(K_{e2(\gamma)})$) determination. The simulation data such as deposit energy, particle hit position, etc. were digitized and stored in the same format as the experimental data.

5.2 Detector components installed in the simulation codes

We have taken into account the following sensitive detector items in the Monte Carlo simulation. The detector material, size, geometry, etc. were installed as precisely as possible to reproduce the experimental conditions. The PID detectors (TOF, AC, PGC) were installed in the simulation code, however output signals from the detectors were discarded and not recorded in the data file (the e^+ efficiency was 100% in the simulation). Therefore, the PID selection conditions should be the same for the $K_{e2(\gamma)}$ and $K_{e2\gamma}^{\text{SD}}$ decays to cancel out the e^+ detection efficiency.

Active Target: An active target, which consist of 256 scintillator bars with a size of (3.1 mm × 3.1 mm) × 200 mm were arranged in a beam direction to form of 6-cm-ϕ tube. The plastic scintillator material is C_9H_{10} with density of 1.032 g/cm^3. When charged particles lose the energy in each fiber, the energy and time information were recorded every time. For the scintillating light transportation, 256 wavelength-shifter fibers (defined same material of scintillator) are set downstream of the target,
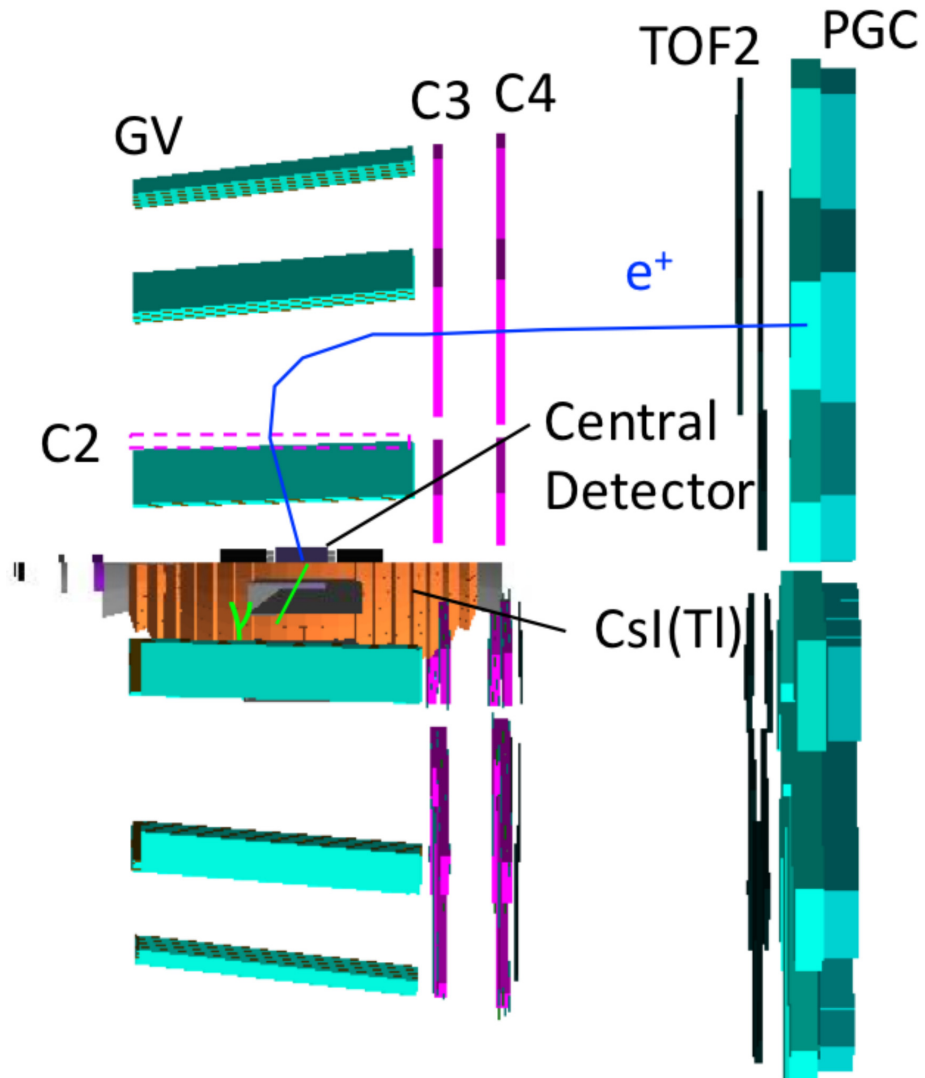
Figure 49: The detector configuration installed in the Monte Carlo simulation. Central detectors, particle trackers, PID detectors, CsI(Tl) calorimeter, GSC counter etc. were taken into account in the simulation. Common analysis codes accessed both of the experimental and simulation data to reduce a systematic uncertainty due to the analysis. The simulation data such as deposit energy, particle hit position, etc. were digitized and stored in the same format as the experimental data.

where length is 600 mm. In addition, the target holder, TOF1 and AC PMT supporter made of aluminum were installed.

TOF1: The TOF1 counter was made of a fast plastic scintillating material, and this material properties is defined in the simulation. The TOF1 size is (23.8 mm × 26.5 mm) × 5.0 mm which was arranged in each sector (12 counters in total). When a charged particle deposits the energy in one of the 12 counters, the trigger flag to trace the track was turned on and the energy and timing information were stored.

Spiral fiber tracker: Spiral fiber tracker (SFT) was approximated as two layers of a plastic scintillating cylinder. The inner and outer cylinders have the radius of 84.1 and 87.8 mm, respectively, with a thickness of 1.8 mm [57]. The logical volumes are defined as SFT1 and SFT2. Particle hit positions (x, y, and z) in SFT1 and SFT2 were stored.

Aerogel Cherenkov counter: The silica aerogel material was defined as
$SiO_2 : H_2O : C = 62.5\% : 37.4\% : 0.1\%$ with density of 0.200 g/cm^3. The AC consists of the aerogel, air, and aluminum box cover. When a charged particle passed through and the threshold condition of Cherenkov photon emission was satisfied for refractive index of $n = 1.08$, optical Cherenkov photons were taken into account in principle. However, these optical photons were not used in the E36 simulation calculation. The PMT component was approximated to be a cylinder with outer radius of 47 mm, a thickness of 1.6 mm, and a length of 163 mm, where the material was assumed to be iron. Light guides with an acrylic Winston cone were connected to the PMT. The detector constrain is detail in Ref [57]. They were also approximated to be paraboloid form with the outer radius of 34 mm and the inner radius of 42 mm, where material is defined as $C_5O_2H_8$ with density of 1.18 g/cm^3.

TOF2: The TOF2 counter is made of a plastic scintillating plate with a size of (800 mm × 300 mm) × 20 mm. It notes a length of gap5 and gap7 is set to 680 mm. The particle track was terminated and the next event started in order to speed up the calculation if the daughter charged particle from the K^+ decay did not reach the TOF2 counter. When the particle hit TOF2, the TOF2 trigger flags was turned on.

Thin Trigger Counter: Thin trigger counter (TTC) is also made of a plastic scintillating plate with a size of 500 mm × 243 mm × 3 mm. It notes a length was set to 600 mm for the gap6 counter. When the particle from the K^+ decay hit to TTC, the TTC trigger flag was turn on.

PGC: Details of the PGC arrangement was described in section 4.5.2. PGC were assembled with 7 lead-glass modules (6 modules for gap 5 and 7) with a thickness of 122 mm used in the TOPAZ experiment. The material properties were carefully input in the simulation.

CsI(Tl) photon detector: The number of CsI(Tl) crystals was 768 and covered about 70% of the total solid angle. They were installed to form a barrel structure. An emitted photon from the K^+ decay generated an electro-magnetic shower and the energy deposits of all charged particles in the CsI(Tl) modules were taken into account. Energy sum of the all deposited energy by the electro-

magnetic shower was treated as the observed energy by the CsI(Tl) modules, while the earliest hit timing among the shower particles were interpreted as the observed timing.

MWPC: The MWPCs consist of a frame, Mylar window, gap gas, Kapton strip, Cu strip, and tungsten (W) anode wires. The Mylar thickness is 12 μ. The chamber gas is a mixture of AR : Ethen $= 1 : 1$ with density of 1.81 mg/cm^3. The inner and outer gas volume was defined to be a thickness of 6 mm and 10.6 mm. The Kapton strip, Cu strip, and anode wire were approximated by a thin film with a width of 25 μm, 18 μm, and 20 μm, respectively. The particle hit position on the chambers was defined as the particle position at the anode wire plane and recorded to the data in the simulation.

Gap sandwich counter: The Gap sandwich (GSC) counter was a stacking structure of four layers of Lead plates (990 mm $\times$ 196 mm $\times$ 3.7 mm) and plastic scintillator plates (990 mm $\times$ 196 mm $\times$ 10 mm), i.e. total thickness is 54.8 mm. GSC was set at the position of z $= -93$ mm with 7 deg. inclination with respect to beam direction. Charged particles were bent by the spectrometer and did not hit the counters. The deposit energy and its timing in the scintillator parts was recorded as the GSC data.

5.3   Toroidal magnet and magnetic field

The field map of the toroidal magnet is necessary for the track reconstruction in the momentum analysis. Also, charged particles in the simulation were transported through the spectrometer by referring the calculated field map. By P. Monagan, the toroidal field maps were calculated using a 3-dimensional code TOSCA with several magnet current conditions. The actual field distribution used in the simulation were obtained by linear interpolation from the field distribution of the nearest two magnet currents. Strictly speaking, this operation was not correct because saturation effect of the magnetic field was already being actualized in the region used in the E36 experiment. In this analysis, additional small correction factor was introduced to reproduce the MWPC profiles by the simulation.

5.4   Kaon decay models for two and three body decays

Before starting the $K_{e2\gamma}$ studies, the experimental reproducibility by the simulation has to be checked using major K^+ decay channels of K_{e2}, $K_{\mu2}$, $K_{\pi2}$, and K_{e3} events. The following decay kinematics was assumed in the Monte Carlo simulation, and the simulation results were compared with the experimental ones.

Two body decay is the simplest kinematics. Daughter particles from K^+ decay at rest have monochromatic momenta which can be described as,

$$p = \sqrt{\left(\frac{M_K^2 - M_1^2 + M_2^2}{2M_K}\right)^2 - M_2^2} \tag{66}$$

where M_1 and M_2 are masses of the daughter particles. For the K_{e2} and $K_{\mu2}$ decays, a visible particle is only e^+ (246.8 MeV/c) and μ^+ (235.53 MeV/c), respectively, and they are emitted isotopically. For the $K_{\pi2}$ decay, π^+ and π^0 with the momentum of 205.14 MeV/c are emitted in back-to-back directions, and π^0 decays rapidly into $\pi^0 \to \gamma\ \gamma$ (98.823%) and into $\pi^0 \to e^+e^-\gamma$ (1.174%).

Kinematics of three body K_{e3} decay is summarized by PDG in detail. The Dalitz density can be described using the λ' and λ'' form factors as,

$$\rho \quad \sim A f_+^2 \tag{67}$$

$$f_+ \quad = 1 + \frac{\lambda'_+ t}{M_{\pi^+}^2} + \frac{\lambda''_+}{2} \frac{t^2}{M_{\pi^+}^4}, \tag{68}$$

$$A \quad = \quad 4(z+y-1)(1-y) \tag{69}$$
$$+ \quad r_l(4y+3z-3) \tag{70}$$
$$- \quad 4r_\pi + r_l(r_\pi - r_l), \tag{71}$$

$$y \quad = \frac{2E_l}{M_K}, \quad z = \frac{2E_\pi}{M_K}, \tag{72}$$

$$r_l \quad = \left(\frac{M_l}{M_K}\right)^2, \quad r_l = \left(\frac{M_\pi}{M_K}\right)^2 \tag{73}$$

$$\lambda'_+ \quad = 0.02485, \tag{74}$$

$$\lambda''_+ \quad = 0.00192, \tag{75}$$

$$t \quad = M_k^2 - 2E_{\pi^0} M_k + M_{\pi^0}^2 \tag{76}$$

5.5   Accidental beam backgrounds in the γ analysis

The CsI(Tl) timing spectrum without any event selections was obtained and a sharp peak corresponding to the true coincidence with the K^+ decay was observed, as shown in Fig. 50(a). Accidental backgrounds which have a timing structure of 250 KHz frequency were also observed. It is not easy to verify the backgrounds with sideband events (region 1, 2) and next cycle events (region 3) can correctly reproduce the actual backgrounds below the peak. Therefore, we decided to use the $K_{\mu2}$ decay which does not emit the γ ray and can extract the pure background information. The $K_{\mu2}$ events were selected only using the charged particle analysis (tracking and PID). The cluster energy distribution is shown in Fig. 50(b). About 20% of the total events have the finite photon clusters, and we concluded that the contribution of these accidental backgrounds has to be carefully estimated in the $K_{e2\gamma}^{\mathrm{SD}}$ analysis. In addition to this $K_{\mu2}$ background method, the side band events were also used as accidental backgrounds by adopting wider timing windows, which was treated as a systematic uncertainty effect.

On the other hand, radiative $K^+ \to \mu^+\nu\gamma$ decays can generate photons at the trigger timing, however the photon energy of the IB component is low. Also, the SD component is negligible compared with IB. Actually we searched for the $K_{\mu2\gamma}$ events in the $K_{\mu2}$ sample using the CsI(Tl) and GSC data, but we could not find them. Therefore, real photon fraction in the background sample are negligibly small and does not affect these studies for the accidental backgrounds.

We once produced the data sample of the $K_{\mu2}$ events using the standard photon gate window, and we merged these $K_{\mu2}$ events to the simulation data of the $K_{e2\gamma}^{\mathrm{SD}}$ decays. Since the background fraction is considered to be dependent on the beam rate, the $K_{\mu2}$ samples were collected using all run data.
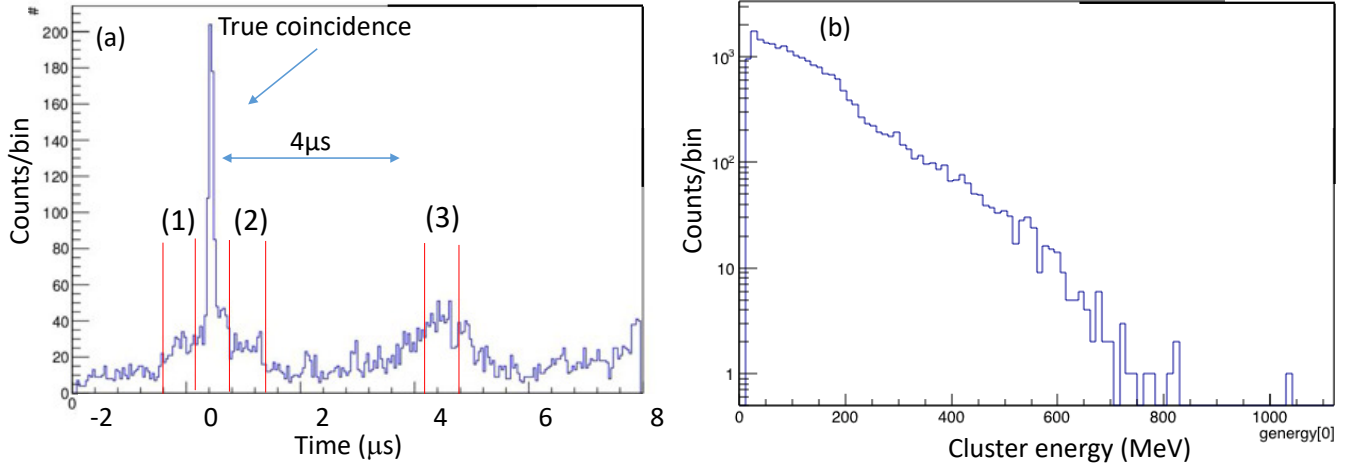
Figure 50: (a) The CsI(Tl) timing spectrum without any event selections and (b) the cluster energy distribution of accidental backgrounds. A sharp peak corresponding to the true coincidence with the K^+ decay was seen. Accidental backgrounds which have a timing structure of 250 KHz frequency were also observed.

The validity of this simulation method was checked using two photons ($E_{\gamma 1} > E_{\gamma 2}$) from the π^0 decay in $K^+ \rightarrow \pi^+ \pi^0$ tagged by the π^+ with $200 < p_\pi < 210$ MeV/c and the photon energy higher than 21 MeV. Also, events with large shower leakage from the calorimeter were rejected by requiring $E_{\gamma 1} + E_{\gamma 2} > 120$ MeV. Figure 51 shows the experimental spectra (dots) of (a) $E_{\gamma 1}$, (b) $E_{\gamma 2}$, (c) opening angle between the two photons, and (d) invariant mass ($M_{\gamma\gamma}$), together with the simulation data. The contribution from the π^0 decay and events with at least one accidental background hit in the two clusters are shown as the dashed (blue) and dotted (green) histograms, respectively. The solid (red) histogram is obtained by summing the two components and normalizing to the experimental yield. The simulation calculations are in good agreement with the experimental data, which indicates a good understanding of the photon measurement by the CsI(Tl) calorimeter. Also, the detection efficiencies of all CsI(Tl) modules were determined using the $K_{\pi 2}$ events. Using the information of the π^+ and one of the two photons, the second photon energy and direction were calculated, and the existence of the actual photon cluster was checked. It can be concluded that the $K_{\pi 2}$ kinematics was correctly understood in the simulation.

5.6   GSC efficiency difference between the MC and experiment

The radiative photons cannot be perfectly detected by GSC due to the finite probability of the photon interaction with the lead materials and the hardware threshold in the signal readout, although the former effect was only taken into account in the Monte Carlo simulation. Therefor the GSC efficiency in MC simulation is little larger than that in the experiment. The $\Omega(K_{e2\gamma}^{SD})$ value in Eq15 cannot be calculated directly in GSC analysis and need to be corrected using the ratio of the GSC efficiency between MC and the experiment.

The GSC efficiency in the experiment relative to that in the Monte Carlo simulation was measured
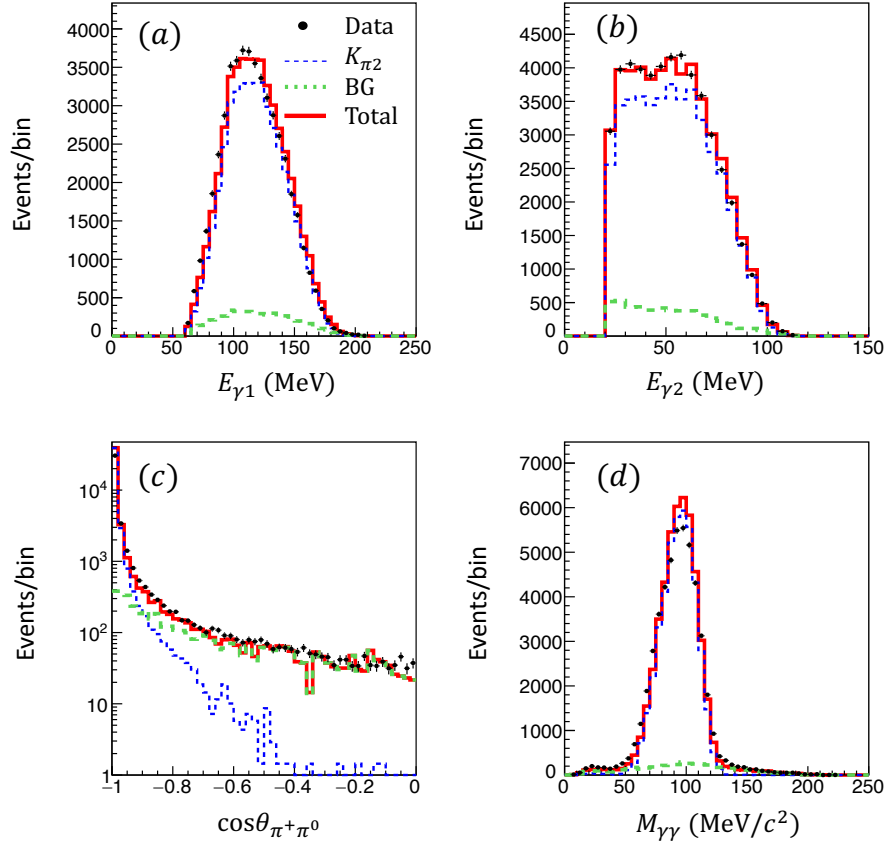
Figure 51: $K_{\pi 2}$ spectra compared with the MC simulation taking into account the accidental backgrounds in the CsI(Tl) calorimeter. (a) and (b) are the photon energy distributions ($E_{\gamma 1} > E_{\gamma 2}$), (c) is the opening angle between the π^+ and π^0, and (d) is the invariant mass $M_{\gamma\gamma}$. The black dots are the experimental data. The contribution from the π^0 decay and events with at least one of the two clusters being accidental are shown as the dashed (blue) and dotted (green) histograms, respectively, and the solid (red) histogram is obtained by summing the two components.

using the $K^+ \to \pi^+\pi^0$ ($K_{\pi2}$) decays with an escaping photon passing through the holes. One photon cluster events in the CsI(Tl) calorimeter were selected, and the information of the escaping photon was calculated by requiring the $K_{\pi2}$ kinematics, as shown in Fig. 52. Events with one photon cluster (γ_1) were selected by requiring $200 < p < 210$ MeV/c and $130^2 < M^2_{\mathrm{TOF}} < 140^2$ MeV$^2/c^4$, as shown in Fig. 53(a), where M^2_{TOF} is the mass-squared of charged particle obtained from the time-of-flight, momentum, and path length. Here it should be noted that the accidental backgrounds were taken into account in the simulation to reproduce the experimental $K_{\pi2}$ distributions. In order to reduce the effects of shower leakage, the γ_1 energy was calculated from the opening angle between the γ_1 and π^0 directions ($\theta_{\pi^0\gamma_1}$) assuming the $K_{\pi2}$ kinematics as,

$$E_{\gamma_1} = M^2_{\pi^0}/(2p_{\pi^0})\frac{1}{\sqrt{1 + (M_{\pi^0}/p_{\pi^0})^2} - \cos\theta_{\pi^0\gamma_1}}, \tag{77}$$

where M_{π^0}=135 MeV/c^2 is the π^0 rest mass and p_{π^0}=205 MeV/c is the π^0 momentum. The energy and direction of the escaping photon (γ_2) were calculated from the γ_1 and π^+ information. The γ_2 photons were further selected by requiring the photon passage through the muon holes using the γ_2 direction and the K^+ decay vertex, as shown in Fig. 53(b). The dots shown in Fig. 53(c) and (d) are the γ_1 and γ_2 polar angle distributions, respectively, and the red lines are the simulation calculation. They are in good agreement, which indicates that the energy and direction of the escaping photons were correctly determined from the γ_1 and π^+ information.
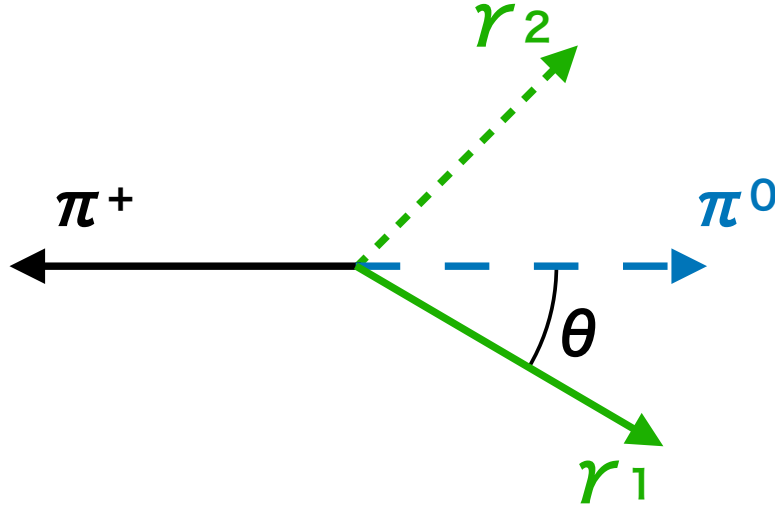
Figure 52: The $K_{\pi2}$ events used for the GSC efficiency determination. In order to reduce effects of shower leakage, the γ_1 energy was calculated from the γ_1 and π^+ directions assuming the $K_{\pi2}$ decay kinematics. Then, the γ_2 photon energy and direction were calculated from the γ_1 and π^+ information.

A quantity ξ, which is the product of the GSC acceptance and efficiency, was defined as,

$$\xi = N(\mathrm{GSC})/N(\mathrm{EP}), \tag{78}$$
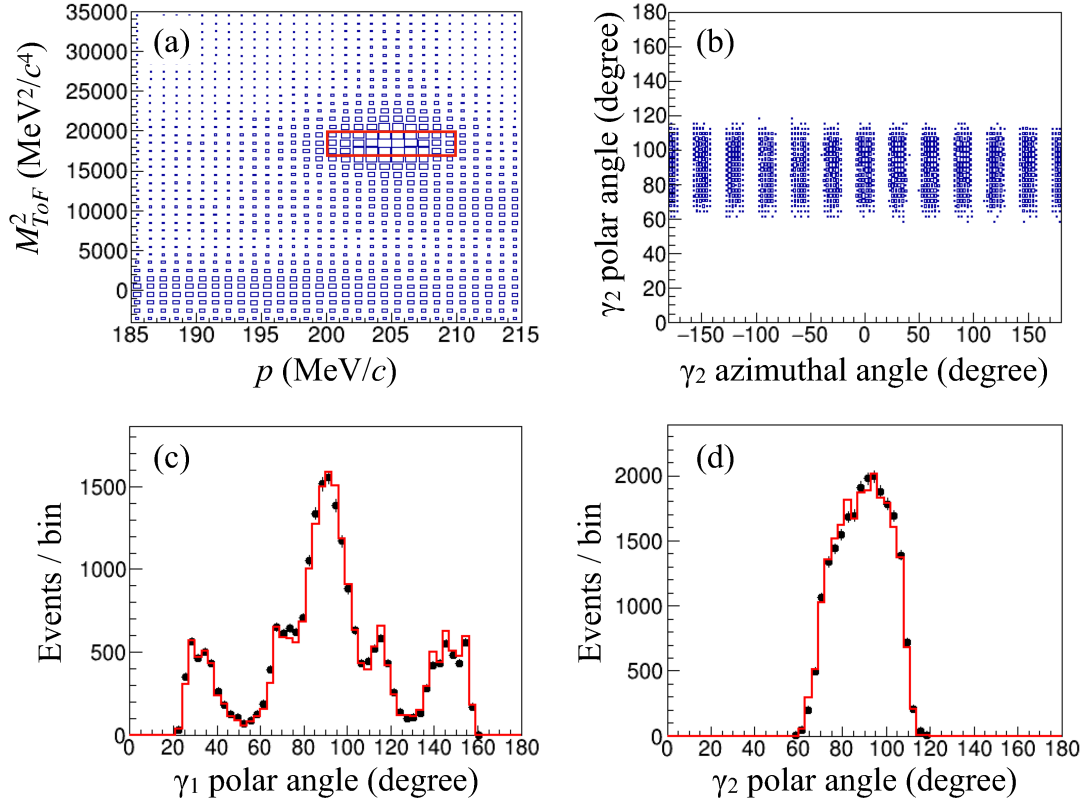
Figure 53: The $K_{\pi 2}$ decays were selected by the cut window of the (p, M_{TOF}^2) correlation, as shown in (a). Then, requiring the 1-cluster hit in the CsI(Tl) calorimeter, the $K_{\pi 2}$ events were further selected: (b) polar-azimuthal angular distribution of the γ_2 photon, and polar angle distributions of the (c) γ_1 and (d) γ_2 photons. The simulation histograms (red line) in (c) and (d) are in good agreement with the experimental ones (dots).

where $N(\mathrm{EP})$ and $N(\mathrm{GSC})$ are the numbers of the photons passing through the holes obtained in the above analysis and the actual GSC hit events, respectively. Then, the GSC efficiency ratio, $R_\xi = \xi_{\mathrm{Exp}}/\xi_{\mathrm{MC}}$, were determined using the experimental GSC data and the simulation calculation was determined. The reduction of the the R_ξ value, 15 from the unity was adopted as the detector inefficiency due to the hardware threshold effect. Figure 54 (a) and (b) show the ξ and R_ξ values, respectively, obtained as a function of the γ_2 energy. The ξ values below the 200 MeV are distributing $10-20\%$, because the GSC acceptance for the escaping photons is $\sim 30\%$ and the photon conversion probability is $\sim 70\%$, as well as the CsI(Tl) inefficiency for low energy photons. On the other hand, opening angle between the photon and π^+ for events with the γ_2 energy higher than 200 MeV is strongly constrained in the back-to-back direction because of the $K_{\pi 2}$ kinematics. Consequently, most of the γ_2 photons were directed toward GSC and the ξ value is $\sim 50\%$. Since the photon conversion probability was taken into account in the simulation, the R_ξ distribution has a nearly flat structure over the entire photon energy region. The R_ξ drop in the low energy region is most likely due to imperfect reproducibility of the experimental conditions by the simulation for low energy photons. The R_ξ around $160-200$ MeV, which corresponds to the dominant parts of the radiated photon from the $K_{e2\gamma}^{\mathrm{SD}}$ decay, was obtained to be 0.97 ± 0.04.
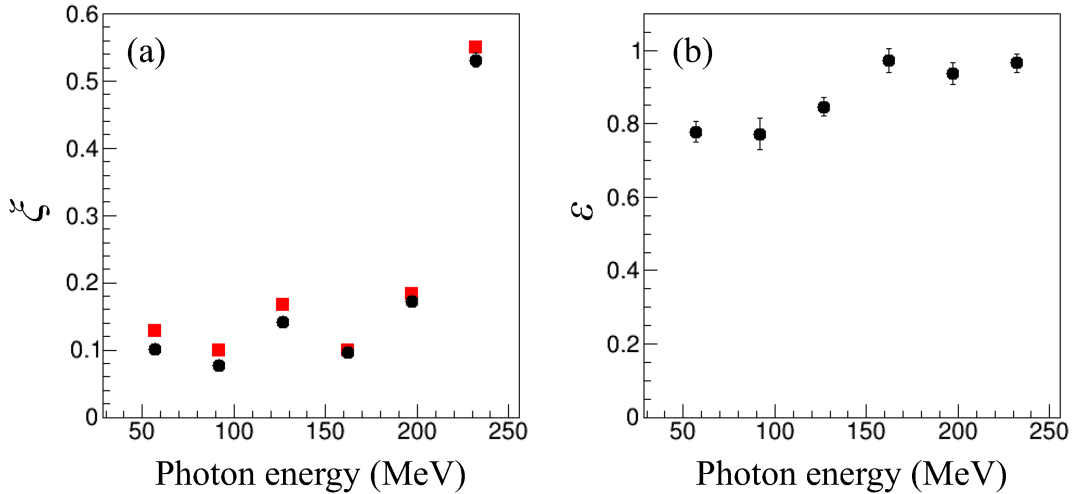
Figure 54: (a) ξ values obtained as a function of the photon energy for the experimental (circle/black) and simulation (square/red) data, and (b) GSC efficiency ratio, R_ξ, calculated as $R_\xi = \xi_{\mathrm{Exp}}/\xi_{\mathrm{MC}}$. They are obtained using the $K_{\pi 2}$ events with one photon escaping through the CsI(Tl) holes.

By using the R_ξ value, Eq.15 in GSC analysis is modified as

$$\frac{Br(K_{e2\gamma}^{\mathrm{SD}})}{Br(K_{e2(\gamma)})} = \frac{N(K_{e2\gamma}^{\mathrm{SD}})}{N(K_{e2(\gamma)})} \cdot R_\Omega \cdot \frac{1}{R_\xi} = \frac{N(K_{e2\gamma}^{\mathrm{SD}})}{N(K_{e2(\gamma)})} \cdot \frac{\Omega(K_{e2(\gamma)})}{\Omega(K_{e2\gamma}^{\mathrm{SD}})} \cdot \frac{\xi_{\mathrm{MC}}}{\xi_{\mathrm{Exp}}}, \tag{79}$$

5.7 Output data from the simulation

The MC data stored in each detector system were recorded in file in the following data structure. The analysis program developed for the experimental data in the KEKCC server accessed to the

simulation output files and analyzed them in the same manner as the experimental data. Therefore, the main analysis framework such as target pattern recognition, particle tracking, PID, and CsI clustering are actually common in order reduce the systematic effect due to the analysis. The MC data was recorded to the files output when the hit-flags were coincided for target, TOF1, TOF2, C2, C3, C4, and TTC.

Here, we just summarize the output structure of the simulation data as follows. The Pass1 codes accessed to these files and analyze the simulation data using the same analysis programs as the experimental data. The original information such as position, direction, energy, particle-id, etc. at birth were also stored in the data, as listed in Table 16.

Table 16: Output data component

variable	Array	Unit
event number	1	
kaon stop position	3	cm
c2 hit position	3	cm
c3 hit position	3	cm
c4 hit position	3	cm
Target fiber deposit energy	256	MeV
Target fiber hit time	256	ns
Target fiber Track ID	256	
TOF1 hit position	$3 \times [5]$	cm
TOF1 hit time	[5]	ns
TOF1 track ID	[5]	
SFT1 hit position	$3 \times [5]$	cm
SFT1 hit time	[5]	nc
SFT1 track ID	[5]	
SFT2 hit position	$3 \times [5]$	cm
SFT2 hit time	[5]	nc
SFT2 track ID	[5]	
AC hit position	$3 \times [5]$	cm
AC hit time	[5]	nc
AC mass	[5]	MeV/c^2
AC track ID	[5]	
TOF2 hit position	$3 \times [5]$	cm
TOF2 hit time	[5]	nc
TOF2 track ID	[5]	
TTC deposit energy	12	MeV
TTC hit time	12	nc
PGC deposit energy	84	MeV
PGC hit time	84	nc
PGC Cherenkov photon yield	84	photons
PGC trackID	84	
PGC hit ID in module	1	
CsI deposit energy	768	MeV
CsI hit time	768	nc
Primary momentum	3	MeV/c
A flag of $K_{\pi 2}$ dalitz decay	1	

6 $Br(K_{e2\gamma}^{\mathrm{SD}})/Br(K_{e2(\gamma)})$ determination

6.1 Advantages to adopt the E36 experimental procedure

Before starting the $Br(K_{e2\gamma}^{\mathrm{SD}})/Br(K_{e2(\gamma)})$ determination, it is worthwhile to summarize the experimental advantages to adopt the E36 procedure. Our method has the following advantages: (1) charged particles from the $K_{e2(\gamma)}$ and $K_{e2\gamma}^{\mathrm{SD}}$ decays are e^+ with similar momenta, and the PID efficiency up to a small p dependence cancels out, (2) since the $K_{e2(\gamma)}$ decay produces a peak at 247 MeV/c in the momentum spectrum, the $K_{e2(\gamma)}$ yield can be accurately determined, and, at the same time, the $K_{e2(\gamma)}$ events are largely suppressed by requiring a photon hit in the photon counters for the $K_{e2\gamma}^{\mathrm{SD}}$ selection, (3) the photon counters acceptance can be determined using the photons from the $K_{\pi2}$ decay, (4) other systematic uncertainties from imperfect reproducibility of the experimental conditions such as tracker inefficiencies, detector misalignment, DAQ deadtime, etc. are also cancelled out in the ratio determination.

6.2 Charged particle analysis

Fig.55(a) shows the charged particle momentum spectrum without any constraint. The peak structure due to the predominant $K_{\mu2}$ and $K_{\pi2}$ decays is visible at 236 MeV/c and 205 MeV/c, respectively. From this data, we extract e^+ events with the following conditions as

- Flight length > 240 cm

- K$^+$ stopping position $r < 3$ cm

- Tracking χ^2/n.d.f $< 50/4$

- gd_ehole flag $= 1$

- ktime > 1.5 ns

- PID condition

    - ACADC > 100
    - PGCADC > 140
    - TOFMASS < 4000

The momentum determination for charged particles passing thought the spectrometer edge, resulting short flight path length of < 240 cm, was not reliably performed, because the field distribution was not correctly calculated and bending angle of changed particle was small, corresponding to bad momentum resolution. The radius of the K^+ stopping target was 3cm, and events with K^+ decay outside the target were rejected. The $K_{\mu2}$ peak widths were checked by slicing the tracking χ^2 distribution and wider peaks were observed for events with the tracking $\chi^2 > 50$. Since some charged particle grazed CsI(Tl) module and accepted by the spectrometer, events with CsI(Tl) module hit around the muon hole which charged particle passed were rejected. The K^+ decay time, defined as
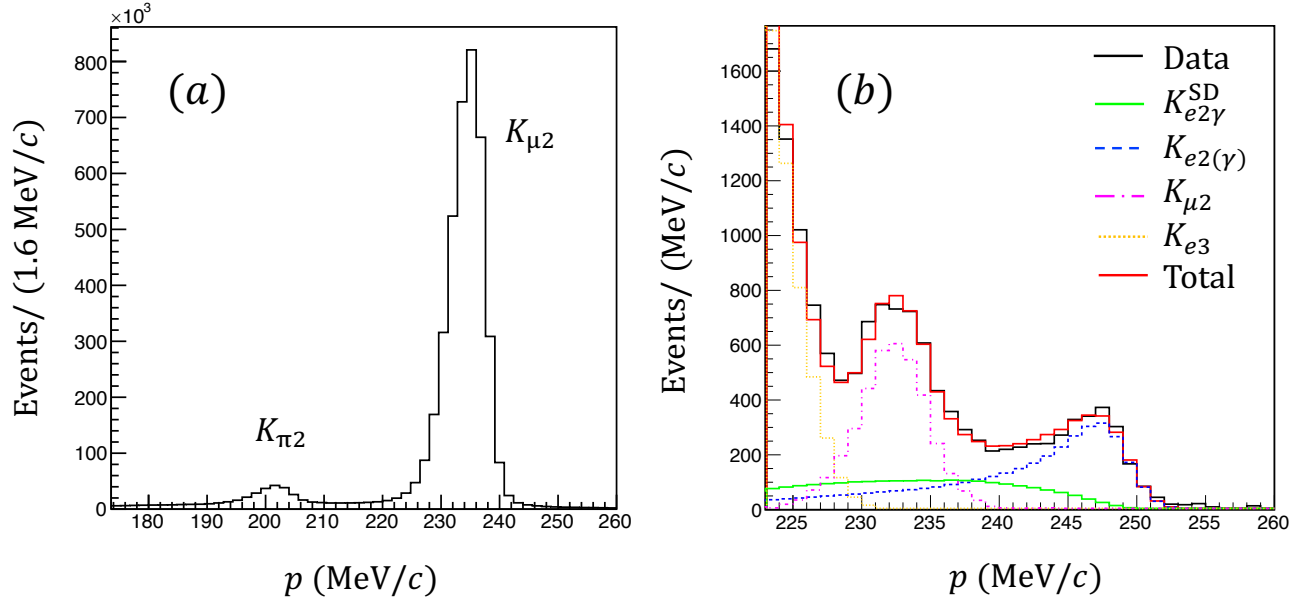
Figure 55: (a) and (b) are the momentum spectra corrected for the energy loss in TGT before and after imposing the positron selection PID, respectively, before requiring the photon detection by CsI(Tl). The peak structure due to the predominant $K_{\mu2}$ and $K_{\pi2}$ decays is seen at 236 MeV/c and 205 MeV/c, respectively, in (a). The $K_{\pi2}$ decay is reduced due to the momentum acceptance of the spectrometer. The $K_{e2(\gamma)}$ and K_{e3} decays, as well as the remaining $K_{\mu2}$ events due to μ^+ mis-identification are presented in (b). The $K_{e2(\gamma)}$ peak is observed with a tail structure in the lower momentum region due to the emission of internal and external bremsstrahlung before entering the spectrometer. The momentum in (b) was scaled so that the $K_{e2(\gamma)}$ peak position is at 247 MeV/c, and consequently the $K_{\mu2}$ peak position appears at 233 MeV/c. The e^+ momentum below 225 MeV/c is not usable for the $K_{e2\gamma}^{\mathrm{SD}}$ and $K_{e2(\gamma)}$ decays due to the high K_{e3} contribution. The $K_{e2\gamma}^{\mathrm{SD}^+}$, $K_{e2(\gamma)}$, K_{e3} and $K_{\mu2}$ decays determined by simulation calculations are also shown in (b).

the time of the e^+ signale at the TOF1 counter, was required to be more than 1.5 ns later than the K^+ arrival time determined by the beam Cherenkov counter to suppress the fraction of in-flight K^+ decays and any other prompt backgrounds to be 0.1%.

Positrons were selected by setting thresholds for AC and PGC at channel 100 and 140, respectively. Also, the mass-squared of the charged particle (M_{TOF}^2) obtained from the TOF, momentum, and path length was required to be $M_{\mathrm{TOF}}^2 < 4000$ (MeV$^2/c^4$). These positron selection cuts were chosen to remove most of the $K_{\mu 2}$ backgrounds with a μ^+ rejection probability of $(99.934\pm0.002_{\mathrm{stat}})$%, while maintaining a reasonable e^+ efficiency of $(75.2\pm0.4_{\mathrm{stat}})$%. This was determined to minimize the total uncertainty in the $K_{e2\gamma}^{\mathrm{SD}}$ branching ratio measurement from the $K_{\mu 2}$ subtraction. Here, the branching ratio of the $K_{e2\gamma}^{\mathrm{SD}}$ decay was determined by changing the PID selection conditions in the (AC, PGC, TOF) cut-point space and the statistical uncertainty was obtained in each cut point. Left figure in Fig. 56 shows the uncertainty distribution, $\Delta Br(K_{e2\gamma}^{\mathrm{SD}})/Br(K_{e2(\gamma)})$, in the cut point space of (PGC ADC, TOF MASS) by fixing AC ADC at 100, and the optimum cut point chosen as the minimum uncertainty is shown as the dot. Right figure in Fig. 56 is the contour plots for the e^+ efficiency (black) and the μ^+ rejection probability (red), where the black and red arrows are increasing and decreasing directions for the e^+ efficiency and the μ^+ rejection probability, respectively. The overall e^+ efficiency and the μ^+ mis-identification probability using TOF, AC, and PGC can be calculated using the efficiency curves shown in Fig.42.
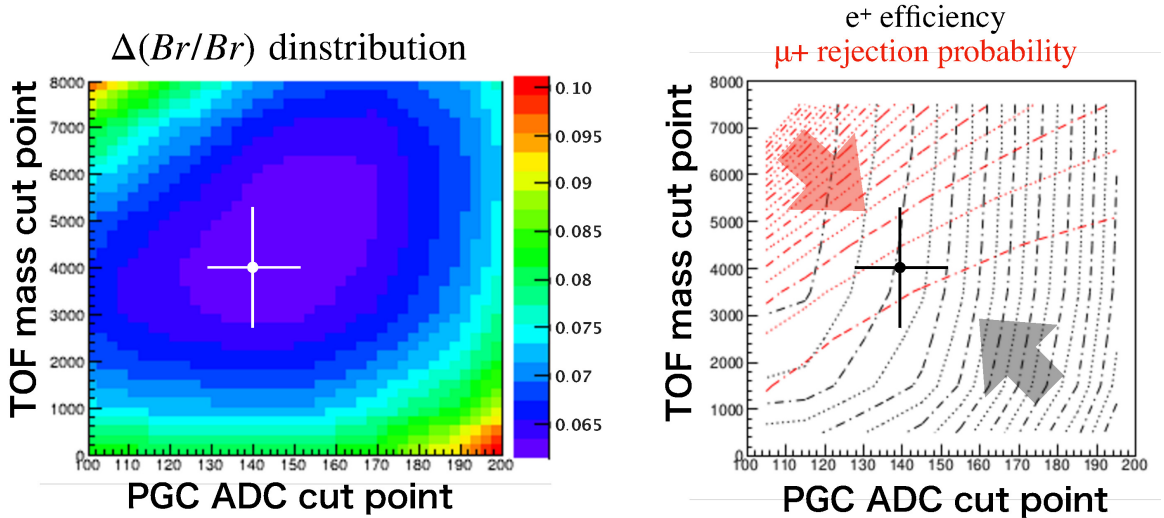
Figure 56: (Left) The uncertainty distribution in the cut point space of (AC ADC, TOF MASS), (right) the contour plot for the e^+ efficiency and the μ^+ rejection probability. The optimum cut point chosen as the minimum uncertainty is shown as the dot. The black and red arrows are increasing direction for the e^+ efficiency and the μ^+ rejection probability, respectively.

Fig. 55(b) shows the obtained e^+ momentum spectrum. The black dot is the experimental data. The blue dashed, green solid, yellow dotted, and magenta dotted-dashed lines correspond to the MC $K_{e2(\gamma)}$, $K_{e2\gamma}^{\mathrm{SD}}$, K_{e3}, and $K_{\mu 2}$ decays, respectively, and the red thick line is total simulation obtained by summing up each component. The $K_{e2(\gamma)}$ and K_{e3} decays, as well as the remaining $K_{\mu 2}$ events due to μ^+ mis-identification are presented. The $K_{e2(\gamma)}$ peak is observed with a tail structure in the lower

momentum region due to the emission of internal and external bremsstrahlung before entering the spectrometer. The momentum in (b) was scaled so that the $K_{e2(\gamma)}$ peak position is at 247 MeV/c, and consequently the $K_{\mu2}$ peak position appears at 233 MeV/c. The e^+ momentum below 225 MeV/c is not usable for the $K_{e2\gamma}^{\mathrm{SD}}$ and $K_{e2(\gamma)}$ decays due to the high K_{e3} contribution.

6.3 $Br(K_{e2\gamma}^{\mathrm{SD}})/Br(K_{e2(\gamma)})$ determination by using CsI(Tl)

In order to select the $K_{e2\gamma}^{\mathrm{SD}}$ events, photon hits in the CsI(Tl) calorimeter were required. Due to pile-up of the accidental backgrounds in the CsI(Tl), the accepted $K_{e2\gamma}^{\mathrm{SD}}$ events included 2-cluster events in the calorimeter with a ratio of the ϵ probability obtained using $K_{\mu2}$ events compared with 1-cluster events. Since event loss in the 1-cluster data and the appearance of the 2-cluster events were taken into account in the simulation, the $K_{e2\gamma}^{\mathrm{SD}}$ branching ratio can be derived by comparing the experimental data with the simulation for both the 1-cluster and 2-cluster events simultaneously.

The $K_{e2\gamma}^{\mathrm{SD}}$ decays with 1-cluster in the CsI(Tl) were obtained using the following procedure. The photon energy was required to be $E_\gamma > 21$MeV. This E_γ cut point was a little higher than the hardware threshold to remove effects from small gain variations of each CsI(Tl) module. Fig.57 show the distributions of (a) the opening angle between the e^+ and γ and (b) the missing-mass-squared calculated as $M_{\mathrm{miss}}^2 = (m_K - E_e - E_\gamma)^2 - (\mathbf{p_e} + \mathbf{p}_\gamma)^2$ where $\mathbf{p}$ is the momentum vector, assuming the $K^+ \to e^+\nu\gamma$ decay kinematics. In order to suppress the $K_{\mu2}$ background events, $\cos\theta_{e\gamma} < -0.8$ and $-4000 < M_{\mathrm{miss}}^2 < 8000$ MeV^2/c^4 were required. These cut points were determined to reject the $K_{\mu2}$ and K_{e2} events, keeping nearly 100% of the $K_{e2\gamma}^{\mathrm{SD}}$ events. The momentum spectrum is shown in Fig. 58 (a) indicated by the dots. Here, a small contribution from $K_{\mu2}$ with an accidental hit remained after the $K_{e2\gamma}^{\mathrm{SD}}$ selection cuts. The $K_{e2\gamma}^{\mathrm{SD}}$ decays obtained in the 2-cluster data were selected in a similar manner. If one of the two clusters satisfied the conditions for the 1-cluster analysis, the event was adopted as a $K_{e2\gamma}^{\mathrm{SD}}$ decay and the associated CsI(Tl) cluster was chosen as the true photon event, as shown in Fig. 58 (b). It should be noted that the $K_{\mu2}$ surviving fraction relative to the $K_{e2\gamma}^{\mathrm{SD}}$ yield in the 2-cluster data is approximately twice that observed in the 1-cluster data because there are two photon candidates in the 2-cluster analysis. The $Br(K_{e2\gamma}^{\mathrm{SD}})/Br(K_{e2(\gamma)})$ value was obtained to be 1.14 ± 0.07 by simultaneously fitting the momentum spectra of the events with 1-cluster, 2-cluster, and without CsI(Tl) constraint using the simulation data of the $K_{e2\gamma}^{\mathrm{SD}}$, $K_{e2(\gamma)}$, and $K_{\mu2}$ decays, as shown in Fig. 58 (a)(b)(c). Here, the $Br(K_{e2\gamma}^{\mathrm{SD}})/Br(K_{e2(\gamma)})$ value defined in Eq. 15 and the $K_{e2\gamma}^{\mathrm{SD}}$ yield in the 1-cluster data were the fitting parameters in order to simultaneously reproduce the three momentum spectra using the R_Ω values obtained in the MC simulation. The $K_{\mu2}$ yields in each momentum spectrum were also treated as fitting parameters in order to subtract them. The solid (green), dotted (blue), and dashed-dotted (magenta) lines are the decomposed $K_{e2\gamma}^{\mathrm{SD}}$, $K_{e2(\gamma)}$, and $K_{\mu2}$ events. The thick-red line is the fitted result obtained by adding all the decay contributions. The fitting regions of $p > 230, 232$, and 240 MeV/c for the events with 1-cluster, 2-cluster, without CsI(Tl) constraint, respectively, were chosen to reduce the effects from the $K_{\mu2}$ subtraction to minimize the uncertainty of $K_{e2\gamma}^{\mathrm{SD}}$ by eliminating most of the $K_{\mu2}$ events. Note that it is very difficult to reproduce these surviving $K_{\mu2}$ events after the PID selection and the M_{miss}^2, $\cos\theta_{e\gamma}$, E_γ cuts by the simulation. The $Br(K_{e2\gamma}^{\mathrm{SD}})/Br(K_{e2(\gamma)})$ result as well as the accepted $K_{e2\gamma}^{\mathrm{SD}}$ and $K_{e2(\gamma)}$ yields and the associated R_Ω values are given in Table 17 entitled as physics run (Prun) along with the statistical uncertainties from the fits. On the other hand, the statistical uncertainty of R_Ω obtained from the MC calculation
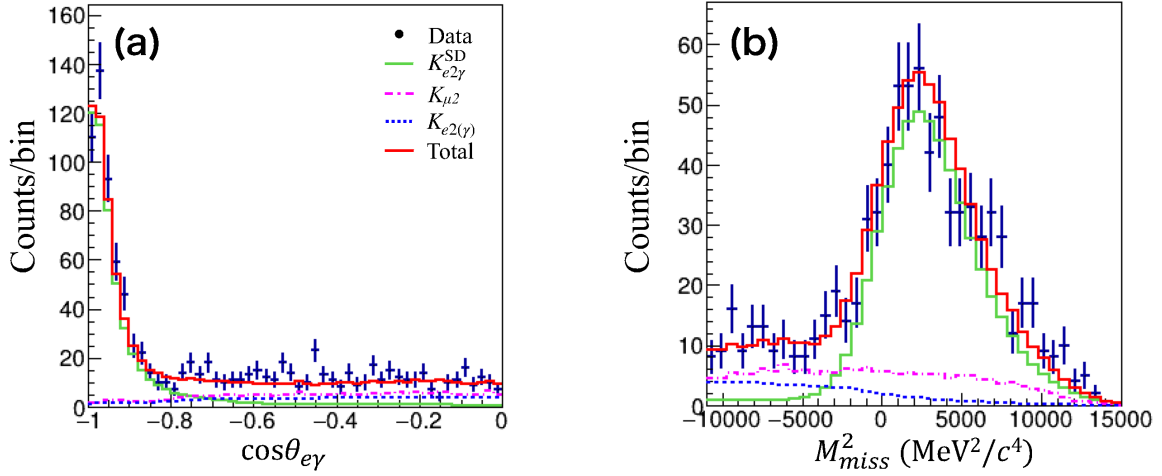
Figure 57: The spectra with the 1-cluster requirement: (a) $\cos\theta_{e\gamma}$ and (b) M^2_{miss}. The black dots are the experimental data. The solid (green), dashed-dotted (magenta),dotted (blue) histograms are the simulation data of $K^{\mathrm{SD}^+}_{e2\gamma}$, $K_{\mu2}$ and K_{e2} with accidental backgrounds, respectively. The thick-red line is the total simulation result obtained by adding each component. In order to suppress the $K_{\mu2}$ and K_{e2} background events, $\cos\theta_{e\gamma} < -0.8$ and $-4000 < M^2_{\mathrm{miss}} < 8000$ MeV$^2/c^4$ were required. These cut points were determined to reject the $K_{\mu2}$ and K_{e2} events, keeping nearly 100% of the $K^{\mathrm{SD}}_{e2\gamma}$ events.

was less than 10^{-3}.

6.4 Checking reproducibility in the simulation

6.4.1 $K^{\mathrm{SD}}_{e2\gamma}$ kinematics

The events in Fig. 58 (a) were used for an event selection validity check. Figure 59 shows the distribution of (a) E_γ, (b) $\cos\theta_{e\gamma}$, and (c) M^2_{miss}. The $K_{\mu2}$ background fraction in Fig. 59 was successfully suppressed down to ~2% of the $K^{\mathrm{SD}}_{e2\gamma}$ yield in the fitted momentum range. The experimental data (dots) are in good agreement with the simulation (thick-solid/red), indicating a correct understanding of the $K^{\mathrm{SD}}_{e2\gamma}$ acceptance. The decomposed $K^{\mathrm{SD}}_{e2\gamma}$ (solid/green) and $K_{\mu2}$ (dashed-dotted/magenta) contributions are also shown.

6.4.2 SC run

In this experimental study, one of the key issues is the treatment of the accidental backgrounds in the CsI(Tl) calorimeter and the $K_{\mu2}$ backgrounds that survive after the PID analysis. In order to validate this analysis method, the Crun data (see section 4.1) taken during the commissioning runs dedicated to K^+ beam and PID detector tuning were used. As a result, the surviving $K_{\mu2}$ fraction in the Crun data was a factor of ~3 higher than in the Prun data. These data samples were independently analyzed using the same analysis codes adopted for the Prun data. The e^+ momentum spectra were obtained using the same PID condition for events with the 1-cluster, 2-cluster, and without any CsI(Tl) constraint, as shown in Fig. 60 (a), (b), and (c), respectively, indicated by the dots. The
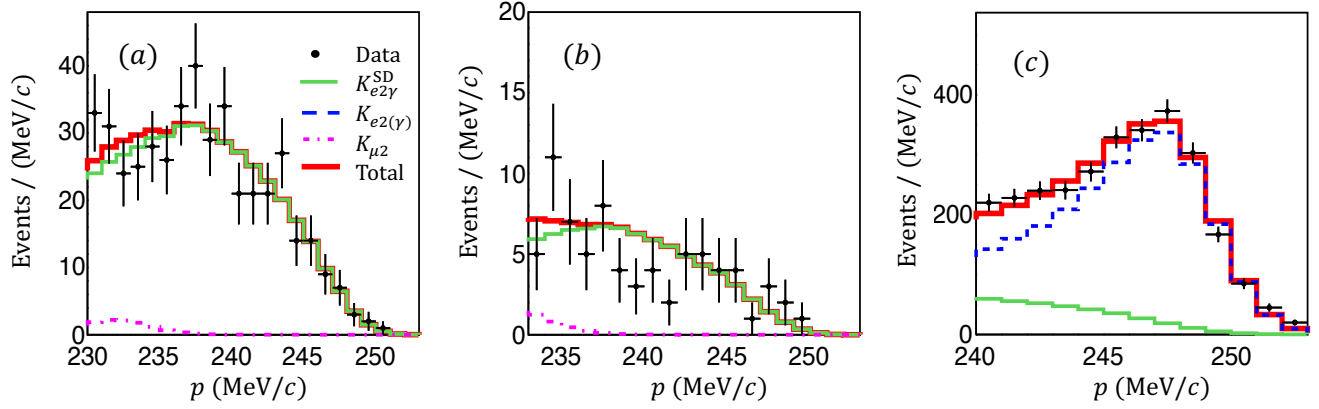
Figure 58: Charged-particle momentum spectra with requiring (a) one photon cluster and (b) two photon clusters in coincidence with the e^+ track, and (c) charged particles without any CsI(Tl) constraint. The dots (black) are the experimental data. The solid (green), dashed (blue), and dashed-dotted (magenta) lines are the $K_{e2\gamma}^{SD^+}$, $K_{e2(\gamma)}$, and $K_{\mu2}$ decays, respectively, determined by simulation calculations. The thick-red lines are the fitted results obtained by adding all the decay contributions. The events are shown only for the fitted momentum range.

Table 17: Results of the individual counts N, acceptance ratio R_Ω, and $Br(K_{e2\gamma}^{SD})/Br(K_{e2(\gamma)})$ values with statistical uncertainties obtained by simultaneously fitting the events with 1-cluster, 2-cluster, and without CsI(Tl) constraint for Prun and Crun. An error-weighted average of the Prun and Crun results was adopted as the final result. Also, $N(K_{e2(\gamma)})$, $N(K_{e2\gamma}^{SD})$, $N(K_{\mu2})$ in the fitting regions of $p > 230$, 232, and 240 MeV/c for the events with 1-cluster, 2-cluster, without CsI(Tl) constraint, respectively, are given.

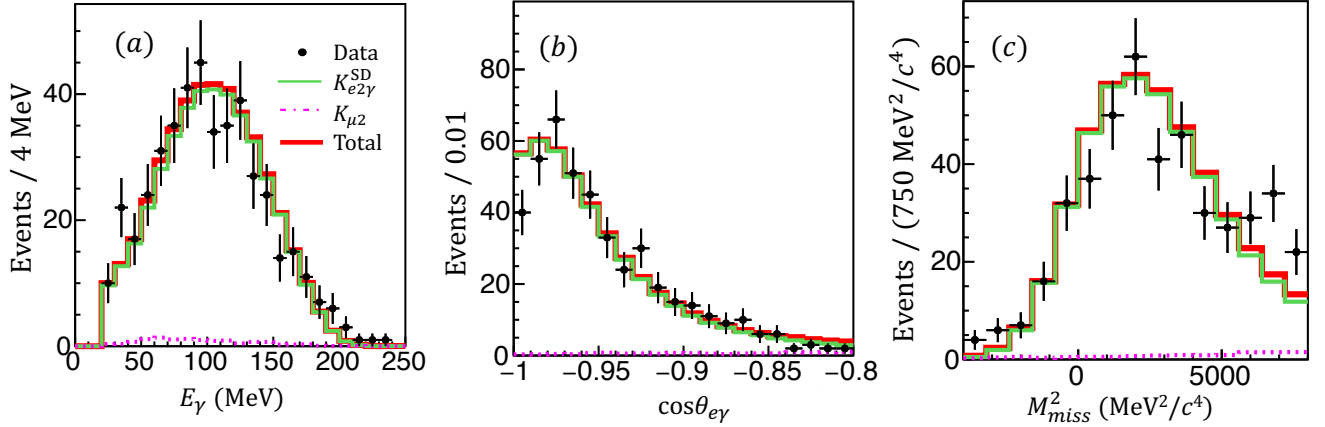|	Run period	Prun	Crun	Combined
Without CsI(Tl) constraint	$N(K_{e2(\gamma)})$	2353 ± 55	330 ± 21	2684 ± 59
	$N(K_{e2\gamma}^{SD})$	355 ± 19	44 ± 7	399 ± 20
1 cluster	$N(K_{e2\gamma}^{SD})$	432 ± 24	56 ± 9	488 ± 26
	$N(K_{\mu2})$	11 ± 16	11 ± 7	22 ± 17
	R_{Ω_1}	6.22	5.83	
2 cluster	$N(K_{e2\gamma}^{SD})$	77 ± 4	9 ± 1	86 ± 4
	$N(K_{\mu2})$	3 ± 5	3 ± 3	6 ± 6
	R_{Ω_2}	34.8	38.4	
Results	χ^2/dof	36.7/43	51.7/43	
	$N(K_{e2\gamma}^{SD})$	509 ± 28	65 ± 10	574 ± 30
	$N(K_{\mu2})$	14 ± 17	14 ± 8	28 ± 19
	$Br(K_{e2\gamma}^{SD})/Br(K_{e2(\gamma)})$	1.14 ± 0.07	1.0 ± 0.2	1.12 ± 0.07

Figure 59: The $K_{e2\gamma}^{\mathrm{SD}}$ spectra with the 1-cluster requirement: (a) E_γ, (b) $\cos\theta_{e\gamma}$, and (c) M_{miss}^2. The $K_{e2\gamma}^{\mathrm{SD}}$ events were selected by imposing $p > 230$ MeV/c, $-4000 < M_{\mathrm{miss}}^2 < 8000$ MeV^2/c^4, and $\cos\theta_{e\gamma} < -0.8$ to suppress the K_{e3} and $K_{\mu2}$ contributions. The black dots are the experimental data. The solid (green) and dashed-dotted (magenta) histograms are the simulation data of $K_{e2\gamma}^{\mathrm{SD}}$ and $K_{\mu2}$ with accidental backgrounds, respectively. The thick-red line is the total simulation result obtained by adding each component.

$Br(K_{e2\gamma}^{\mathrm{SD}})/Br(K_{e2(\gamma)})$ ratio was derived to be 1.0 ± 0.2, which is consistent with the result using the Prun data in spite of the larger number of $K_{\mu2}$ background events. The solid (green), dashed (blue), and dashed-dotted (magenta) lines in Fig. 60 are the $K_{e2\gamma}^{\mathrm{SD}}$, $K_{e2(\gamma)}$, and $K_{\mu2}$ decays, respectively, obtained by the simulation calculation. The thick-red line is the fitted result obtained by adding all the decay contributions. The details of the analysis result are summarized in Table 17. In addition to the Crun analysis described above, a separate study was performed with the Prun data. The cuts were tightened to remove most of the $K_{\mu2}$ background events and relaxed to accept the genuine $K_{e2\gamma}^{\mathrm{SD}}$ events with higher efficiency, although the statistical uncertainties were significantly enlarged. The $Br(K_{e2\gamma}^{\mathrm{SD}})/Br(K_{e2(\gamma)})$ values determined by these PID conditions were consistent with those obtained using the optimized PID conditions within uncertainties, indicating the good reproducibility of the PID analysis in the simulation.

6.5 $Br(K_{e2\gamma}^{\mathrm{SD}})/Br(K_{e2(\gamma)})$ determination using GSC

Comparing with the CsI(Tl) calorimeter, the GSC timing resolution was much better and the background rate at the GSC position was much lower, and therefore, the K_{e2} and $K_{\mu2}$ events with accidental backgrounds observed in the CsI(Tl) analysis were drastically reduced. For the charged particle selection, we choose the wide PID cut conditions as,

- Flight length > 240 cm
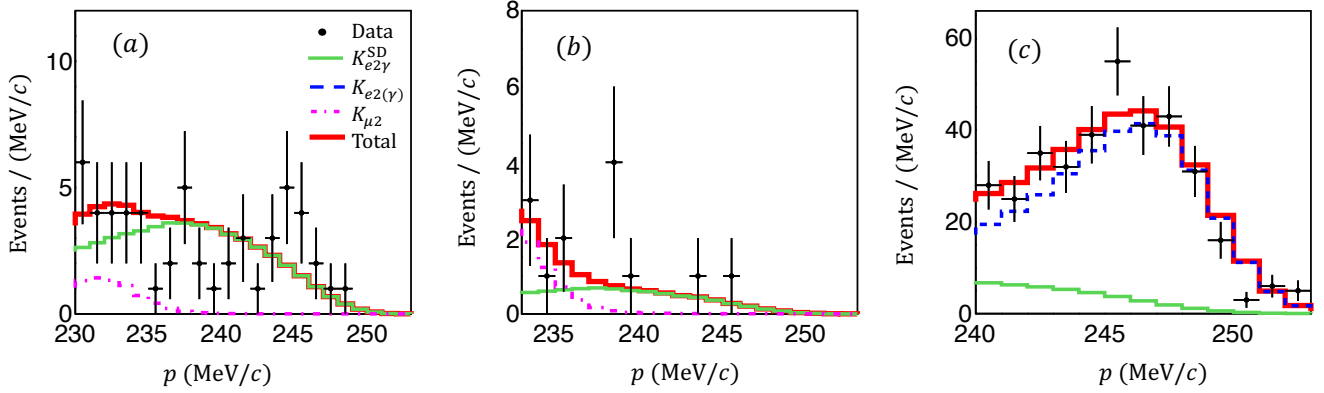
- K$^+$ stopping position $r < 3$ cm

Figure 60: Charged particle momentum spectra for the Crun data with requiring the (a) 1-cluster and (b) 2-cluster in the CsI(Tl) calorimeter and (c) without any CsI(Tl) constraint. The black dots are the experimental data. The solid (green), dashed (blue), and dashed-dotted (magenta) lines are the $K_{e2\gamma}^{\rm SD}$, $K_{e2(\gamma)}$, and $K_{\mu2}$ decays, respectively, determined by simulation calculations. The thick-red lines are the fitted result obtained by adding all decay contributions.

- Tracking $\chi^2/$n.d.f $< 50/4$

- gd_ehole flag $= 1$

- ktime > 1.5 ns

- PID condition

    - ACADC > 220
    - PGCADC > 120
    - TOFMASS < 5000

The $K_{e2\gamma}^{\rm SD}$ selection using GSC was quit simple, and we just imposed the GSC hit with 0 photon cluster in the CsI(Tl) calorimeter. The $K_{e2(\gamma)}$ events were removed and the $K_{e2\gamma}^{\rm SD}$ events were successfully observed, as shown in Fig. 61. The e^+ momentum spectra were obtained by selecting events with the spectrometer sector difference of the accepted e^+ and radiative photon (diff) for (a) 6, (b) 5, and (c) 4. Also, the e^+ momentum spectrum without any photon constraint is shown in Fig. 61 (d). Since the $K_{e2\gamma}^{\rm SD}$ events are observed only for diff=6, 5 and not for diff=4, the $K_{e2\gamma}^{\rm SD}$ events are concentrated in the back-to-back direction of the e^+ and photon momenta. The spectrum shape of events with diff=6 is so different from that with diff=5, indicating correct understanding of the SD dynamics, as shown in Fig. 6 and 7. It is to be noted that the same yield of the $K_{\mu2}$ backgrounds in the three momentum spectra are assumed in the fitting[7]. The $Br(K_{e2\gamma}^{\rm SD})/Br(K_{e2(\gamma)})$ value defined in Eq. 79 and the $K_{e2\gamma}^{\rm SD}$ yield in the diff=6 data were the fitting parameters in order to simultaneously reproduce the

---

[7]The $K_{\mu2}$ yield in diff=6, 0 should be half of other combinations.

87

three momentum spectra by fixing the R_Ω and R_ξ values obtained by the MC simulation. The fitting results are shown in the figures by the red line, and the decomposed $K_{e2\gamma}^{\mathrm{SD}}$, $K_{e2(\gamma)}$, and $K_{\mu2}$ decays are indicated by the dashed (green), dotted (blue), and dashed-dotted (magenta) lines, respectively. The accepted $K_{e2\gamma}^{\mathrm{SD}}$ and $K_{e2(\gamma)}$ yields and the associated R_Ω/R_ξ values are given in Table 18 entitled as physics run (Prun) along with the statistical uncertainties from the fits.
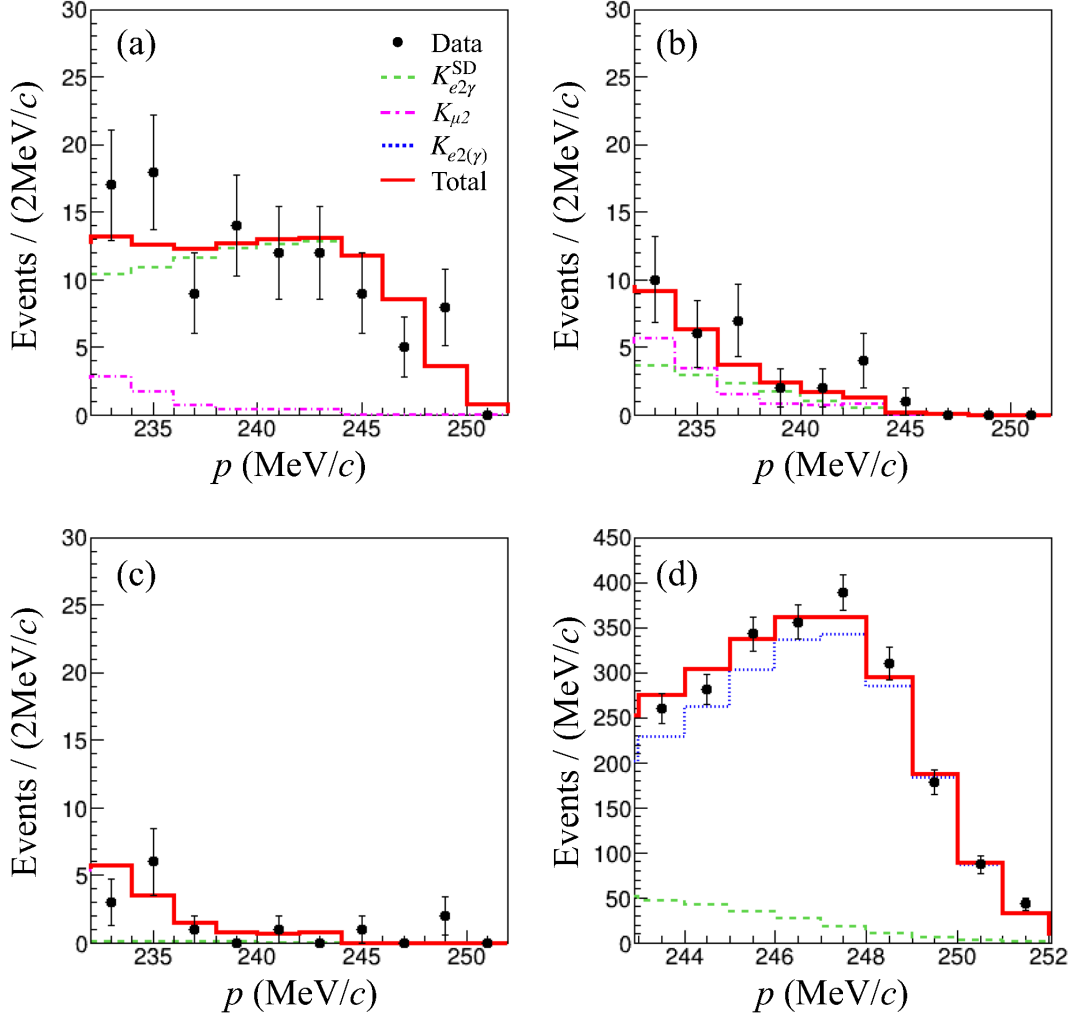
Figure 61: Charged particle momentum spectra for (a) diff=6, (b) diff=5, (c) diff=4 requirements and (d) charged particles without any photon constraint. The dots (black) are the experimental data. The dashed (green), dashed-dotted (magenta), dotted (blue) lines are the $K_{e2\gamma}^{\mathrm{SD}}$, $K_{\mu2}$ and $K_{e2(\gamma)}$ decays, respectively, determined by the simulation calculation. The solid (red) line is the fitted result obtained by adding all decay items.

Table 18: Results of the individual counts N, acceptance ratio with GSC efficiency correction R_Ω/R_ξ, and $Br(K_{e2\gamma}^{\text{SD}})/Br(K_{e2(\gamma)})$ values with statistical uncertainties obtained by simultaneously fitting the events with diff=6, diff=5, diff=4 and without GSC constraint for Prun. $N(K_{e2(\gamma)})$, $N(K_{e2\gamma}^{\text{SD}})$ in the fitting regions of $p > 232$ and 242 MeV/c for the events with GSC hit and without GSC constraint, respectively, are given.

	Run period	Prun
Without GSC constraint	$N(K_{e2(\gamma)})$	1935 ± 49
	$N(K_{e2\gamma}^{\text{SD}})$	194 ± 20
Gap difference 6	$N(K_{e2\gamma}^{\text{SD}})$	99 ± 10
	R_Ω/R_ξ	22.35
Gap difference 5	$N(K_{e2\gamma}^{\text{SD}})$	13 ± 1
	R_Ω/R_ξ	171.23
Gap difference 4	$N(K_{e2\gamma}^{\text{SD}})$	0 ± 1
	R_Ω/R_ξ	5344.39
Results	χ^2/dof	65.1/58
	$N(K_{e2\gamma}^{\text{SD}})$	113 ± 12
	$Br(K_{e2\gamma}^{\text{SD}})/Br(K_{e2(\gamma)})$	1.15 ± 0.12

7 Systematic uncertainties

In the present work, the $Br(K_{e2\gamma}^{\text{SD}})$ value relative to $Br(K_{e2(\gamma)})$ was obtained by calculating the ratio of the $K_{e2\gamma}^{\text{SD}}$ and $K_{e2(\gamma)}$ yields, as defined in Eq. 15 or in Eq. 79. The charged particle analysis was first performed, then the photon measurement was required for the further $K_{e2\gamma}^{\text{SD}}$ selection. Therefore, the dominant contributions to the systematic uncertainty are due to the ambiguity of the radiative photon measurement in the $K_{e2\gamma}^{\text{SD}}$ decay.

7.1 Systematic uncertainties in the CsI(Tl) analysis

The systematic uncertainties for the $Br(K_{e2\gamma}^{\text{SD}})/Br(K_{e2(\gamma)})$ determination are summarized in Table 20. The total size of the systematic uncertainty in the $Br(K_{e2\gamma}^{\text{SD}})/Br(K_{e2(\gamma)})$ determination was thus obtained by adding each item in quadrature to be 0.036. Here we would like to explain each component as follows.

7.1.1 Hole size of CsI(Tl) calorimeter

Imperfect reproducibility of the CsI(Tl) crystal size in the simulation can introduce the systematic uncertainty due to change of the photon acceptance. These effects were estimated by assuming three independent hole size reduction as (A) upstream (2 mm), (B) downstream (2 mm), and C. sideway (0.5 mm) in the simulation, which are the maximum conceivable possibility taking into account the CsI(Tl) mechanical construction procedure. The event loss probabilities were treated as the effects due to the hole size uncertainty as, $(5.9 \pm 0.3) \times 10^{-3}$, $(1.20 \pm 0.04) \times 10^{-2}$, and $(2.0 \pm 0.2) \times 10^{-3}$ for the (A), (B), and (C) conditions, respectively. Therefore, the total size of the CsI(Tl) hole size

effect was estimated to be 1.42×10^{-2}. The $Br(K_{e2\gamma})/Br(K_{e2(\gamma)})$ value is denoted as R_{Br}) and the uncertainty of R_{Br}), ΔR_{Br}, is given as,

$$\Delta R_{Br} = R_{Br} \times (1.42 \times 10^{-2}) \tag{80}$$
$$= 0.017 \tag{81}$$

Table 19: Effects from uncertainty of the CsI(Tl) hole size. They were estimated by reducing the hole size with the maximum conceivable values

Part	Reason	uncertainty	Relative error
A	Crystal size	dy=0.5 mm	$(5.9 \pm 0.3) \times 10^{-3}$
B	Muon hole wall	dz=2 mm	$(1.20 \pm 0.04) \times 10^{-2}$
C	Muon hole wall	dz=2 mm	$(2.0 \pm 0.2) \times 10^{-3}$
Total	quadratic sum		1.42×10^{-2}

7.1.2 CsI(Tl) misalignment

Since M^2_{miss} was calculated using photon vectors, the CsI(Tl) misalignment can introduce wrong M^2_{miss} calculation result. In the analysis, events were chosen using the M^2_{miss} cut, the CsI(Tl) misalignment can contribute to the systematic effect in the R_{Br} deduction.

The CsI(Tl) calorimeter was placed on the supporting rail and fixed to the toroidal magnet, the misalignment in x and y directions was negligible. The maximum conceivable shift in z direction was considered to be $\sigma_z \sim 1$ mm, and the R_{Br} value was re-calculated assuming this shift in the simulation. The parameter shift of

$$\Delta R_{Br} < 0.0006 \tag{82}$$

was adopted as the systematic uncertainty due to the CsI(Tl) misalignment, so it's uncertainty is negligible.

7.1.3 Imperfect reproducibility of photon angular distribution

The distribution in the simulation is little inconsistent with the experimental data for the photon's polar angle distribution as shown in Fig. 62. In particular, the simulation counts seems to be higher than the experimental data for upstream events(~ -0.5), and opposite trend for downstream events(> 0.5). The estimation of the systematic error due to this inconsistency will be discussed in this section.

The systematic uncertainty due to the above non-reproducible spectrum shape was estimated by dividing events by a cut of $\cos\theta_\gamma = 0.5$ and the R_{Br} shift was treated as the uncertainty due to this effect. The sample 1 and 2 are defined as a region -1 to 0.5 and 0.5 to 1, respectively. After that, these R_{Br} values of sample 1 and 2 are separately calculated to be (1.119 ± 0.071) using ~ 849 events and (1.114 ± 0.176) using ~ 202 events, respectively. The central value of R_{Br} is $(1.120 \pm 0.065) \times 10^{-5}$. The maximum conceivable shift is obtained to be $\Delta R_{Br} = 0.0006$.
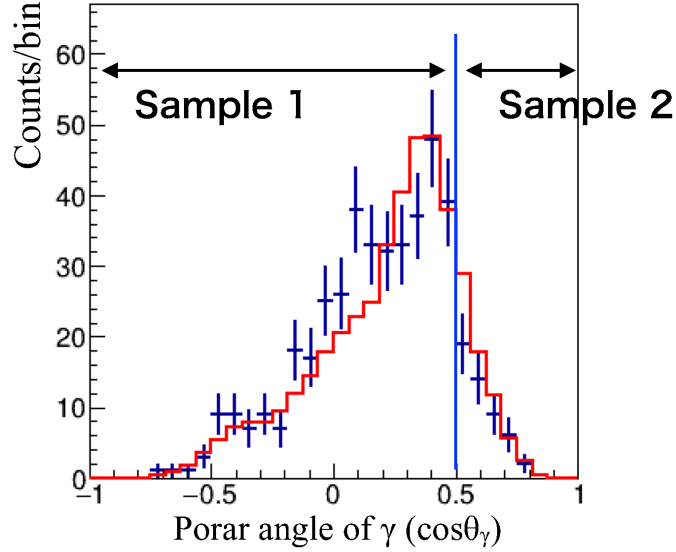
Figure 62: The distribution of photon direction z-coordinate using the events in Fig. 58 (a). The sample is divided with a boundary of $\cos\theta_\gamma = 0.5$ in order to calculate the effect of Br shift by the inconsistency. The sample 1 and 2 are defined as a region -1 to 0.5 and 0.5 to 1, respectively.

7.1.4 Accidental backgrounds in CsI(Tl)

The beam backgrounds strongly depended on the parameter setting of the K1.1BR beamline elements, and were being varied during the E36 data-taking period. These backgrounds were taken into account in the simulation by integrating over all of the physics runs. In order to check the effect of the background intensity fluctuation, the beam background data were separated into 4 subsets of the data. The R_{Br} analysis was 4 times repeated adopting these subset data as the accidental backgrounds in the simulation. Note the experimental data was the same among the above 4 trials. The R_{Br} value can be derived by averaging these values. Statistical uncertainty of these R_{Br} values was meaningless in this estimation, and it is enough to check parameter shifts.

The standard deviation of this distribution was obtained to be

$$\sigma^2 = \sum_{j=1}^{n=4} \frac{\Delta R_{Br_j}^2}{n-1} \tag{83}$$

Since the uncertainty of the average value was

$$\sigma_{\text{ave}} = \sqrt{\sum_{j=1}^{n=4} \frac{\Delta R_{Br_j}^2}{n(n-1)}} \tag{84}$$

which was adopted as the systematic uncertainty of the accidental background fluctuation.

This σ_{ave} is calculated to be

$$\sigma_{ave} = \Delta R_{Br} = 0.004. \tag{85}$$

91

7.1.5 Photon energy threshold of CsI(Tl)

As discussed in the CsI(Tl) calorimeter section, the hardware threshold was set in the readout system of the VF48 Flash ADC. The threshold level was not constant and dependent on the gain and DC level for each CsI(Tl) module. Therefore, we have to set a new common threshold in the analysis stage a little above the hardware threshold. However, the photon energy distribution is wide, and in the low energy region around 20 MeV the photon yield increase with increasing the energy. Therefore, if we raise the threshold, imperfect reproducibility of the energy distribution by the simulation enhances this systematic effect.

Here, we perform the R_{Br} determination as a function the cut point (E_{cp}). In the region of $E_{cp}=19-23$ MeV, the R_{Br} values were stabilized, although R_{Br} was affected by this cut in higher energy region. It can be considered that $E_{cp}=19-23$ MeV is low enough to reduce the systematics due to the MC imperfect reproducibility of the photon measurement. We interpreted the parameter fluctuation in the $E_{cp}=19-23$ MeV region is the systematic effect of the CsI(Tl) energy cut. The error is calculated to be

$$\Delta R_{Br} = 0.0071 \tag{86}$$

7.1.6 Photon energy calibration of CsI(Tl)

Relative gain coefficient of each CsI(Tl) module was calibrated using monochromatic μ^+s from the $K_{\mu2}$ decays. These gain coefficient was re-adjusted by introducing a new global coefficient ($G_{gl} = 0.93$) in order to reproduce the $M_{\gamma\gamma}$ distribution of the π^0 decay. The G_{gl} error size is better than 1%, and therefore effect to the R_{Br} determination was estimated by changing the G_{gl} value by 1% level and obtained to be

$$\Delta R_{Br} < 0.0008. \tag{87}$$

7.1.7 Photon timing window

Since the CsI(Tl) single rate was high due to direct hits of beam particles, effects from accidental backgrounds to the R_{Br} value have to be carefully discussed. These backgrounds were taken into account in the simulation by merging the actual background data using the $K_{\mu2}$ events. Therefore, the R_{Br} analysis result should not be changed by adopting wider window for the timing CsI(Tl) selection and accepting side band events of the true peak, if the treatment of the accidental backgrounds was correct.

Dependence of the R_{Br} values on the timing widow width was checked by using the gate window of $T_{\text{win}} = 100$ ns-150 ns. Here the gate width of 80 ns was too narrow and the R_{Br} value should decrease by rejecting proper photon events. These results were consistent with the statistical uncertainty. and the parameter difference between 100 ns and 150 ns was adopted as the systematic uncertainty of the beam background effects.

The error is calculated to be

$$\Delta R_{Br} = 0.009 \tag{88}$$

7.1.8 CsI(Tl) detection efficiency

CsI(Tl) efficiency was obtained using the $K_{\pi 2}$ events. The statistical uncertainty of this value was treated as a systematic effect of the photon measurement by the CsI(Tl) calorimeter.

$$\Delta R_{Br} = 0.012 \tag{89}$$

7.1.9 PID efficiency error

The momentum dependence of the PID efficiency of the AC, PGG, and TOF system in the region higher than the K_{e3} endpoint have been determined, as discussed in section 4.6. The efficiency distributions were fitted by a linear function using the K_{e3} and in-flight K_{e3} events. In order to fix to experimental,the simulation e^+ spectrum was re-weighted using the fitting results of the relative efficiency of AC, PGC, and TOF, as summarized in the Table 14, 13, and 15. In addition, we considered effects from the uncertainty of the slope parameters for the R_{Br} determination. Basically this factor is pointed to uncertainty of acceptance ratio between K_{e2} and $K_{e2\gamma}^{\mathrm{SD}}$ (R_Ω). When the branching ratio is combined, the center value would be biased to normal run due to smaller statistical error than one of systematic control run. Therefore, the systematic error of normal run is dominated and we have estimated error size for normal run.

AC efficiency In a case of AC, the efficiency curve depending on p is decided to

$$\varepsilon(p) = (-0.45 \pm 0.42) \times 10^{-3} \times p + (1.04 \pm 0.09) \tag{90}$$

for standard PID condition, cut point $ACADC = 100$. The error of R_{Br} when the slope is changed within the fitted error is estimated to be $+0.0059/-0.0064$, resulting 0.006 as systematic uncertainty.

PGC efficiency In a case of PGC, the efficiency curve depending on p is decided to

$$\varepsilon(p) = (0.02 \pm 0.48) \times 10^{-3} \times p + (0.84 \pm 0.10) \tag{91}$$

for standard PID condition, cut point $PGCADC = 140$.
 The error of R_{Br} when the slope is changed within the fitted error is estimated to be $+0.0056/-0.0073$, resulting 0.007 as systematic uncertainty.

TOF efficiency In a case of TOF, the efficiency curve depending on p is decided to

$$\varepsilon(p) = (-2.78 \pm 0.58) \times 10^{-3} \times p + (1.49 \pm 0.13) \tag{92}$$

for standard PID condition, cut point $TOFmass = 4000$ MeV$^2/c^4$.
 The error of R_{Br} when the slope is changed within the fitted error is estimated to be $+0.0134/-0.0186$, resulting 0.019 as systematic uncertainty.

7.1.10 $K_{\mu 2}$ background subtraction

In the analysis, we took into account the contribution of the $K_{\mu 2}$ backgrounds, which should be subtracted in the fitting. However, if we did not correctly understand the $K_{\mu 2}$ behavior and the decomposition was not successful in the fitting, this effect can contribution to the systematic uncertainty.

Here, we checked shifts of R_{Br} depending on the number of $K_{\mu 2}$ events as a function of the TOF mass cut point and AC ADC cut point. We could not find significant shifts or trend for R_{Br} depending on the $K_{\mu 2}$ yields. In addition, we estimated fluctuation of the R_{Br} value due to the number of $K_{\mu 2}$ events and 0.015 is obtained. We took account to systematic error less than 0.015.

7.1.11 $K_{e2\gamma}^{\mathrm{SD}}$ form factor

Since the (e^+, γ) angular correlation and photon energy distributions depend on the $K_{e2\gamma}^{\mathrm{SD}^+}$ form factor, the detector acceptance was affected by the λ parameter. The $Br(K_{e2\gamma}^{\mathrm{SD}^+})/Br(K_{e2(\gamma)})$ shift due to a parameter change of $\Delta\lambda = 0.1$ [34] was interpreted as systematic uncertainty. Although effects from a A/V_0 uncertainty were not serious, the detector acceptance was calculated by varying $\Delta(A/V_0) = 0.1$ and treated as a systematic uncertainty. This effect was estimated by changing the $K_{e2\gamma}^{\mathrm{SD}}$ distribution with a re-weight method. The acceptance change in the parameter region of $lambda = 0.3 \pm 0.1$ was obtained to be

$$\Delta R_{Br} = 0.011, \tag{93}$$

which was regarded as the systematic effect due to the form factor uncertainty.

7.1.12 K^+ stopping distribution

The kaon stopping distribution in MC simulation has been determined using the $K_{\mu 2}$ sample and input to the simulation, however imperfect reproducibility of the K^+ stopping distribution must introduce the systematic uncertainty. We check the R_{Br} value shifting the K^+ stopping distribution. The change of R_{Br},

$$\Delta R_{Br} = 0.003. \tag{94}$$

was treated as the systematic uncertainty of this effect.

7.1.13 Material thickness in the central parts

In the E36 simulation code, detector materials where charged particles passed were carefully input, but material thickness around the target was not accurate, as explained in section 5.2. In particular, the AC PMTs were not taken into account at all, which would affect the K_{e2}-EB tail and the photon loss in the analyses. Although opening angle of e^+ and e^- pair from photon conversion is small and this event must be accepted as a normal photon event, the effect has to be estimated.

According to the $\cos\theta_{e\gamma}$ distribution, it is sufficient to consider events in the region of $\cos\theta_{e\gamma} < -0.85$, which corresponds to CsI(Tl) crystal #1$\sim$#7. This effect was checked assuming additional

materials in the simulation and missing photon probability was calculated as a function of the assumed material thickness. As a result, this systematic effect is concluded to be negligibly small as,

$$\Delta R_{Br} < 0.0001 \tag{95}$$

7.1.14 Positron momentum resolution

In the simulation, the momentum resolution of charged particles due to the finite spatial resolution of the K^+ decay vertex was estimated to be $\sigma_p = 0.9\%$. Although the contribution to the systematic uncertainty from the charged particle measurement was considered to be very small, this effect was checked by changing the momentum resolution assumed in the simulation. As a result, this effect was estimated to be

$$\Delta R_{Br} = 0.002. \tag{96}$$

7.1.15 Magnetic field

The magnetic field in our spectrometer was controlled by the magnet current intensity. However, it is well-known a relation between the current and observed $K_{\mu2}$ momentum peak. It is should be noted the final result was obtained by using the corrected momentum for the target deposit energy.

Here, we researched the effect from the magnetic field uncertinty. The experimental momentum should be shifted by a factor, such as $p'_e = p_e * k$, when the magnetic field was not determined correctly. We show several spectra by varying the k parameter in the region of $k = 0.9910 \sim 1.011$, as shown in Fig. 63. The bottom plots are the subtraction spectra of $N_{\mathrm{exp}} - N_{\mathrm{MC}}$. The chi-square as a function of k is shown in Fig. 64, and thus the best tuning factor of $k = 1.0012 \pm 0.0001$ was obtained. The ΔR_{Br} was calculated from the error size of the k parameter. By the $k = 1.0012 \pm 0.0001$ parameter, the ΔR_{Br} was determined to be $+0.0016/-0.0012$,respectively. Therefore, the systematic error is less than $\Delta R_{Br} = 0.0016$ at most.

7.1.16 In-flight kaon decay

The E36 simulation started from K^+ decays at rest and we did not take into account in-flight (IF) K^+ decay in the simulation. Therefore, the simulation could not reproduce in-flight K^+ events and we should remove these in-flight decays by the event selection cuts. The most reliable quantity to reject these events is the timing of the beam Cherenkov counter to measure the K^+ incoming time to the experimental area (K-time). Events with the in-flight K^+ decays concentrate around the prompt timing of the K-time spectrum.

K-time distribution with 2γ and $p_e > 230$ MeV/c has 0-ns peak and time component of exponential tail, as shown in Fig. 28. The IF events distributes 0 ns peak, as a prompt signal, which is fitted by the Gaussian function with the $\sigma \sim 0.8$ ns. The stopped kaon events distributes as a tail component with kaon life time $\sim$12 ns, so it is fitted by the exponential function. The best time constant is focus to 15 ± 2 ns. In the analysis, K-time cut point was set to 1 ns, and it should be estimated the systematic error for R_{Br} shift by K-time change from 1 ns. Here, the number of IF events in ktime¿1 ns is calculated to be 6 from the result of Gaussian fitting. Thus, we considered the
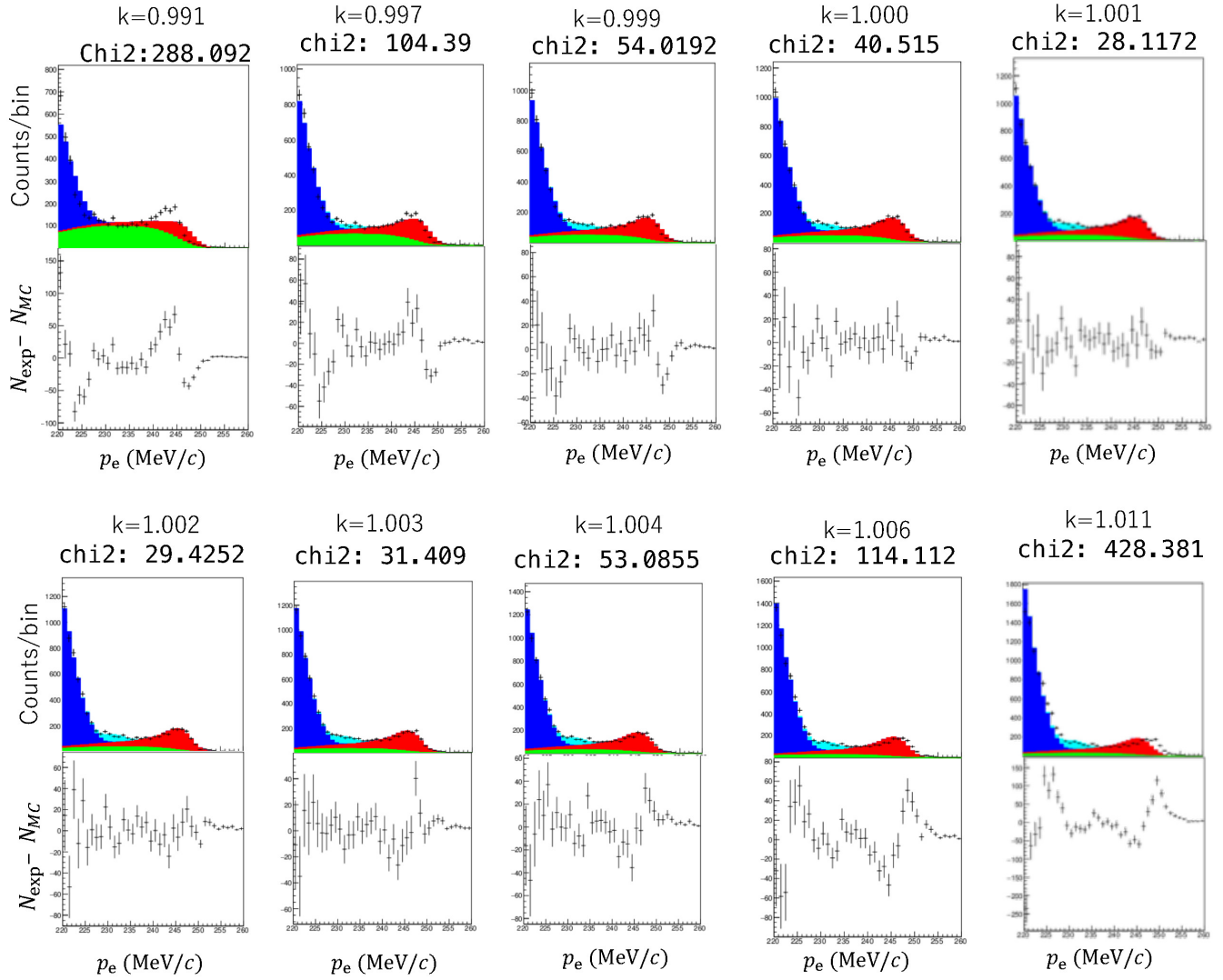
Figure 63: The momentum spectra affected by a factor k, strongly, as a case that the magnetic field is not determined correctly.
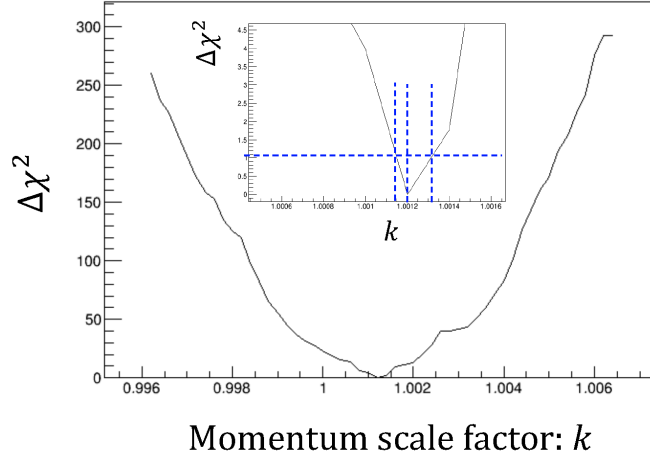
Figure 64: Relation between χ^2 and the fine tune factor k. The best factor $k = 1.0012$ as a minimum χ^2 is obtained and the error of 0.0001 is estimated.

systematic uncertainty is determined as a R_{Br} shift when the IF event changes to 1σ. The 2.3 events of IF are decrease and 2.0 events of IF are increase when the ktime is changed to 1.2 ns and 0.85 ns, respectively. As a result for the systematic error calculation, The R_{Br} shift is $\Delta R_{Br} = +0.00015 \times 10^{-5}$ and $\Delta R_{Br} = 0.00223 \times 10^{-5}$ for the Ktime is set to 1.2 ns and 0.85 ns, respectively. Therefore, the systematic error via in-flight kaon decay contamination is determined to be $\Delta R_{Br} = 0.00223$ at most.

7.2 Systematic uncertainties in the GSC analysis

The estimation method for systematic uncertainties in the GSC analysis is quite similar to that in the CsI(Tl) analysis. Here, their estimated results are summarized by separating each item and finally they are added in quadrature. The charged particle analysis was common for the K_{e2} and $K_{e2\gamma}^{\mathrm{SD}}$ events, while the photon detection was only required for the $K_{e2\gamma}^{\mathrm{SD}}$ selection. Therefore, the dominant contribution to the systematic uncertainty is due to the ambiguity of the radiative photon measurement. The systematic uncertainties for the $Br(K_{e2\gamma}^{\mathrm{SD}})/Br(K_{e2})$ determination are summarized in Table 21.

The R_ξ values were calculated by changing the $K_{\pi2}$ selection conditions, and the parameter shifts were treated as the systematic uncertainty of the R_ξ determination, which is the most dominant contribution in the GSC analysis. The imperfect reproduciblity of the GSC geometry in the simulation can introduce a systematic uncertainty through a change in the photon acceptance. This effect was estimated by considering the maximum conceivable detector misalignment of 2 mm.

Although the accidental backgrounds in the GSC were efficiently removed compared with the CsI(Tl) analysis and these contributions were considered to be very small, they were checked by changing the selection window of the timing gate. The effect from the $K_{\mu2}$ subtraction was estimated by intentionally changing the $K_{\mu2}$ fraction with various PID selection conditions. The $Br(K_{e2\gamma}^{\mathrm{SD}})/Br(K_{e2})$ changes were interpreted as the contribution from this effect. The (e^+, γ) angular correlation depends significantly on the λ parameter, which introduces a systematic uncertainty through a change in the

Table 20: Summary of the systematic uncertainties for the $Br(K_{e2\gamma}^{\mathrm{SD}})/Br(K_{e2})$ ratio determination in the CsI(Tl) analysis.

Source	Systematic uncertainty
Hole size of CsI(Tl) calorimeter	0.017
CsI(Tl) misalignment	< 0.001
Imperfect reproducibility of photon angular distribution	< 0.001
Accidental backgrounds in CsI(Tl)	0.004
Photon energy threshold of CsI(Tl)	0.007
Photon energy calibration of CsI(Tl)	< 0.001
Photon timing window	0.009
CsI(Tl) detection efficiency	0.012
AC detection efficiency	0.007
PGC detection efficiency	0.007
TOF detection efficiency	0.019
$K_{\mu2}$ background subtraction	0.015
$K_{e2\gamma}^{\mathrm{SD}}$ form factor	0.011
K^+ stopping distribution	0.003
Material thickness in the central parts	< 0.001
Positron momentum resolution	0.002
Magnetic field	0.002
In-flight kaon decay	0.002
Total	0.036

detector acceptances. The $Br(K^{\mathrm{SD}}_{e2\gamma})/Br(K_{e2})$ shift due to a parameter change of the theoretical uncertainty [34] $\Delta\lambda = 0.1$ was interpreted as the systematic uncertainty.

The total size of the systematic uncertainty in the $Br(K^{\mathrm{SD}}_{e2\gamma})/Br(K_{e2})$ determination was obtained by adding each item in quadrature to be 0.080. Since the statistical uncertainty in the GSC analysis is unfortunately much higher than that in the CsI(Tl) analysis, it is not necessary to seriously consider the systematic uncertainties in the GSC analysis.

Table 21: Summary of the systematic uncertainties for the $Br(K^{\mathrm{SD}}_{e2\gamma})/Br(K_{e2})$ ratio determination in the GSC analysis.

Source	Uncertainty
GSC misalignment	< 0.001
GSC timing window	0.025
GSC detection efficiency	0.060
AC detection efficiency	0.008
PGC detection efficiency	0.010
TOF detection efficiency	0.013
$K_{\mu2}$ background subtraction	0.042
$K^{\mathrm{SD}}_{e2\gamma}$ form factor	0.001
K^+ stopping distribution	0.009
Material thickness in the central parts	< 0.001
Positron momentum resolution	0.002
Magnetic field	0.002
In-flight kaon decay	0.002
Total	0.080

8 Results and discussion

In CsI(Tl) analysis, The $K_{e2\gamma}^{\mathrm{SD}}$ branching ratio relative to the $K_{e2(\gamma)}$ decay was determined using the Prun and Crun analysis results with a total of 574 ± 30 $K_{e2\gamma}^{\mathrm{SD}}$ events, and an error-weighted average of these values was adopted as the final result by adding the total size of the systematic uncertainties as [13]

$$Br(K_{e2\gamma}^{\mathrm{SD}})/Br(K_{e2(\gamma)}) = 1.12 \pm 0.07_{\mathrm{stat}} \pm 0.04_{\mathrm{syst}}. \tag{97}$$

The SD process is not subject to the helicity suppression mechanism of the week charged current, and $K_{e2\gamma}^{\mathrm{SD}}$ branching ratio is comparable to that of $K_{e2(\gamma)}$, which is specific characteristic in the e^+ channel. In general, the SD branching is much smaller than the IB branching ratio (for example, SD process in $K^+ \to \mu^+\nu\gamma$ and $K^+ \to \pi^+\pi^0\gamma$), and it is very difficult to select the SD events with low IB contamination. As well as $K_{e2\gamma}^{\mathrm{SD}}$, the structure dependent $\pi^+ \to e^+\nu\gamma$ was clearly observed due to the same reason as the K^+ decay.

In GSC analysis, the $Br(K_{e2\gamma}^{\mathrm{SD}})/Br(K_{e2(\gamma)})$ value was also determined using the Prun data[8] with a total of 113 ± 12 $K_{e2\gamma}^{\mathrm{SD}}$ events as

$$Br(K_{e2\gamma}^{\mathrm{SD}})/Br(K_{e2(\gamma)}) = 1.15 \pm 0.12_{\mathrm{stat}} \pm 0.08_{\mathrm{syst}}, \tag{98}$$

which is consistent with the result obtained using the CsI(Tl) calorimeter within the experimental uncertainty, although the kinematical approach of the GSC analysis is essentially different from that of the CsI(Tl) analysis. It should be emphasized that information of the photon and hit position were used in the CsI(Tl) analysis by imposing the $K_{e2\gamma}^{\mathrm{SD}}$ kinematics in the event selection. On the other hand, although the GSC counters could not provide these information, the e^+ momentum spectra of the $K_{e2\gamma}^{\mathrm{SD}}$ decay were successfully obtained by requiring only the GSC hits. This feature implies that invisible and/or non-evaluated systematic uncertainties are expected to be smaller than the current ones. Moreover, the present experimental uncertainties are dominated by the statistical ones and it can be said there is still a room to establish a new record of the $K_{e2\gamma}^{\mathrm{SD}}$ uncertainty by performing the further-improved-E36 experiment in the extended hadron halls at J-PARC.

The $Br(K_{e2\gamma}^{\mathrm{SD}})$ value relative to the $K_{\mu2}$ decay can be expressed as

$$\frac{Br(K_{e2\gamma}^{\mathrm{SD}})}{Br(K_{\mu2})} = \frac{Br(K_{e2\gamma}^{\mathrm{SD}})}{Br(K_{e2(\gamma)})} \times \frac{Br(K_{e2(\gamma)})}{Br(K_{\mu2})} = \frac{Br(K_{e2\gamma}^{\mathrm{SD}})}{Br(K_{e2(\gamma)})} \times R_K^{\mathrm{SM}} \tag{99}$$

using the R_K^{SM} prediction. Therefore, the $Br(K_{e2\gamma}^{\mathrm{SD}})/Br(K_{\mu2})$ value is derived to be $(2.77 \pm 0.17_{\mathrm{stat}} \pm 0.10_{\mathrm{syst}}) \times 10^{-5}$. Then, using $\lambda = 0.36$, which is the reported value by the KLOE group, Dalitz distribution of the $K_{e2\gamma}^{\mathrm{SD}}$ decay was numerical calculated. Events assuming the $K_{e2\gamma}^{\mathrm{SD}}$ matrix element were generated for the entire phase space, as shown in Fig. 65. The event fraction in the region of $p_e > 200\mathrm{MeV}/c$, $E_\gamma > 10$ MeV was obtained to be 0.6672. Thus, the partial fraction of the $K_{e2\gamma}^{\mathrm{SD}}$ branching ratio in the phase space region ($p > 200$ MeV/c, $E_\gamma > 10$ MeV) is obtained by correcting

---

[8]The $K_{e2\gamma}^{\mathrm{SD}}$ yield in Crun is very low, and we decided not to use Crun for the GSC analysis.

for the phase space reduction as

$$R_\gamma = \frac{Br(K_{e2\gamma}^{\mathrm{SD}},\ p > 200 \text{ MeV}/c,\ E_\gamma > 10 \text{ MeV})}{Br(K_{\mu2})} \tag{100}$$

$$R_\gamma^{\mathrm{E36}} = (1.85 \pm 0.11_{\mathrm{stat}} \pm 0.07_{\mathrm{syst}}) \times 10^{-5}, \tag{101}$$

from the CsI(Tl) analysis, where systematic effect of this phase space reduction due to the form factor uncertainty is estimated to be 0.007×10^{-5} and already included. This result is almost 25% ($\sim 2.5\sigma$) higher than the result, as shown in Fig. 66,

$$R_\gamma^{\mathrm{KLOE}} = (1.483 \pm 0.066_{\mathrm{stat}} \pm 0.013_{\mathrm{syst}}) \times 10^{-5} \tag{102}$$

reported in the previous experimental study [38], which supported the theoretical model model of ChPT-$\mathcal{O}(p^4)$ [35],

$$R_\gamma^{\mathrm{ChPT}} = 1.477 \times 10^{-5}, \tag{103}$$

and ChPT-$\mathcal{O}(p^6)$ [36]. On the other hand, the present result is in agreement with the recent lattice calculation [61], as shown in Fig. 66,

$$R_\gamma^{\mathrm{lattice}} = (1.74 \pm 0.21) \times 10^{-5}. \tag{104}$$

The Dalitz density can be described with the amplitude part, $V + A$, with small correction (λ) by the momentum transfer and kinematical dependence, $f_{\mathrm{SD+}}(x, y)$, as given in Eq. 11. The above theoretical model precisely reproduces the spectra shape of the observed $K_{e2\gamma}^{\mathrm{SD}}$ events indicating the correct understanding of $K_{e2\gamma}^{\mathrm{SD}}$ process by the $f_{\mathrm{SD+}}(x, y)$ term. However, the observed branching ratio is 25% higher than the ChPT prediction, and therefore, the $V + A$ value adopted in the model is 12% lower than this experimental result. Since the theoretical uncertainties are not quoted in the ChPT calculation [35, 36], non-evaluated diagrams or further higher-order calculations have to be taken into account. On the other hand, the lattice calculation predicted the correct $V + A$ amplitude, which is superior to ChPT for the $K_{e2\gamma}^{\mathrm{SD}}$ form factor calculation. It should be emphasized that the shape of the Dalitz distribution (i.e. $f_{\mathrm{SD+}}$) was assumed in the acceptance calculation, the derived $K_{e2\gamma}^{\mathrm{SD}}$ result does not be affected by the $V + A$ value and its uncertainty at all. For the R_K analysis, one of the most serious problem is the subtraction of the $K_{e2\gamma}^{\mathrm{SD}}$ events from the observed e^+ sample. In the e^+ sample, contribution from the normal $K_{e2(\gamma)}$ decay and the $K_{e2\gamma}^{\mathrm{SD}}$ process cannot be,in principle, distinguished, and the $K_{e2\gamma}^{\mathrm{SD}}$ contribution has to be subtracted which has a large hadronic uncertainty is regarded as a background for R_K, as discussed in section 3.1. On the other hand, in the present work, the separate spectra were obtained for events with 1 and 2 photons detected in the CsI(Tl) calorimeter and for events without conditions on the number of photons; these were fit simultaneously with the ratio $Br(K_{e2\gamma}^{\mathrm{SD}})/Br(K_{e2(\gamma)})$ and the yields of $K_{e2\gamma}^{\mathrm{SD}}$ and $K_{\mu2}$ decays as free parameters. The successful fitting made the reliable $K_{e2\gamma}^{\mathrm{SD}}$ subtraction from the e^+ sample, as shown in Fig. 67(a). Note the analysis procedure for the branching ratio determination of $K_{e2\gamma}^{\mathrm{SD}}$ by requiring the photon measurement is equivalent to the $K_{e2\gamma}^{\mathrm{SD}}$ subtraction in the R_K analysis, which is already realized in the present work. The $K_{\mu2}$ events of the experimental data (black) and the simulation (red) are also shown in Fig. 67(b). The R_K value can be derived using the above $K_{e2(\gamma)}$ and $K_{\mu2}$ yields and the
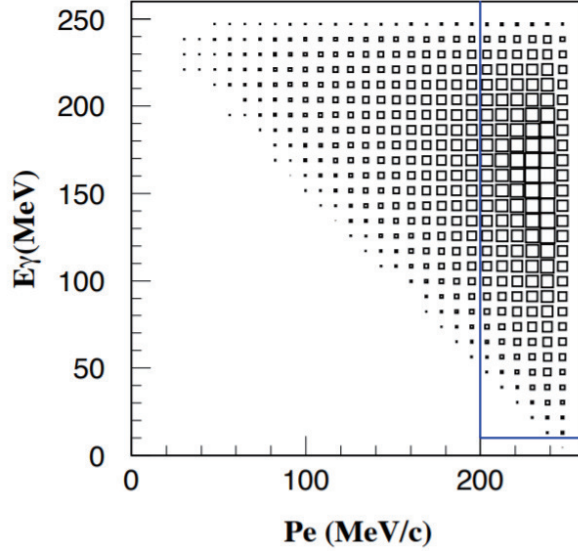
Figure 65: Dalitz plot distribution of the $K_{e2\gamma}^{\mathrm{SD}}$ decay. The event fraction in the region of $p_e >$ 200MeV/c, $E_\gamma > 10$ MeV was obtained to be 0.6672. In order to compare the present results with the KLOE's, the effect of this phase space reduction was calculated.
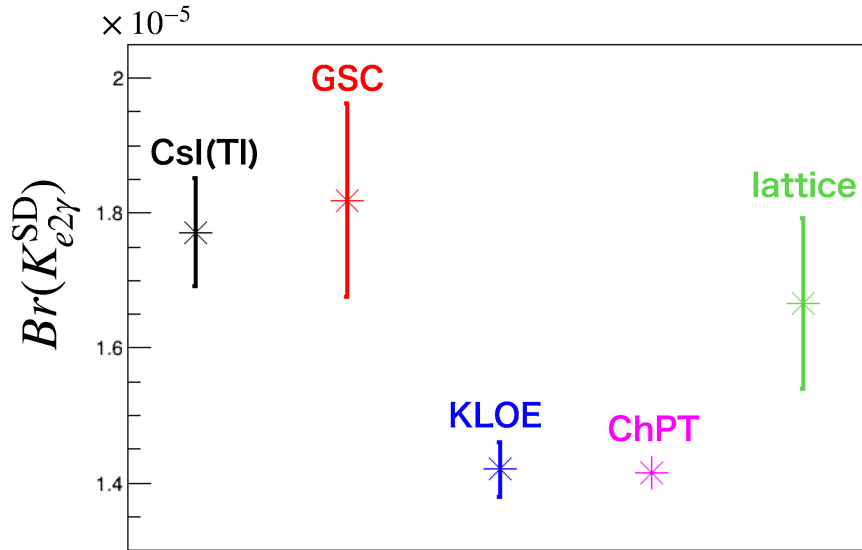

Figure 66: The $K_{e2\gamma}^{\mathrm{SD}}$ branching ratio obtained in the E36 experiment using CsI(Tl) (black) and GSC (red). The predicted R_K value was used for the E36 analysis. The KLOE result is shown in the blue dot, which is almost 25% ($\sim$2.5σ) lower than the E36 result. Theoretical calculations using ChPT (magenta) and lattice (green) are also shown.
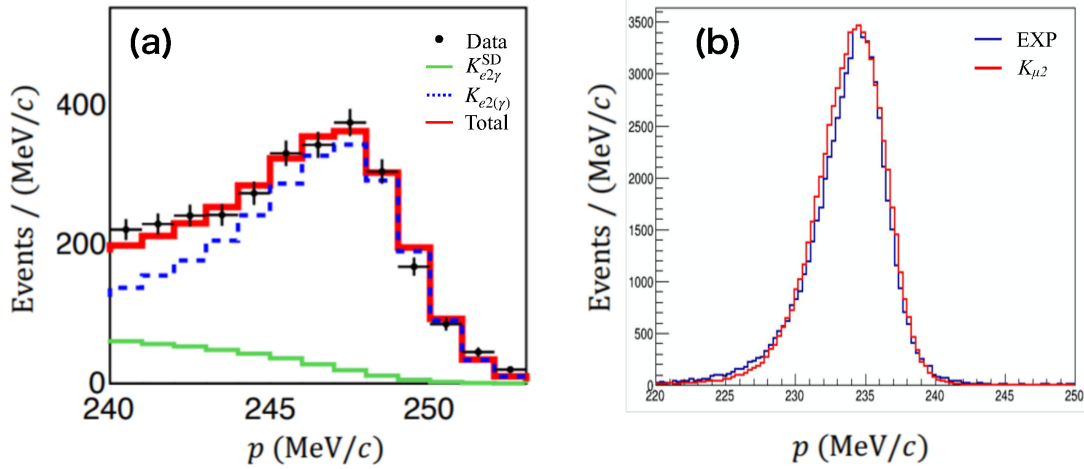
Figure 67: The momentum spectra for the (a) $K_{e2(\gamma)}$ and (b) $K_{\mu2}$ decays. In (a), the black dots are experimental data, and the blue/dotted and green/solid lines are the $K_{e2(\gamma}$ and $K_{e2\gamma}^{\mathrm{SD}}$ events, respectively, determined by the simulation calculation. The thick-red line is the fitted result obtained by adding all the two contributions. The black and red lines in (b) are the experimental and simulated $K_{\mu2}$ events, respectively. The R_K value can be derived using the $K_{e2(\gamma)}$ and $K_{\mu2}$ yields and the detector acceptances obtained from the simulated $K_{e2(\gamma)}$ and $K_{\mu2}$ yields.

detector acceptances obtained from the simulated $K_{e2(\gamma)}$ and $K_{\mu2}$ yields. It can be concluded that the present work promoted one of the essential analysis in the R_K determination.

In the NA62 experiment, which produced the result with the smallest R_K uncertainty, the $K_{e2\gamma}^{\mathrm{SD}}$ decay was the main background source in the $K_{e2(\gamma)}$ sample, which is the same situation as the E36 and KLOE experiments. It should be noted that the branching ratio of the $K_{e2\gamma}^{\mathrm{SD}}$ reported by the KLOE group was used in the NA62 analysis, and this SD contribution was subtracted from the observed $K_{e2(\gamma)}$. The $K_{e2\gamma}^{\mathrm{SD}}$ fraction in NA62 are described to be 1% or 4% depending on the data samples. This indicates the $K_{e2\gamma}^{\mathrm{SD}}$ fraction would increase by 25% and affect the R_K result in the NA62 analysis. Since the experimental uncertainty is reported to be 0.5%, this change would not be negligible for the R_K determination.

Finally, it is worthwhile to summarize the key points to obtain the successful result in the present work as,

- (1)consideration of accidental CsI(Tl) backgrounds in the Mote Carlo simulation,

- (2)accurate measurement for the kinematical reconstruction,

- (3)use of $K_{\pi2}$ events for the calibration purpose in the CsI(Tl) analysis.

First, if there had been no accidental backgrounds, the $K_{e2\gamma}^{\mathrm{SD}}$ event would have appeared as 1-hit or 0-hit (photon missed) events. However, 2-hit ($K_{e2\gamma}^{\mathrm{SD}}$+ BG) events were observed. We analyzed 0 and 1 hit events as well as these 2-hit events by introducing the accidental backgrounds into the MC simulation, which was performed as a correct treatment of the accidental backgrounds in CsI(Tl). Secondly, the E36 detector has high coverage in order to detect Kaon decays at rest. This feature

allowed us to measure the $K^{\mathrm{SD}}_{e2\gamma}$ kinematics precisely, as is seen in Fig. 59, 57, and 59. It can also let us extract pure $K^{\mathrm{SD}}_{e2\gamma}$ samples with an effective rejection of the $K_{\mu2}$ decay with background events. Thirdly, we used $K_{\pi2}$ samples for the analysis in various situation, for instance, measuring efficiency of GSC and CsI(Tl), checking reproducibility of MC simulation, and so on. It produced the correctness check for the R_ω calculation and the reliable analysis.

9 Acknowledgement

I would like to express my sincere gratitude to Prof. S. Yoshida for taking over responsibility for this dissertation and my Ph.D. study and research. He kindly arranged for me to be able to continue my research at Chiba University and encouraged me to derive the final result of the $K_{e2\gamma}^{\text{SD}}$ branching ratio. I would also like to thank Prof. H. Kawai for his support and guidance over the years. He has given me a lot of important opportunities, for instance presenting at international conferences, visiting various places and so on.

I am also grateful to Dr. S. Shimizu who is a spokesperson of the J-PARC E36 experiment in Japan, Dr. K. Horie, and Dr. J. Imazato for the continuous support of my Ph.D study and research, for their patience, motivation, enthusiasm, and immense knowledge. Their guidance helped me in all the time of research and writing of this thesis. I could not have imagined having better advisors and mentors for my Ph.D study. I am grateful to Dr. H. Ito for teaching me a lot of basic techniques. My sincere thanks also goes to Dr. M. Tabata for his generous support and various advises.

I also would like to thank Dr. M. Kohl and Dr. M. D. Hasinoff, who are the leading members of the J-PARC E36 collaboration abroad, for many important comments and suggestions in the meetings. I would like to express my sincere gratitude to the other E36 members : S. Bianchin, T. Cao, C. Djalali, D. H. Dongwi, T. Gautam, D. Gill, Y. Igarashi, N. Kalantarians, S. Kimura, S. Kodama, H. Lu, O. Mineev, P. Monaghan, S. Strauch, R. Tanuma, A. Toyoda, H. Yamazaki, N. Yershov. I am grateful to the J-PARC Support, the cryogenic group, the beam channel group, the KEK and J-PARC User's Office.

I thank my fellow labmates: S. Han, K. Okuhata, T. Yuzawa, H. Matsunaga, M. Sano, S. Murata, T. Mizuno, K. Fujiwara, Y. Emoto, H. Kobayashi, N. Kaneko, H. Ijiri and H. Isobe for the sleepless nights we were working together before deadlines and for all the fun we have had in the laboratory.

I would like to thank the other thesis committee members for my dissertation: Prof. A. Ariga, Prof. A. Ishihara, and Prof. H. Hotta, for their encouragement, insightful comments, and hard questions. I believe that my dissertation is certainly improved following the committee's comments and suggestions. Also, I am grateful to Prof. Matsuta, Prof. Fukuda, Prof. Mihara for their supports in Osaka University, and my dissertation work was actually developed in cooperation with Osaka researchers. The Osaka life to improved the $K_{e2\gamma}^{\text{SD}}$ analysis is really fun for me and never forget it.

I would also like to thank the members of the "Fureai-no-wa" which allowed me to experience a variety of volunteer activities. Also, I am grateful to the faculty members and the stuff including S. Shimonagata, M. Watanabe, S. Nagasawa, S. Yamauchi T. Tokuhisa, H. Sugeno, K. Tanaka, H. Goto, who supported our volunteer activities. In particular, I am indebted to Ms. Goto for her support throughout my student days.

I would like to thank Dr. Handa, the principal of "Seizan-Juku", for teaching me how to overcome hardships, what I should value in life and many other important things. I am also indebted to the seniors of "Seizan-Juku", Ms. Shiode, Mr. Funatsu, Mr. and Mrs. Asakawa. I would like to extend my gratitude to cheerful fellos of it. I cannot forget to thank Yoshida Scholarship Foundation, Japan Society for the Promotion of Science, and Japan Student Services Organization for supporting me financially.

Last but not the least, I would like to express most sincere and heartfelt gratitude to my entire family: Hiroko, Nanako, Hisato, Satsuki, Nobuyuki, Mami, Taizo, Megumi, Yusuke, Ryoma, Yurika,

Kayoko and Ritsuo, who have raised me, supported me, encourage me and believed in me.

References

[1] R. Dalitz, Phys. Rev. 94, 1046 (1954).

[2] E. Fabri, Nuvo Cimento 11, 479 (1954).

[3] J. Orear, G. Harris, and S. Taylor, Phys. Rev. 102, 1676 (1956).

[4] C. S. Wu et al., Phys. Rev 105, 1413 (1957).

[5] H. H. Christenson et al., Phys. Rev. Lett. 13, 138 (1964).

[6] S. Glashow, J. Iliopoulos, and L. Maiani, Phys. Rev. D2, 1285 (1970).

[7] M. Kobayahshi and T. Maskawa, Prog. Theor. Phys. Japan, 49, 652 (1973).

[8] P. A. Ayla et al. (Particle Data Group), Prog. Theor. Exp. 2020, 083C01 (2020).

[9] CERN-EP-2021-050.- Geneva.

[10] J. K. Ahn et al., Phys. Rev. Lett. 122, 021802 (2019); J. K. Ahn et al., Phys. Rev. Lett. 126, 121801 (2021).

[11] M. Abe et al., Phys. Rev. D 73 (2006) 072005.

[12] J. Gasser and H. Leutwyler, Nucl. Phys. B250, 517 (1985).

[13] H. Ito et al., Phys. Lett. B 826, (2022) 136913.

[14] W. J. Marciano and A. Sirlin, Phys. Rev. Lett. 71 (1993) 3629.

[15] F. Finkemeier, Phys. Lett. B 387 (1996) 391.

[16] A. Masiero, P. Paradisi, and R. Petronzio, Phys. Rev. D74 (2005) 011701(R).

[17] A. Masiero, P. Paradisi, and R. Petronzio, J. High Energy Phys. 0811 (2008) 042.

[18] K.S. Babu and C. Kolda, Phys. Rev. Lett. 89,(2002) 241802 .

[19] M. Sher, Phys. Rev. D66, (2002) 057301; A. Brignole and A. Rossi, Nucl. Phys. B701, (2004) 3.

[20] R. Kitano, M. Koike, S. Komine, and Y. Okada, Phys. Lett. B575, (2003) 300.

[21] A. Dedes, J.R. Ellis, and M. Raidal, Phys. Lett. B549, (2002) 159.

[22] A. Brignole and A. Rossi, Phys. Lett. B566, (2003) 217;E. Arganda, A.M. Curiel, M.J. Herrero, and D. Temes,Phys. Rev. D71, (2005) 035011.

[23] P. Paradisi, J. High Energy Phys. 02 (2006) 050; arXiv:[hep-ph/0601100] (2006).

[24] C. Lazzeroni et al., Phys. Lett. B719, (2013) 326.

[25] M. Moulson et al., in proceedings of KAON09, PoS (KAON09) 035 (2009).

[26] P. A. Zyla et al. (Particle Data Group), Prog. Theor. Exp. Phys. 2020, 083C01 (2020).

[27] F. Ambrosino et al., Eur. Phys. J. C64 (2009) 627-636; arXiv:[hep-ex/0907.3594] (2009).; Eur. Phys. J. C 65 (2010) 703.

[28] V. Cirigliano and I. Rosell, Phys. Lett. 99 (2007) 231801.

[29] G. Czapek et al., Phys. Rev. Lett. **70** (1993) 17.

[30] D.I. Britton et al., Phys. Rev. Lett. **68** (1992) 3000.

[31] D. Pocanic et al., arXiv:[hep-ex/0907.4358] (2009).

[32] D.A. Bryman, in proceedings of KAON07, PoS(KAON) 052 (2007).

[33] J. Bijnens, G. Ecker, and J Gasser, Nucl. Phys. B396 (1993) 81; J. Bijnens, G. Colangelo, G. Ecker, and J Gasser, published in 2nd DAPHNE Physics Handbook, (1995) 315.

[34] V. Cirigliano et al., Review of Modern Physics 84 (2012) 399.

[35] C. Q. Geng, I-Lin Ho, and T. H. Wu, Nucl. Phys. B 684 (2004) 281.

[36] Chuan-Hung Chen et al., Phys. Rev. D 77 (2008) 014004.

[37] C. Gatti, Eur. Phys. J. C 45 (2006) 417.

[38] F. Ambrosino et al., Eur. Phys. J. C 64 (2009) 627; Eur. Phys. J. C 65 (2010) 703.

[39] S. Shimizu, et al., Proposal for J-PARC 50 GeV Proton Synchrotron, P36 June, 2010; http://j-parc.jp/researcher/Hadron/en/Proposal_e.html

[40] S. Strauch et al., Proc. Sci., PoS(KAON13)014, 2013.

[41] J.A. Macdonald et al., Nucl. Inst. and Meth. Phys. Res. Sect. A506 (2003) 60.

[42] S. Shimizu et al., Phys. Lett. B 495 (2000) 33; Y. H. Shin et al., Eur. Phys. J. C 12 (2000) 627; K. Horie et al., Phys. Lett. B 513 (2001) 311; M. A. Aliev et al., Phys. Lett. B 554 (2003) 7; S. Shimizu et al., Phys. Rev. D 70 (2004) 037101; S. Shimizu et al., Phys. Lett. B 633 (2006) 190.

[43] J. Doornbos, "An 800 MeV/c separated kaon beam at J-PARC", May 2007, https://trek.kek.jp/e06/PAC/K1.1BR_add.pdf

[44] TREK homepage, http://trek.kek.jp/.

[45] V. Fitch and R. Motley, Phys. Rev, 101 (1956) 496.

[46] A. Kawachi et al., Nucl. Inst. and Meth. A416 (1998) 253.

[47] J. Simkin and C.W. Trowbridge et al., Rutherford report RL-79-097, Dec 1979.

[48] M. Tabata et al., Nucl. Instr. Meth. A 795 (2015) 206.

[49] Belle homepage, http://belle.kek.jp/.

[50] Summary of TOPAZ experiment; https://www2.kek.jp/proffice/archives/hyouka/TRISTANreport/

[51] Catalog of photomultiplier tubes; https://www.hamamatsu.com/jp/en/product/optical-sensors/pmt/catalog/index.html

[52] Y. Miyazaki et al., Nucl. Inst. and Meth. A779 (2015) 13.

[53] D.V. Dementyev et al., Nucl. Inst. and Meth. A440 (2000) 151.;D.V. Dementyev et al., Nucl. Inst. and Meth. A379 (1996) 499.

[54] S. Kimura, "Search for Dark Photon using the CsI(Tl) calorimeter in the J-PARC E36 experiment.", Master's Thesis, Chiba University, 2019.

[55] https://www.triumf.info/wiki/DAQwiki/index.php/VF48; Y. Igarashi and M. Saito, in: IEEE 2012 Nuclear Science Symposium and Medical Imaging Conference Record (Nss/MIC).

[56] M. Tabata et al., PoS(TIPP2014)328; arXiv:1411.6707[physics.ins-det] (2014).

[57] O. Mineev et al., Nucl. Inst. and Meth. A847 (2017) 136.

[58] S. Kodama, "Performace evaluation of Spiral Fiber Tracker (SFT) for the J-PARC E36 experiment", Master's Thesis, Chiba University, 2015.

[59] S. Shimizu et al., E36 technical note, http://www-online.kek.jp/ e06/pukiwiki/?SFT

[60] H. Ito et al., Nucl. Inst. and Meth. A901 (2018) 1.

[61] R. Frezzotti et al., Phys. Rev. D 103, (2021) 053005.